Microwave spectroscopy for probing electronuclear modes in quantum magnets

Thesis by
Matthew Libersky

In Partial Fulfillment of the Requirements for the
Degree of
Doctor of Philosophy in Applied Physics

CALIFORNIA INSTITUTE OF TECHNOLOGY
Pasadena, California

2025
Defended August 13, 2024

Matthew Libersky
ORCID: 0000-0003-4140-360X

Acknowledgements

Thanks to Dan Silevitch for help throughout, along with Stephen Armstrong and Chris Simon. Ryan McKenzie and Philip Stamp have helped with developing the theory sections, and Yikai Yang, Henrik Ronnow have provided helpful discussions. For Chapter 7, thanks to Sandra Glotzer and Matthew Chalk for film growth and microfabrication. Additional thanks to my advisors, Thomas Rosenbaum and Joseph Falson. Additionally to my family–with Charlotte, Belle, and Halo.

Abstract

Crystals with rare earth ions present an opportunity to explore a range of model magnetic systems, allowing for an experimental realization of several important physical concepts. For example, the compound $LiHoF_4$ is a transparent, insulating crystal which implements the transverse field Ising model (TFIM) with the Ho^{3+} spins. The TFIM is a well-known model which is one of the simplest systems to display quantum behavior, such as quantum phase transitions (QPTs). This makes $LiHoF_4$ very useful for investigating these and other quantum effects. $LiHoF_4$ also has strong hyperfine coupling to the nuclear spins, which means the excitations must be considered as composite of electronic and nuclear states (i.e., 'electronuclear'). This introduces a nuclear spin bath which modifies behavior near the QPT. In this work, we investigate the behavior of this QPT by probing the electronuclear states in $LiHoF_4$ at microwave frequencies. To accomplish this, we develop the use of loop-gap resonators which enable sensitive microwave measurements in $LiHoF_4$. We also extend the techniques to related systems, such as the 2-dimensional XY antiferromagnet $LiErF_4$. We then investigate ways to observe new phenomena in the $LiHoF_4$ system, namely improving superconducting resonators as one possible way to observe the dynamics of quantum quenching through the QPT.

Published Contents and Contributions

M. M. Libersky, D. M. Silevitch, and A. Kouki. "Design of a Loop-Gap Resonator with Bimodal Uniform Fields Using Finite Element Analysis." In: *2019 22nd International Conference on the Computation of Electromagnetic Fields (COMPUMAG)*. July 2019, pp. 1–4. DOI: 10.1109/COMPUMAG45669.2019.9032729

- I did most of the writing and calculations for this paper, with contributions from the other authors.

M. Libersky et al. "Direct Observation of Collective Electronuclear Modes about a Quantum Critical Point." In: *Physical Review Letters* 127.20 (Nov. 2021), p. 207202. DOI: 10.1103/PhysRevLett.127.207202

- This paper is primarily my work, with contributions from the respective coauthors.

R. D. McKenzie et al. "Theory of Magnon Polaritons in Quantum Ising Materials." In: *Physical Review A* 106.4 (Oct. 2022), p. 043716. ISSN: 2469-9926, 2469-9934. DOI: 10.1103/PhysRevA.106.043716

- This paper was written by collaborators developing theories based primarily on my experiments.

R. McKenzie. *Magnetostatic Modes and Criticality in Uniaxial Magnetic Materials*. Aug. 2023. arXiv: 2308.14169 [cond-mat]

- This paper was written by a collaborator, developing a theory based on some of my data.

P. Stamp et al. "Gallery of Soft Modes: Theory and Experiment at a Ferromagnetic Quantum Phase Transition." In: *Submitted to Physical Review B* (2024)

- This paper is mainly based on my experiments.

CONTENTS

LIST OF FIGURES

LIST OF TABLES

Chapter 1

Experimental System and Theory

The lanthanide series is made up of several metallic elements with very similar chemical properties. These are usually shown as a separate row shown below the periodic table (above the radioactive actinide series), fitting in between groups II and III. The neighboring elements yttrium and lutetium are generally considered lanthanides/rare earths, as they share most chemical properties. While yttrium has a much lighter atomic weight compared to the standard rare earth elements, it has very similar chemical properties. This is evidenced by the fact that it occurs alongside most of the other rare earth elements in natural ores, which themselves are notoriously difficult to separate. Going across the lanthanide row, each sequential element gets an additional 4f electron. Importantly, these are not the valence electrons, but rather an inner shell. This is why these elements are chemically very similar. As additional electrons are added to the 4f shell, these inner electrons poorly screen/block the positive nucleus. This leads to the valence electrons having a strong attraction to the nucleus and thus a smaller radius. This is called the lanthanide contraction and causes the heavier atoms to unexpectedly have a smaller radius than the rare earth elements with lower atomic numbers. This effect is another reason that the chemical properties are similar across the lanthanides.

The f-shell electrons and the generally similar chemical properties make the rare earths valuable ingredients in a wide range of materials. In particular, rare earth ion-doped insulating crystals play host to a variety of interesting effects relevant to many different fields. The parent compounds for these families of materials are usually some kind of yttrium compound which form transparent insulating crystals, with the optical, electronic, and magnetic properties tuned by replacing some or all of the yttrium with various rare-earth species. They are used as the lasing medium in several varieties of high-power lasers [EEA79], and in the context of quantum information they have been studied as quantum memories [Pro+15b] and microwave to optical transduction [Eve+19]. Beyond these devices, they also present unique

model systems for exploring a range of physical concepts.

The systems studied in this dissertation are based on the $LiYF_4$ system, which has the $CaWO_4$ Scheelite structure. The $LiYF_4$ family of materials are commercially grown as laser crystals using the Czochralski method, and hence fairly large and high-quality single crystals are easily available. Typical laser crystals in this family are predominantly yttrium, with 1-3% of the ions replaced with rare earths such as holmium or neodymium. The work here considers the opposite end of the compositional spectrum, focusing primarily on $LiHoF_4$ and secondarily on $LiErF_4$. The optical properties of $LiHoF_4$ are evident in an interesting behavior: the color will change based on the illumination. The crystal appears between a translucent yellow to pink depending on whether LED, incandescent, or fluorescent light is in use.

The nuclear properties of the Ho and Er rare earth ions seen here are also relevant. Holmium only has one stable isotope, ^{165}Ho, which carries a 7/2+ nuclear spin. There are two isotopes with half-lives in the thousands of years (^{163}Ho and ^{166m1}Ho) but these do not occur naturally and can be ignored. Erbium on the other hand, has six naturally occurring isotopes, with the most common ^{166}Er at 33.5%. Most of these natural isotopes have zero nuclear spin, except for ^{167}Er (23% abundance). Erbium 3+ is known as a Kramers' ion [JM91; Pro16], where the ground state is doubly degenerate.

1.1 Rare Earth ion Hamiltonian and models

One of the most well-known and fundamental models in quantum magnetism is that of the transverse field Ising model (TFIM). In such a model we have spins that can either be up or down ($|\uparrow\rangle, |\downarrow\rangle$) along the so-called easy axis, with some kind of interaction between them. Introducing a field transverse to the Ising axis allows for quantum tunneling between these two states. The Hamiltonian can written as [Dut+15; Sac11; McK23; Tab+08; MS18]:

$$\mathcal{H} = -\sum_{i<j} V_{ij}\tau_i^z\tau_j^z - \Delta_0\sum_i \tau_i^x, \tag{1.1}$$

where z is the easy axis, V_{ij} is the interaction strength, and Δ_0 represents the transverse field strength. This Hamiltonian has a critical temperature T_c above which the system

is disordered. It is also one of the simplest models with a quantum phase transition at a critical transverse field value Δ_c.

The materials that we will be discussing are notable as solid-state representations of magnetic models. The base material $LiYF_4$ is non-magnetic. However, as noted above, yttrium is chemically very similar to the lanthanides and hence it is possible to either partly or fully replace yttrium with another rare earth element. Depending on the element and base crystal, we can access a variety of magnetic model systems. In this work we look at crystals with 100% of the yttrium replaced with holmium ($LiHoF_4$) and one with 100% erbium ($LiErF_4$). The rare earth ions of holmium and erbium carry magnetic moments, while the rest of the lattice is not magnetic. Due to the different crystal electric fields of Er and Ho, the respective compounds have different magnetic symmetries. $LiHoF_4$ is a dipolar-coupled Ising ferromagnet with an easy axis, while $LiErF_4$ is a dipolar-coupled XY antiferromagnet.

We can first write a generalized Hamiltonian for all the $LiYF_4$-based crystals, then see how each ion produces such different properties. Each ion site has an electronic spin of $J = 8$ and the only isotope ^{165}Ho has a nuclear spin of $I = 7/2$. The complete Hamiltonian of the $LiHoF_4$ system is given by [Cha+04]

$$\mathcal{H} = \sum_i V_C\left(\vec{J}_i\right) - g_L\mu_B \sum_i B_x J_i^x + \frac{1}{2}\left(g_L\mu_B\right)^2 \sum_{i\neq j} \mathcal{L}_{ij}^{\mu\nu} J_i^\mu J_j^\nu \tag{1.2}$$

$$+ \frac{1}{2}\left(g_L\mu_B\right)^2 \frac{J_{ex}}{a^3} \sum_{i,nn} \vec{J}_i \cdot \vec{J}_{NN} + A \sum_i \left(\vec{I}_i \cdot \vec{J}_i\right), \tag{1.3}$$

with $\mu, \nu \in x, y, z$. The first term (with V_C) refers to the effect of the crystal fields, as in the electric field which the magnetic ions experience from the other atoms in the crystal. $LiHoF_4$ has a tetragonal Scheelite structure with 4 nearest neighbors. Using the Hund's rules, a Ho^{3+} ion has a ground state of $^5I_8$, ($S = 2, L = 6, J = 8$) [Cha+04]. An isolated Ho^{3+} ion will thus have a $2J + 1$ degenerate ground state. However, Coulomb interactions with nearby ions will create an electric field that splits the ground state. The particular form of V_c is given in terms of the Stevens operators [Ste52; JM91]. The general form is given by

$$V_c(\mathbf{J}) = \sum_i \sum_{lm} B_l^m O_l^m(\mathbf{J}_i), \tag{1.4}$$

where $O_l^m(\mathbf{J}_i)$ are the crystal field operators consisting of various J operators, and B_l^m are the crystal field parameters which depend on the relative locations of the other ions. In general, these are quite difficult to calculate, as the charge density is typically not distributed in a simple way, and because we are considering rare earth ions, the 4f electrons are screened by the outer electrons [JM91]. Thus, using a point charge model is not very accurate. However, the symmetry of the Scheelite structure means that only certain terms are relevant [Cha+04]:

$$\begin{aligned} V_C(\vec{J}) \;=\; & B_2^0 O_2^0 + B_4^0 O_4^0 + B_6^0 O_6^0 + B_4^4(C) O_4^4(C) \\ & + B_6^4(C) O_6^4(C) + B_4^4(S) O_4^4(S) + B_6^4(S) O_6^4(S). \end{aligned} \tag{1.5}$$

where the $O_l^m(\mathbf{J}_i)$ operators are given by [Cha+04]:

$$\begin{aligned} O_2^0 &= 3J_z^2 - J(J+1), \\ O_4^0 &= 35J_z^4 - 30J(J+1)J_z^2 + 25J_z^2 - 6J(J+1) + 3J^2(J+1)^2, \\ O_4^4(C) &= \frac{1}{2}(J_+^4 + J_-^4), \\ O_6^0 &= 231J_z^6 - 315J(J+1)J_z^4 + 735J_z^4 + 105J^2(J+1)^2 J_z^2 \\ &\quad - 525J(J+1)J_z^2 + 294J_z^2 - 5J^3(J+1)^3 + 40J^2(J+1)^2 \\ &\quad - 60J(J+1), \\ O_6^4(C) &= \frac{1}{4}(J_+^4 + J_-^4)\left[11J_z^2 - J(J+1) - 38\right] + \text{H.c.} \\ O_6^4(S) &= \frac{1}{4j}(J_+^4 - J_-^4)\left[11J_z^2 - J(J+1) - 38\right] + \text{H.c.}, \end{aligned}$$

where $J_+ = J_x + jJ_y$ and $J_- = J_x - jJ_y$, small j is the imaginary unit, and H.c. means hermitian conjugate [Cha+04]. These parameters B_l^m are usually determined by experiment, after eliminating some due to symmetry considerations. In Table 1.1 are two examples of experimentally derived crystal field parameters. We have used those of [Røn+07] for calculations here.

The next term is from the Zeeman effect of the applied transverse magnetic field B_x. The term with $\mathcal{L}_{ij}^{\mu\nu}$ represents the dipole interactions, given by the following tensor:

$$\mathcal{L}_{ij}^{\mu\nu} = \frac{\delta^{\mu\nu}|\vec{r}_{ij}|^2 - 3(\vec{r}_{ij})^\mu(\vec{r}_{ij})^\nu}{|\vec{r}_{ij}|^5}. \tag{1.6}$$

Citation	B_2^0	$10^3 B_4^0$	$10^3 B_4^4$	$10^5 B_6^0$	$10^5 B_6^4(c)$	$10^5 B_6^4(s)$
[HJN75]	-0.065	0.426	4.53	0.01	8.55	± 1.69
[Røn+07]	-0.06	0.35	3.6	0.04	7.00	± 0.98

Table 1.1: Crystal field parameters (i.e., coefficients for the Stevens operators) given in meV for $LiHoF_4$, as determined by the respective citations. In [HJN75], they measured these with susceptibility, and for the latter [Røn+07] they used neutron scattering.

This long-range interaction being the dominant coupling makes the $LiHoF_4$ system unique as a dipolar-coupled Ising magnet.

Next is the nearest-neighbor exchange coupling, with $a = 5.175$ Å being the lattice constant in the xy plane [Cha+04]. In theoretical treatments, J_{ex} is typically a free parameter to make T_c in the calculated phase diagram match experiment [DAS22]. Most calculations such as mean field predict $T_c \sim 1.8\,\mathrm{K}$ without this term, so this term is added to match experiment. Measurements [Røn+07] have found this to be $J_{12} = -0.1\,\mu\mathrm{eV}$. They found that this value fits well with the data, except at low-field and high-temperature near the classical phase transition where a value of $J_{12} = -0.27\,\mu\mathrm{eV}$ aligns better with the data.

Finally, the last term is the hyperfine interaction between the electron and nuclear spins on each site.

There is another interaction which has mostly been neglected in other work, but may prove relevant for more accurately describing the system, especially in regards to the spin waves and Walker modes we will discuss later. The Suhl-Nakamura effect [Suh58; HGB63] is an effective nuclear spin-spin interaction in ferromagnets and antiferromagnets. The Suhl-Nakamura interaction applies to systems with hyperfine coupling and electron spins coupled ferro- or antiferro-magnetically [Suh58; Nak58]. Each nuclear spin sees the electronic spin on the same atom through hyperfine coupling, and the electron spins are coupled with dipole and exchange interactions. This means that one nuclear spin excitation would couple to its electron spin, which creates a spin wave that couples to other electrons. Then, any electron affected by the spin wave can couple to its own nucleus, creating an indirect coupling between nuclei.

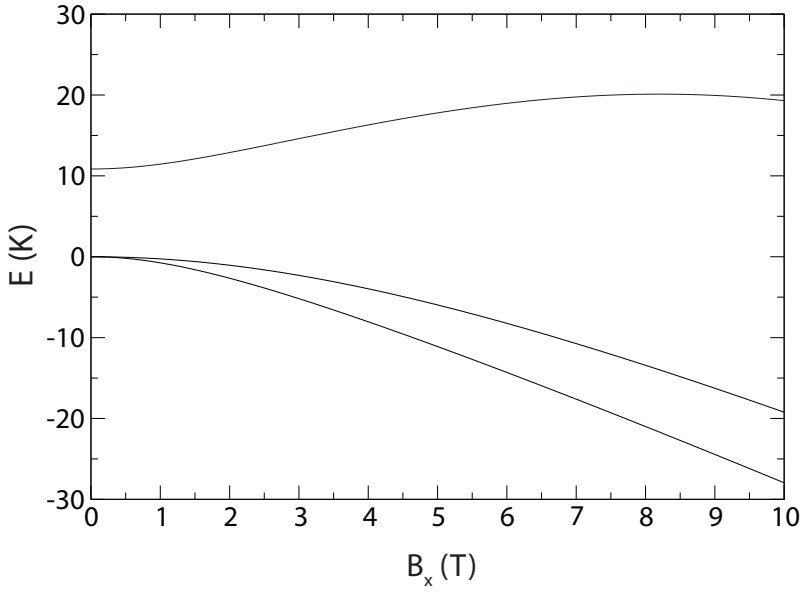

Figure 1.1: Electronic energy levels, showing the ground state doublet splitting with transverse field. At zero-field there is an approximate 11 K gap. This shows a much larger energy scale than the plots showing hyperfine levels, noting that 1 K = 20.8 GHz. Adapted from [Cha+04].

1.2 Effective Hamiltonian

This Hamiltonian includes all the relevant factors, but it is quite difficult to solve in this form. Thanks to the dipolar term, the state of spin i depends on every other spin, and each of those depends on the others... and so on. This Hamiltonian also includes the higher energy levels which might be relevant to laser applications at high temperatures. However, we are primarily interested in the low-energy modes at low temperatures. In this case, we can focus on the levels that give us the Ising behavior. Measurements have shown that the gap between the low-energy doublet and the first excited state is about 11 K (as shown in Fig. 1.1). Therefore, if we focus on the low-temperature and low-energy regime, we can consider a simpler truncated Hamiltonian for the Ising doublet, with components for the electronic and nuclear spins, i.e., $\mathcal{H}_{eff} = \mathcal{H}_e + \mathcal{H}_{NS}$ with terms for the electronic and nuclear spins, respectively [Tab+08].

We can treat the electron spins as a set of spin-$\frac{1}{2}$ Ising spins $\{\tau_i^\mu\}$. This leads to an effective field-dependent longitudinal electronic spin operator $J_i^z = C_{xx}(B_x)\tau_i^z$. The electronic Hamiltonian is thus [MS18]:

$$\mathcal{H}_e \;=\; -\sum_{i<j} V_{ij}(B_x)\;\tau_i^z\tau_j^z - \Delta(B_x)\sum_i \tau_i^x \tag{1.7}$$

where B_x is the transverse field, and $V_{ij}(B_x)$ now includes the truncated dipolar and exchange interactions between the Ising spins [McK+22]:

$$V_{ij} = \frac{1}{2}\left[J_D D_{ij}^{zz} C_{zz}^2(B_x) - J_{nn}\delta_{ij} C_{zz}^2(B_x)\right]. \tag{1.8}$$

$\Delta(B_x)$ represents the effective transverse field on each Ising spin. As indicated, these are both dependent on the applied transverse field B_x. The truncated nuclear spin bath Hamiltonian can be represented as

$$\begin{aligned}\mathcal{H}_{NS} \;=\; &\sum_i \mathbf{\Delta}_n \cdot \mathbf{I}_i + \mathcal{A}_z \sum_i \tau_i^z I_i^z \\ &+ \left(\mathcal{A}_\perp \sum_i \tau_i^+ I_i^- + \mathcal{A}_{++}\sum_i \tau_i^+ I_i^+ + h.c.\right)\end{aligned} \tag{1.9}$$

where $\vec{\Delta}_n = (AC_x, AC_y, 0)$, $A_z = 0$, and

$$A_\perp = A\frac{C_{xx} + C_{yy} + j(C_{yx} - C_{xy})}{4} \tag{1.10}$$

$$A_{++} = A\frac{C_{xx} - C_{yy} - j(C_{yx} + C_{xy})}{4}. \tag{1.11}$$

In this case the effective field $\vec{\Delta}_n$ comes from the hyperfine coupling and is anisotropic. The dependence of the matrix elements C_{ij} is shown in [MS18], in units of K and dependence on the transverse field B_x.

This truncated Hamiltonian $\mathcal{H}_\mathrm{H}$ is made up of the electronic term Eq. 1.7 and the nuclear term Eq. 1.9: $\mathcal{H}_\mathrm{eff} = \mathcal{H}_e + \mathcal{H}_{NS}$. This form shows the Ising behavior at low temperature.

Mean-Field Approximation

It is difficult to solve the $LiHoF_4$ Hamiltonian due to the interaction components. Relevant are both the exchange term between nearest neighbors and the dipole term which is especially difficult to handle because each ion is dependent on every other ion. For this reason, in order to solve the Hamiltonian we need to make some degree of approximation. The simplest of these is the mean-field approximation [Eis21]. The essence of this method is to ignore fluctuations of operators around the average value. This is introduced to the with the $\mathbf{J}_i \cdot \mathbf{I}_i$ term with some algebra to the identity [JM91]:

$$\mathbf{J}_i \cdot \mathbf{I}_i = (\mathbf{J}_i - \langle \mathbf{J}_i \rangle) \cdot (\mathbf{J}_j - \langle \mathbf{J}_j \rangle) + \mathbf{J}_i \cdot \langle \mathbf{J}_j \rangle + \mathbf{J}_j \cdot \langle \mathbf{J}_i \rangle + \langle \mathbf{J}_i \rangle \cdot \langle \mathbf{J}_j \rangle. \tag{1.12}$$

Or on a component basis, $J_\mu J_\mu \rightarrow 2J_\mu \langle J_\mu \rangle - \langle J_\mu \rangle \langle J_\mu \rangle$ where $\mu \in x, y, z$. This allows us to rewrite Eq. 1.3 at the mean-field level as [Eis21]:

$$\mathcal{H}_{\mathrm{MF}} = \underbrace{-\frac{n}{2} K \left(2\mathbf{J} \langle \mathbf{J} \rangle - \langle \mathbf{J} \rangle^2 \right)}_{\text{interaction}} + \underbrace{V_{\mathrm{CF}}(\mathbf{J}) + A\mathbf{J} \cdot \mathbf{I} - \mu_B \mathbf{B} \cdot (g\mathbf{J} + g_N \mathbf{I})}_{\text{single-ion}}. \tag{1.13}$$

This Hamiltonian can then be solved for the eigenvalues and eigenstates, as $\mathbf{E} = \mathcal{H}\Psi$. With the electronic spin $J = 8$ and nuclear spin $I = 7/2$, each one has $2N + 1$ states. The state is therefore defined by a vector of size $N = (2J + 1) \times (2I + 1) = (16 + 1) \times (7 + 1) = 136$. The Hamiltonian is an $N \times N = 136 \times 136$ matrix with the I_μ and J_μ taking the appropriate matrix form. This is calculated numerically in the mean-field form by guessing a $\langle \mathbf{J} \rangle$ value and refining until a self-consistent result is found [JM91; BD02; McK16; MS18].

We can also use the mean-field approach to calculate the phase diagram and demonstrate the effect of hyperfine coupling to the phase transition. This was calculated by Bitko et al. [BRA96] using the following equation:

$$\mathcal{H} = V_c - g_\perp \mu_B H_t \vec{J}_x + A \left(\hat{I} \cdot \hat{J} \right) - 2J_0 \langle \hat{J}_z \rangle \hat{J}_z. \tag{1.14}$$

There are some free parameters related to the coupling that are calculated using their measurements. The solution to this is shown in Fig. 1.2, with the susceptibility

measurements shown by circles. The dashed line is the result of omitting the hyperfine term in Eq. 1.14. This phase boundary shape is in agreement with that which is calculated for the basic toy TFIM, showing that $LiHoF_4$ is a good implementation of this model.

The solid line represents the calculation including the hyperfine term, which becomes most relevant below 400 mK. In this case, the electronic and nuclear spins are coupled to create a larger effective spin, increasing the transverse field scale needed to break the ferromagnetic ordering.

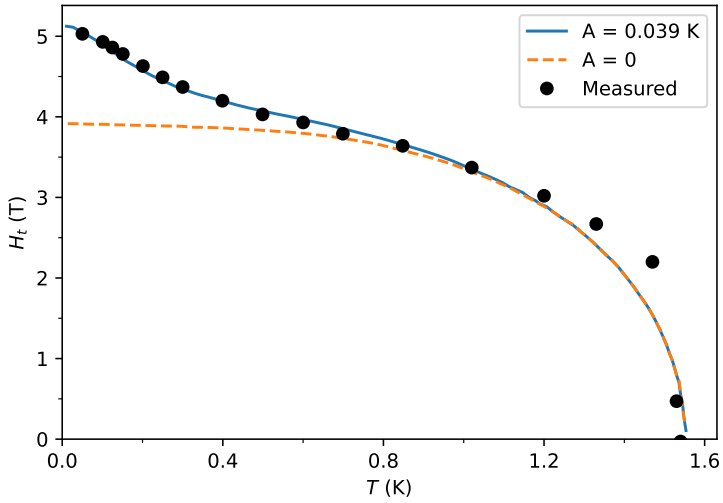

Figure 1.2: Phase diagram of $LiHoF_4$ adapted from [BRA96]. The dashed line is the mean-field solution of Eq. 1.14 without the hyperfine term ($A = 0$). The solid line is from the mean-field solution including the hyperfine term ($A = 0.039\,\mathrm{K}$). The dashed line is very similar to that expected in the simplest transverse field Ising model. In $LiHoF_4$ at low temperatures the hyperfine coupling to the nuclear spin becomes important and increases the energy scale (and thus transverse magnetic field) required to break ferromagnetic ordering. The circles represent susceptibility measurements by Bitko et al.

While the mean-field approach can account for most of the electronuclear dynamics in $LiHoF_4$, it does not account for the behavior near the quantum phase transition (QPT), where fluctuations become more important. For the next level of approximation, we use the Random Phase Approximation (RPA), which uses the mean-field results and allows a degree of fluctuations, assumed to be a gaussian distribution.

For the purposes of these experiments at low-temperatures and GHz frequencies, we

are interested in transitions between and within the two lowest electronic states which each have $2I + 1 = 2 \times \frac{7}{2} + 1 = 8$ states. Therefore this subspace has $2 \times 8 = 16$ states. The electron spin operator is then

$$\tau^z = \begin{bmatrix} 1 & 0 \\ 0 & -1 \end{bmatrix} \bigotimes \mathbf{I}_8 \tag{1.15}$$

where $\mathbf{I}_8$ represents the 8×8 identity matrix corresponding to the 8 nuclear levels, so this operator acts only on the electron spin.

The mean field susceptibility $\chi_0(\omega)$ can be solved analytically, and the RPA susceptibility follows as

$$\chi(\mathbf{k}, \omega) = \frac{\chi_0(\omega)}{1 - V_{\mathbf{k}}\chi_0(\omega)}. \tag{1.16}$$

The RPA modes are given by the poles of this function, and the residue of each pole determines the spectral weight. The lowest energy mode is one of these poles [McK16]:

$$\omega_k = \sqrt{\frac{\chi_0^{zz}}{\chi_2^{zz}}}\sqrt{1 - V_k\chi_0^{zz}}. \tag{1.17}$$

This gives the soft mode, completely softening to zero at $V_k\chi_0^{zz} = 1$. This can also be written in a spectral representation [McK+22]:

$$\chi(\mathbf{k}, z) = \sum_m \left[\frac{A_k^m 2E_k^m}{(E_k^m)^2 - z^2} \right] + \chi_k^{\text{el}}\delta_{z,0}, \tag{1.18}$$

where

$$D_{mp}^{\text{ret}} = \frac{-\omega_r}{\omega^2 - \omega_{mp}^2 + j\omega\Gamma_{mp}} \tag{1.19}$$

$$|S_{21}|^2 \propto Im[D^{ret}_{mp}] = \frac{2\omega\omega_r\Gamma_{mp}}{(\omega^2 - \omega^2_{mp})^2 + (\omega\Gamma_{mp})^2} \tag{1.20}$$

$$\tilde{J^z} = J^z - \langle J^z \rangle = C_{zz}(\tau^z - \langle \tau^z \rangle). \tag{1.21}$$

Susceptibility

Our focus is on the hybrid quantum system consisting of the resonator and the spin system. With models for the resonator physics and the microscopic Hamiltonian of $LiHoF_4$, the key to understanding the data is the interaction between the two. When there is strong coupling between the two systems, the excitations must be considered together.

In deriving the circuit model, the spin system is introduced as a susceptibility χ. Most studies of $LiHoF_4$ measure the low-frequency susceptibility χ [BRA96]. That is to say, the excitation frequency is much lower than electronic or nuclear energy levels.

Before proceeding, we should emphasize that in this context we are discussing the dynamic susceptibility, which is complex-valued and dependent on frequency, magnetic field, and temperature: $\chi(f, H, T)$. The real part of this quantity causes a dispersive frequency shift shaped similarly to the phase diagram. The imaginary part of χ has peaks corresponding to the transitions between electronic and nuclear levels. Discussions of this can be found in [McK16; JM91].

This distinction should be kept in mind throughout the following chapters, as it is not the same quantity measured in low-frequency experiments, although some behavior is similar.

1.3 Structure

So far, we have discussed the theory that is relevant to the rest of this work. Here is a short outline of the remainder of this work. Chapter 2 will describe the practical techniques for the experimental portions. Chapter 3 describes the initial experiments looking at the quantum phase transition in $LiHoF_4$ using loop-gap resonators (LGRs), which were published as [Lib+21a]. Further experiments with $LiHoF_4$ and descriptions of relevant theories, including magnon-polariton modes

and magnetostatic/Walker modes are described in chapter 4. The later chapters focus on other experimental systems. Chapter 5 discusses the material $LiErF_4$, which is similar to $LiHoF_4$ but with the holmium ions replaced by erbium ions. This gives us a XY (2-dimensional) layered antiferromagnet which can also be studied with microwave spectroscopy. We then take a slight detour in chapter 6 looking at ways to improve niobium superconducting resonators. Finally, in chapter 7 we look at future experiments that might use LGRs or superconducting resonators to explore dynamics in these systems. In particular, we discuss the possibility of saturating hyperfine levels in $LiHoF_4$ to move the QPT and allow a quantum quench to be observed. We will also connect this to the big picture through the Kibble-Zurek mechanism which describes after a quench—from galaxy clusters to microscopic Ising spins.

Chapter 2

Techniques

2.1 Microwave techniques

Microwave resonators for S-Band Measurements

Now that we have a theoretical understanding of the states involved in $LiHoF_4$, the question becomes how to measure and manipulate these states. The majority of relevant transitions are around 3 GHz, and mostly within the 2-4 GHz IEEE S-band. For typical magnetic resonance (MR, including nuclear and ferromagnetic resonance) and electron spin resonance experiments (ESR/EPR), there are a number of devices to transmit and receive an RF/MW field. A major determining factor is the frequency, and thus wavelength of the rf field. For lower frequencies (MHz) such as in most NMR experiments, a balanced coil is typical. As frequency increases, the inductance $j\omega L$ term gets too high, making a coil ineffective in the GHz range.

The other option is a microwave cavity, which becomes effective around 8 GHz and is often used in ESR. The simplest form of a MW cavity is a metal box with coupling antenna(s). The dimensions of the box are selected to match a particular quarter wavelength and thus frequency, from $\lambda = c/f$. This means that the dimensions of the cavity are inversely proportional to the desired frequency. For an idea of the size—a standard 12 oz soda can has a resonant frequency of 3.5 GHz. This brings multiple issues related to the size. First and foremost, the overall diameter would be too big for a superconducting magnet bore. The field profile also presents multiple issues. Less significant for small samples is the variable field strength throughout the sample. More importantly for these small samples is the resulting filling factor, a very important parameter which generally describes the magnitude of the effect that the sample has on the measured resonator properties. The filling factor for a material in/affecting an RF magnetic field can be defined as:

$$\eta = \frac{\int_{sample} dV H_1^2}{\int_{cavity} dV H_1^2}. \tag{2.1}$$

This is essentially indicating how much of the overall magnetic field is occupied by the sample, weighted by the field strength. Accordingly, if the sample has an effect on the resonant frequency and/or quality factor, the filling factor corresponds to how strong this effect will be [Che+04; ML08; CL82].

Another method that has been used to probe the $LiHoF_4$system is a coplanar waveguide (CPW) resonator, made with conventional conductors (copper) at a macroscopic scale [Kov16]. This is to be distinguished from the topic discussed in chapter 6, superconducting microresonators. Conventional CPW resonators have a fairly low quality factor, and the field profile causes issues at this scale. The MW magnetic field H_{mw} curves around the center conductor, meaning that the direction of H_{mw} is variable within the sample. The susceptibility of the sample is dependent on the direction of H_{mw} relative to the crystallographic axes, so CPW resonators will probe at many different angles throughout the sample. The measurements will include contributions from these different directions, making the analysis difficult and blurring out any features. This concept is called inhomogeneous broadening, and here also applies to the magnitude of H_{mw}. The effect of an inhomogeneous microwave field is most significant when studying saturation effects. If each region is experiencing a different field amplitude, only a fraction of the sample will be saturated at a given time.

Besides the inhomogeneous broadening effects, these CPW resonators will also have a much lower filling factor, as much of H_{mw} is outside the sample, above and below the substrate. This will make the coupling strength weaker and make it harder to see features.

Loop-gap resonator: Overview

Having discussed the most common resonator structures and their shortcomings for this measurement, we eventually came across a much more suitable design, the loop-gap resonator (LGR). It has properties of both lumped element resonators and cavity resonators, and it is practical for measurements of small samples at S-band frequencies. The LGR concept actually has its roots in some of the first microwave generators, starting from the development of microwave engineering

during World War II. A typical design consists of a central circular hole surrounded by flux return holes connected through thin gaps to the center hole [Bri85]. These cavity magnetrons were key components of the first radar systems and thus seen as critical to winning the war. A prototype being shared from Britain to Bell Labs “was called the ‘most valuable cargo’ ever to be imported into the US" [Bri85].

In the most basic form, an LGR can be made of a copper tube with a lengthwise slot [Col48; FH82]. In this case, the “loop," or inductive component, is around the perimeter of the round tube. This creates an RF magnetic field in the axial direction, along the tube. The small gap provides a capacitance with an electric field oriented across the gap. Because the resonant frequency is defined by these parameters rather than overall size, LGRs can be much smaller than the wavelength. This is in contrast to cavity and CPW resonators, where the physical size determines the resonant wavelength and thus frequency.

This most basic design of an LGR has some difficulties. First is the question of mounting. The axial flux through the center loop needs a return flux path, and in this case it is not confined and takes up the space around the resonator. This means that any conducting material placed in the vicinity of the resonator perturbs this field and changes the frequency. Therefore, the mounting materials in the vicinity of the LGR must be insulating. This would normally be plastic, which causes issues with thermal contraction relative to the metal and crystal sample.

Another consequence of this field profile is that it looks similar to a magnetic dipole. This causes significant radiation loss by the resonator. This also means that the resonator is very sensitive to the details of the enclosure farther away. When this is placed in a large metal can, the radiation loss and frequency are affected. Also, depending on the size of the enclosure and the exact geometry, the LGR may couple to a cavity mode. This type of LGR proved difficult to get working, probably due to these various factors.

While the most basic form of an LGR is impractical, with a slight variation we have found a much more reliable and effective resonator. Many problems related to the basic LGR design are due to the ill-defined flux return path. Fixing this problem is the key to make these measurements possible. Rather than a single loop and single gap, we can instead have multiple loops/gaps. An early example of this concept [WFH84] uses three loops connected by two gaps to provide a controlled return flux path and reduce the strong radiation loss associated with the single-loop resonator’s dipole field pattern. Additionally, this approach allows applying uniform

fields simultaneously at multiple frequencies, a key element for pump-probe and other state-manipulation protocols. Due to the flexibility in design, field uniformity, and optical access through the sample, resonators using this design are useful for a wide range of experimental studies, such as transduction between microwave and optical states in quantum computing applications [Bal+18].

Here, we describe an empirical design procedure using finite element method calculations to design an asymmetric loop-gap resonator with uniform fields at two frequencies in the same sample volume and analyze the field uniformity, frequency tunability, and filling factors, providing comparison to a manufactured device.

Loop-gap resonator: Design Requirements

When a sample with complex susceptibility $\chi = \chi' - j\chi''$ is inserted into a resonator, the reactive component χ' modifies the resonant frequency f_0 and the dispersive component χ'' modifies the quality factor Q:

$$\frac{\Delta f_0}{f_0} = \frac{\chi' H^2 \Delta v}{2\int_{res} H^2 d\tau} \tag{2.2}$$

$$\Delta\left(\frac{1}{2Q}\right) = \frac{\chi'' H^2 \Delta v}{2\int_{res} H^2 d\tau}, \tag{2.3}$$

where Δv is the volume of the sample [Che+04]. In ESR experiments, this susceptibility has a characteristic peak at an ESR transition. Off-resonance with an electronic level, this quantity probes the static susceptibility of the sample, providing information about the bulk magnetic properties of a sample [Che+04]. By contrast, studying the on-resonant response of a sample at multiple frequencies can provide information on the spin Hamiltonian [Mis11].

While multifrequency studies are typically performed by retuning a resonator and carrying out separate measurements, there are advantages to having a uniform field at two distinct frequencies simultaneously. For instance, many ESR experiments require temperatures of 0.1 K or below, and thus entailing the use of a ^{3}He/^{4}He dilution refrigerator. Cycling a dilution refrigerator to room temperature to retune a resonator can require hours or days, so the convenience of applying fields to a sample at multiple frequencies is considerable. More importantly, pump-probe spectroscopy with simultaneously-applied fields at two frequencies is a common technique [6]. However, little work has been done to develop a microwave resonator

that can produce uniform, resonantly enhanced, ac magnetic fields at frequencies spaced by a few GHz.

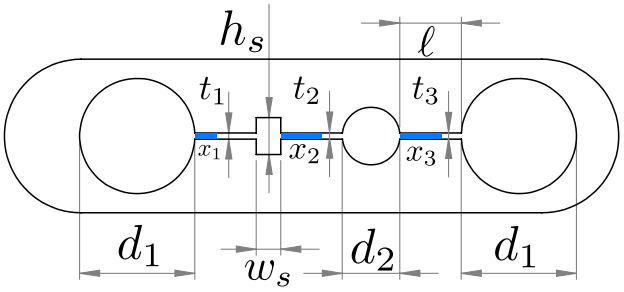

Figure 2.1: Illustration of the resonator design used in this work.

The resonator design studied in this work is shown in Fig. 2.1. This design is a variation of a typical four-loop three-gap resonator, with asymmetry introduced to provide degrees of freedom to control the mode splitting. One loop is rectangular to accommodate the rectangular single crystal samples often used in ESR and quantum magnetism studies. The dimensions of the rectangular loop are fixed by the sample size (here we use 4 mm x 2 mm), and we choose to fix the gap lengths ℓ_i at 5 mm. We also make the the gaps a uniform thickness $t = 330\,\mu\text{m}$, such that by introducing a sapphire shim into variable fractions x_i of the gaps it is possible to tune the gap capacitance post-fabrication.

In a three-loop two-gap design the outer loops serve as the return flux path for the center loop, so increasing the size of these loops enhances the flux density in the central loop. A similar principle applies here, so the outer loops are set as large as is practical. The size of the circular center loop plays a role in determining the relative filling factors of the two modes, as will be examined later.

The goals of our design are to optimize the field uniformity and filling factor for the rectangular loop while understanding the dependence of the mode spacing on these parameters.

Loop-gap resonator: Computational Analysis

A 3D CAD model of the empty resonator was constructed using SOLIDWORKS. The resonator body is made of copper with the loop and gap structure cut out and surrounded by a few mm of air on either side. To compute the resonant frequencies and corresponding field modes, a generalized eigenmode analysis is carried out

using an edge-based finite element formulation as implemented in EMWorks' high frequency simulator (HFWorks). This formulation ensures that no spurious modes are found and allows the use of the imperfect conductor boundary condition at the resonator's copper walls. To ensure higher precision of the resonant field distribution in the loop and gap regions, mesh refinement is used. Mode power normalization is also employed to produce proper field level comparison plots.

Fig. 2.2 shows the magnetic and electric field distributions of the two desired modes. While both modes have flux through the sample loop, a mode-splitting occurs because the return flux paths for the two modes are different. In the low-frequency mode, the magnetic fields in the two center loops oscillate in-phase, using the two loops on the ends as return flux paths, whereas for the high-frequency mode the return flux path is predominantly the second center loop.

The calculated electric field distribution is also qualitatively different between the two modes, with only the high-frequency mode having a significant electric field in the central gap. Fig. 2.3 shows the dependence of the mode frequencies on the three gap widths, with the low and high modes largely independently tunable using the right and left gaps, respectively.

The filling factor, defined as

$$\eta = \frac{\int_{sample} H^2 d\tau}{\int_{all} H^2 d\tau}, \tag{2.4}$$

is also an important parameter for sensitivity in spectroscopy and entering the regime of strong coupling between the resonator and a spin ensemble [Ang+16]. As mentioned previously, cavity and transmission line resonators have mode volumes tied intrinsically to the resonant wavelength, and thus have quite low filling factors for typical mm-size samples in the regime of a few GHz, making them impractical for spectroscopy in this range.

The filling factor is calculated here by numerically evaluating the integrals over a grid, with results shown in Fig. 2.4 for different sizes of the non-sample (circular) center loop.

A tradeoff in the filling factors of the two modes is apparent, due to the different return flux patterns. The low mode essentially sees each central loop acting as the return path for flux through each adjacent outer loop, while for the high mode the

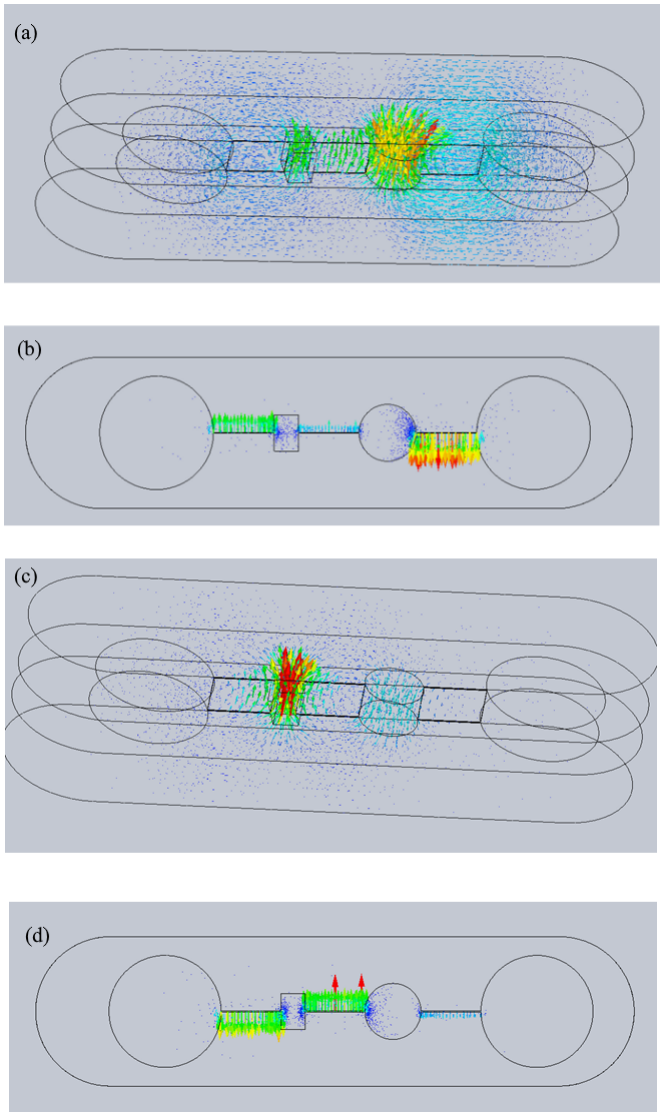

Figure 2.2: Calculated magnetic and electric fields of the low- (a,b) and high-frequency (c,d) modes.

sample loop predominantly serves as the return flux path for both the far-left loop and secondary center loop. This leads to a simple interpretation of these modes in terms of the three-loop two-gap structure discussed previously; in the lower mode, both center loops have the magnetic fields oscillate in phase and act as the single center loop in the three-loop two-gap geometry, while the higher mode corresponds to such a structure excluding one side loop.

The field uniformity within the sample volume is also important for uniform saturation of a spin ensemble [Ang+16]. In Fig. 2.5 cuts through the midplane of the sample

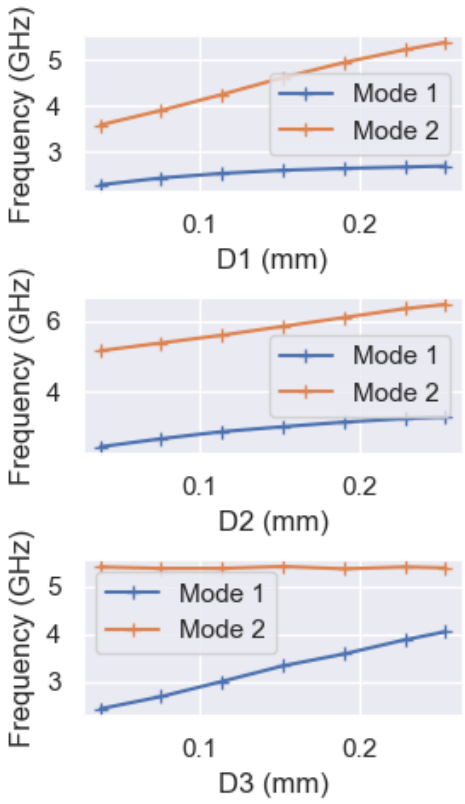

Figure 2.3: Calculated variation of the mode frequencies by tuning of the left, center, and right gap thicknesses. The low-frequency mode is largely insensitive to variation of the left gap while the high-frequency mode is independent of the right gap, allowing each mode to be tuned independently with dielectric loading post-fabrication.

volume are shown. The maximum variation of the magnetic field component perpendicular to this plane is approximately 3% for each mode, which is comparable to single-mode 3D lumped-element resonators [Ang+16].

Loop-gap resonator: construction and characterization

This style of loop-gap resonator presents manufacturing challenges. Using an endmill to cut the gaps is impractical given that the gaps need to be quite narrow compared to the material thickness. Slitting saws can cut narrow gaps, but they are fragile. There is another challenge in the shape of the central sample volume. For a nearly rectangular sample, the sample chamber should correspond to the shape to prevent magnetic torque. Interior rectangular pockets are difficult, with the squareness determined by the endmill diameter.

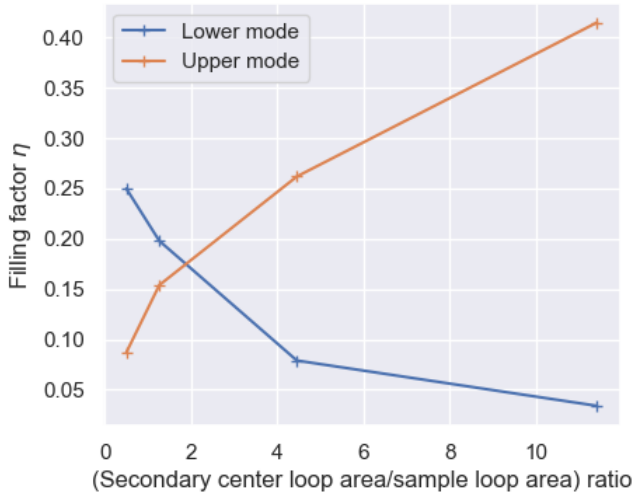

Figure 2.4: Variation of the filling factors of the two modes as the size of the circular center loop is varied, as a function of the ratio between the area of the sample loop and the circular loop. A tradeoff is apparent due to the different return flux patterns of the two modes.

One way to avoid these problems is to mill each half of the LGR at a time, with each half on its side. This makes the rectangular pockets easy to attain with a square endmill. The squareness will be determined by the kerf of the endmill which is small compared to the sample. Additionally, the gap can be formed by taking off extra material between the mating surfaces. The downside is that this approach introduces additional loss at the seam, by interrupting the loop current paths.

There is however a manufacturing process that solve these problems. Wire electrical discharge machining (wire EDM) allows for extreme precision cuts of conductive materials using high-voltage spark erosion. The workpiece serves as one electrode and a wire is the other. When there is a high voltage difference between the two, there is a spark which removes a small amount of material. The voltage is pulsed as the wire is moved, and the wire is unspooled during this process so it is not significantly eroded. A typical wire diameter is around 12 mils (0.3 mm), though they can be larger or smaller. This is effective for these LGRs, with a rectangular pocket and narrow gap.

A photograph of a resonator fabricated out of a single piece of oxygen-free copper using wire EDM is shown in Fig. 2.6. Coupling to both modes is via the electric and

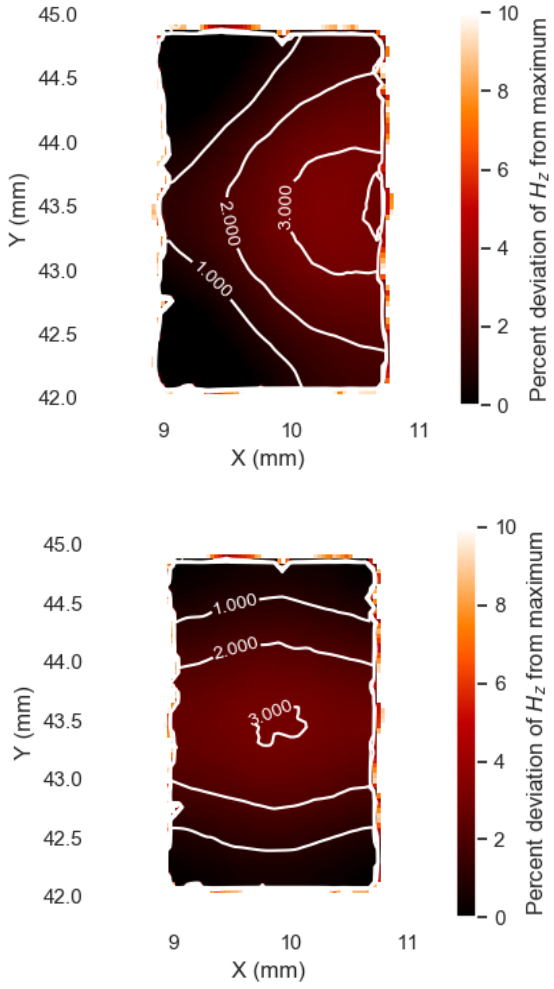

Figure 2.5: Contour plots of H_z within the sample volume for the low- (a) and high-frequency (b) modes.

magnetic fields of a pin extending from an MMCX connector, also shown in Fig. 2.6.

Experimental S-parameters are measured using a vector network analyzer connected to the two coupling pins. In practice, ultra-low temperature experiments must use lossy cables to reduce thermal conductivity to the cold stage, and cold attenuators between the source and resonator are necessary to reduce thermal excitation of microwave photons for experiments [Hue+13]. Attenuation from these make the reflected signal from the resonator weak and difficult to pick out from impedance mismatches in the cabling. Therefore, we only consider the transmission s_{21}, shown in Fig. 2.7 at a temperature of 80 K. The calculated and experimental data qualitatively agree, with quality factors of 800 and 300 measured for the low- and

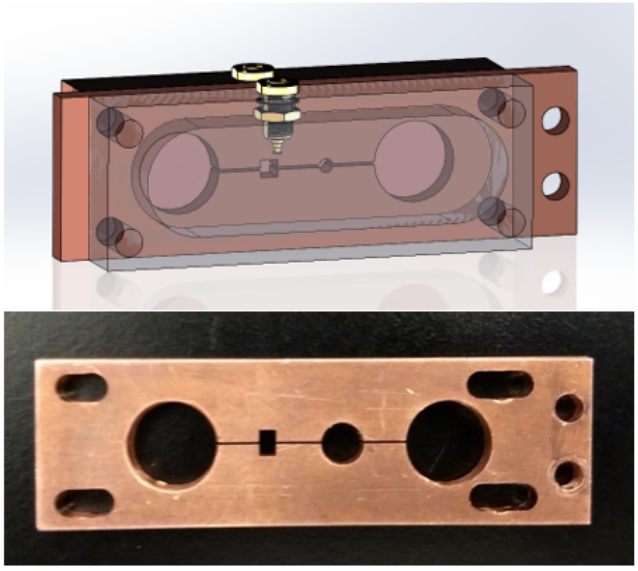

Figure 2.6: CAD model (top) of the resonator assembly including coupling pins and enclosure, and photograph (bottom) of the resonator manufactured using wire EDM.

high-frequency modes, respectively, at 80 K, with coupling pins approximately lined up with the sample volume. This device has been tested down to 30 mK and in a field above 5 Tesla. The quality factors increase slightly from room temperature to low temperature, but otherwise the performance of the resonator is not strongly dependent on temperature, and it remains mechanically robust and stable in strong magnetic fields as is needed for spectroscopy applications.

Elsewhere, analysis of a five-loop four-gap resonator mentioned the presence of multiple modes within the same volume [Eis18], indicating that variations of this basic design could be modified to support more modes with uniform fields.

Material measurements

A benefit of LGRs is that the MW electric and magnetic fields are mostly spatially separate: the magnetic field is confined to the loop/bore(s) and the and the electric field in the gap(s). This provides a significant benefit for measurements with crystals like $LiHoF_4$, where we only care about the MW magnetic field applied to the sample. Exposing such a crystal to the MW electric field would cause heating without relevance to this measurement. However, the property of LGRs that makes them useful is how the measurable resonator properties shift when the LGR is loaded with a sample. In this section, we will discuss how material properties are measured with

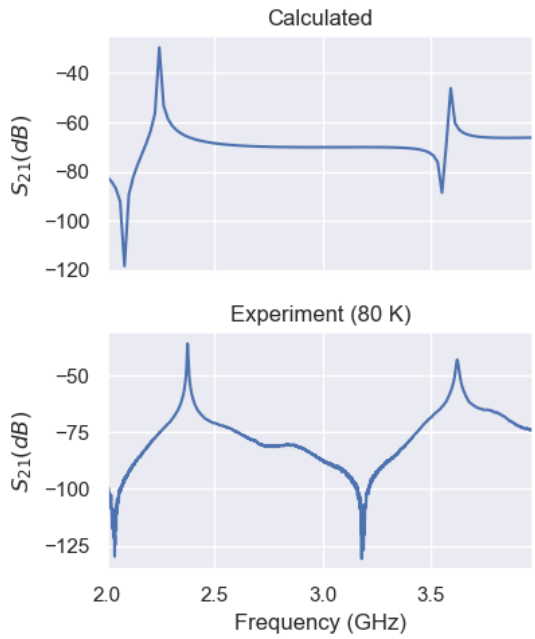

Figure 2.7: Calculated (top) and experimental (bottom) transmission of this resonator design.

LGRs.

While numerical modeling accurately predicts the intrinsic behavior of these 3-loop 2-gap resonators (3L2G), for physics applications it is helpful to develop an analytic approximation by considering an equivalent circuit model.

In this example we will consider the most basic type of LGR, the aforementioned tube with a slot cut along the axis (one loop, one gap, or 1L1G). The case for the M-loop N-gap we actually used is very similar (see Fig. 2.8), but the 1L1G has more simple analytic solutions for quantities such as the resonant frequency and the quality factor. A simple model is discussed in [FH82; Bob15], where we can derive the following for a 1L1G resonator. Modeling the empty resonator as an RLC circuit, the geometry causes the following capacitance and inductance, respectively:

$$C_0 = \frac{\epsilon_0 w \ell}{t}, L_0 = \frac{\mu_0 \pi r_0^2}{\ell}. \tag{2.5}$$

We can now calculate the empty resonance frequency:

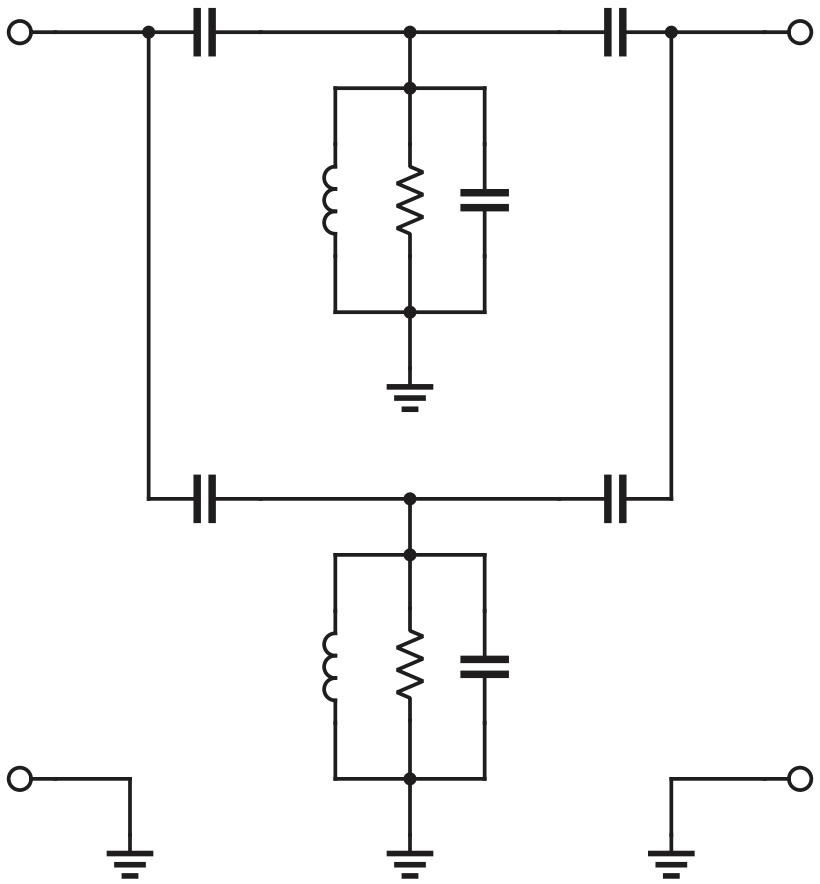

Figure 2.8: Circuit model of the 3-loop 2-gap resonator.

$$\omega_0 = 2\pi\nu_0 = \frac{1}{\sqrt{L_0 C_0}} \approx \sqrt{\frac{\ell t}{\epsilon_0 \mu_0 \pi w r_0^2}} = \frac{c}{r_0}\sqrt{\frac{t}{\pi w}}, \tag{2.6}$$

where $c = 1/\sqrt{\mu_0\epsilon_0}$ is the speed of light in vacuum.

For an LGR with an enclosure and design that suppresses radiation loss, the quality factor Q_0 of the unloaded resonator depends on the metal surface. High-frequency electromagnetic waves only penetrate a skin depth $\delta = \sqrt{2\rho/(\mu_0\omega)}$, where ρ is the LGR material's resistivity, and the depth becomes thinner at higher frequency. The unloaded quality factor is thus calculated as

$$Q_0 = \frac{1}{R_0}\sqrt{\frac{L_0}{C_0}} \approx \frac{x}{2\delta}, \tag{2.7}$$

where x corresponds to the side length of an approximately square inner loop [Bob18; HW81].

We can now look at how loop-gap resonators are used to measure material properties. The key is to look at how the electric and magnetic fields interact with the permittivity and permeability, respectively, of a sample. For $LiHoF_4$ we mainly care about the magnetic effects, as we can place the sample in one of the loops where the magnetic field is concentrated. If we have a material with susceptibility $\chi = \chi' - j\chi''$ inside the resonator, this will cause a shift in the quality factor Q and the resonant frequency f_0. Because the sample does not fill the entirety of the LGR magnetic field, we must introduce a filling factor η which describes how much of the given field is occupied by the sample [Su+23]:

$$\eta = \frac{\int_{sample} H^2 d\tau}{\int_{all} H^2 d\tau}. \tag{2.8}$$

The filling factor indicates how much the material modifies the effective inductance of the resonator, making the effective shifts [AT55; DB19; Kov16]:

$$\frac{1}{Q} = \frac{1}{Q_0} + \eta\chi'' \tag{2.9}$$

$$\omega \approx \frac{1}{\sqrt{L_0(1+\eta\chi')}} \approx \omega_0 \left(1 - \frac{\eta\chi'}{2}\right). \tag{2.10}$$

Vector network analyzer

To more quantitatively connect the measured behavior with the underlying response of the actual samples, we start by considering the transmission coefficient S_{21}. To define this parameter, we can look at a generic two-port network with port 1 and port 2. There are many ways to describe the scattering behavior of such a system, but the most relevant are the S-parameters. We start by defining waves going in and out of each port. The incident wave going in to port i is given by V_i^+ and the wave coming out of port i is V_i^- [Poz11; CC07]. The definition of an S-parameter is thus:

$$S_{ij} = \left.\frac{V_i^-}{V_j^+}\right|_{V_{k\neq j}^+ = 0}. \tag{2.11}$$

For the case of a two-port network, we can write the parameters in a matrix:

$$\begin{bmatrix} V_1^- \\ V_2^- \end{bmatrix} = \begin{bmatrix} S_{11} & S_{12} \\ S_{21} & S_{22} \end{bmatrix} \begin{bmatrix} V_1^+ \\ V_2^+ \end{bmatrix}. \tag{2.12}$$

When dealing with microwave circuits measurements are typically made in terms of power, as voltage and current are spatially inhomogeneous. However, the definition of S-parameters is in terms of voltage, so it is typical to convert power measurements as $P = V^2/Z_0$ where Z_0 is the characteristic impedance, typically $Z_0 = 50\,\Omega$. We can also write this as $V = \sqrt{PZ_0}$, so

$$S_{21} = \left.\frac{V_2^-}{V_1^+}\right|_{V_2^+=0} = \left.\frac{\sqrt{P_2^- Z_0}}{\sqrt{P_1^+ Z_0}}\right|_{P_2^+=0} = \left.\sqrt{\frac{P_2^-}{P_1^+}}\right|_{P_2^+=0}. \tag{2.13}$$

This means that the power ratio is equal to S_{21}^2. This relation is also important because it is typical to describe S-parameters in decibels. The ratio between two voltages V_1 and V_2 is [Poz11]

$$20 \log \frac{V_1}{V_2} \text{dB} \tag{2.14}$$

while the power ratio between P_1 and P_2 is

$$10 \log \frac{P_1}{P_2} \text{dB}. \tag{2.15}$$

I will also use this relation to specify absolute power levels. We can do this by specifying a reference power level for P_2, and the variable as P_1. This is most common using $P_2 = 1\,\text{mW}$ to give a value in decibel-milliwatts, or dBm:

$$10 \log \frac{P_1}{1\,\text{mW}} \text{dBm}. \tag{2.16}$$

In order to model the LGR spectrum, we can use other ways to model a two-port network which can then be converted to usual S-parameters [Poz11]. We shall

model an LGR with a sample in the loop with filling factor η and susceptibility $\chi = \chi' - j\chi''$. In these experiments, we use coupling pins which should lead to some degree of both electric and magnetic field, so they can be modeled as an inductance and capacitance coupled to the LGR.

We can model the LGR as a standard T-circuit, with the coupling components in series with each port signal pin, connecting to the LGR to ground as seen in Fig. 2.8. The impedances of the three components give the Z-parameters, which can be converted into S-parameters with the appropriate formulae [Poz11].

We make the assumption that the coupling impedances Z_1, Z_2 are equal. The coupling strength is determined by the physical placement of the pins which is nominally symmetric, varying slightly with how exactly each is soldered. Regardless, we are mainly concerned with transmission S_{21}, and this is a reciprocal system. Therefore, it doesn't matter which direction the measurement is made, i.e., $S_{21} = S_{12}$. It turns out that the coupling coefficients κ_1 and κ_2 will only appear in a sum together $\kappa_1 + \kappa_2$ in the final transmission function S_{21} which verifies this.

The coupling impedance is the series combination of inductance L_c and capacitance C_c, so

$$Z_c = j\omega L_c + \frac{1}{j\omega C_c}. \tag{2.17}$$

Next, the impedance Z_3 is that of the resonator. We can treat it as a parallel RLC circuit. The resistance represents the internal loss of the resonator, given by $Z_R = R_{\text{res}}$. The capacitance of the gaps is denoted $Z_c = 1/(j\omega C_r)$. We can modify this term by introducing material in the gaps, such as sapphire. In analogy with the magnetic perturbation, $\epsilon_r = \epsilon/\epsilon_0$ [Che+04]

$$C = C_0(1 + \eta\epsilon_r) = C_0(1 + \eta\epsilon_r'(1 - j\tan\delta_e)), \tag{2.18}$$

in terms of the real part of relative permittivity ϵ_r' and the dielectric loss tangent $\tan\delta_e = \epsilon''/\epsilon'$, which are how materials are usually specified. For our purposes, the gap capacitance is adjusted before cooling down and is fixed throughout an experiment, so it can be treated as a constant. Finally, we have the inductor which is partially filled with magnetic material. L_0 is the empty inductance, and $\chi = \chi' - j\chi''$

is the frequency dependent susceptibility. Substituting this in, we see the effective inductance and resistance terms,

$$\begin{aligned} Z_L &= j\omega L = j\omega L_0(1+\eta(\chi' - j\chi'')) \\ &= j\omega L_0(1+\eta\chi' - j\eta\chi'') = j\omega L_0(1+\eta\chi') + \omega L_0\eta\chi''. \end{aligned} \tag{2.19}$$

The real part χ' will modify the inductive component, and the imaginary part χ'' gives a resistive loss due to the sample. Now, Z_3 is the parallel combination of Z_R, Z_L, and Z_C:

$$Z_3 = \left(\frac{1}{Z_R} + \frac{1}{Z_L} + \frac{1}{Z_C}\right)^{-1} \tag{2.20}$$

$$= \left(\frac{1}{R_{\text{int}}} + \frac{1}{j\omega L_0(1+\eta\chi') + \omega L_0\eta\chi''} + j\omega C\right)^{-1}. \tag{2.21}$$

Pozar shows how to convert between network topologies and parameters [Poz12]. In this case we have a tee-network and want to find the S-parameters. As an intermediate step, we use the ABCD parameters, simplifying with $Z_1 = Z_2 = Z_c$:

$$A = 1 + \frac{Z_1}{Z_3} = 1 + \frac{Z_c}{Z_3} \tag{2.22}$$

$$B = Z_1 + Z_2 + \frac{Z_1 Z_2}{Z_3} = 2Z_c + \frac{Z_c^2}{Z_3} \tag{2.23}$$

$$C = \frac{1}{Z_3} \tag{2.24}$$

$$D = 1 + \frac{Z_2}{Z_3} = 1 + \frac{Z_c}{Z_3}. \tag{2.25}$$

Then we can convert these ABCD parameters into S_{21}:

$$S_{21} = \frac{2}{A + B/Z_0 + CZ_0 + D} \tag{2.26}$$

$$= \frac{2}{1 + \frac{Z_c}{Z_3} + \left(2Z_c + \frac{Z_c^2}{Z_3}\right)/Z_0 + Z_0/Z_3 + 1 + \frac{Z_c}{Z_3}} \tag{2.27}$$

$$= \frac{2}{2 + \frac{2Z_c}{Z_3} + \left(2Z_c + \frac{Z_c^2}{Z_3}\right)/Z_0 + Z_0/Z_3} \tag{2.28}$$

$$= \frac{2}{2 + \frac{2Z_c}{Z_3} + \frac{2Z_c}{Z_0} + \frac{Z_c^2}{Z_0 Z_3} + \frac{Z_0}{Z_3}} \tag{2.29}$$

$$= \frac{2Z_0 Z_3}{2 + 2Z_c Z_0 + 2Z_c Z_3 + Z_c^2 + Z_0^2}, \tag{2.30}$$

$$\tag{2.31}$$

where $Z_0 = 50\,\Omega$ is the characteristic impedance, Z_c the coupling impedance and Z_3 the resonator impedance given by Eq. 2.21.

Time-resolved measurement setup

> This project benefitted from contributions by Hayward Melton during his SURF project, including Figure 2.9.

Most of these measurements throughout here have been taken using vector network analyzers (VNAs) (TTR506A, E5071C). These are very precise and well-suited to these measurements, automating the process of measuring S-parameters. However, being an integrated system means doing things differently is difficult. In particular, in discussing nonlinear spin-pumping experiments, we need to probe the material on a much faster time scale. Getting enough points for a reliable fit of resonant frequency and quality factor usually takes between say 100 ms and 3 s. Of course, this also precludes any other time-resolved measurement as well, such as spin echo among others.

When a resonator rings down after a pulse [Gyü+15], the power and voltage waveforms take the respective forms

$$p(t) = p_0 \exp\left(-\frac{t\omega_0}{Q}\right) \tag{2.32}$$

$$V(t) = \sqrt{p_0 Z_0} \exp\left(-\frac{t\omega_0}{2Q}\right) \exp(j\omega t), \tag{2.33}$$

where p_0 is the source power during the pulse, $\omega_0 = 2\pi f_0$, where f_0 is the resonant frequency, Q is the quality factor, and Z_0 is the characteristic impedance (usually $50\,\Omega$). These are related through the equation $P = V^2/R$ modified for a complex signal: $p(t) = V^*(t)V(t)/Z_0$. When taking the Fourier transform of this voltage signal, we get the same spectrum as we see on the VNA in the frequency domain. So, if we apply a pulse to the resonator and watch the ringdown, the Fourier transform of the ringdown signal contains the same information as the VNA acquires over a longer timescale, namely resonant frequency and quality factor.

The obvious solution would be to directly generate the GHz signal and monitor it on an oscilloscope. However, at these frequencies that becomes untenable. The relevant equipment would be very expensive, and the data would be difficult to manage and analyze. To solve this we have developed a system to transform the low-frequency signals to and from the gigahertz signals. This is fairly similar to what VNAs do internally, but instead we can control the signals directly.

The basic principle is to use frequency mixers which effectively multiply two signals. A fixed microwave source is used as the local oscillator (LO) for each mixer [Poz11], and an intermediate-frequency (IF) port is a low frequency signal that the mixer can use as an input or output to modulate or demodulate the combined signal denoted RF. In this case, we use mixers to demodulate the resonator signal. Suppose the LO signal is given by

$$v_{LO}(t) = \cos(2\pi f_{LO} t) \tag{2.34}$$

and the

$$v_{RF}(t) = \cos(2\pi f_{RF} t). \tag{2.35}$$

Thus, when we multiply the LO with the RF signal from the resonator the trigonometric identity $\cos\theta\cos\phi = [\cos(\theta-\phi) + \cos(\theta+\phi)]/2$

$$v_{IF}(t) = v_{LO}(t)v_{RF}(t) = K\cos 2\pi f_{LO}t \cos 2\pi f_{RF}t \tag{2.36}$$

$$= \frac{K}{2}\left[\cos 2\pi(f_{RF} - f_{LO})t + \cos 2\pi(f_{RF} + f_{LO})t\right]. \tag{2.37}$$

In order to test this measurement setup we could use $LiHoF_4$, but in order to get a sharp signal we need to cool it near 100 mK. For a simplified test of these electronics, we can use an EPR reference standard which is useful at higher temperatures. A very common EPR reference standard is 2,2-diphenyl-1-picrylhydrazyl, more commonly known as DPPH [LD].

$$h\nu = \Delta E = g_J\mu_B B_0 \tag{2.38}$$

We purchased DPPH from Alfa Aesar, supplied as a black (slightly purple, especially in solution) powder. We mixed a small amount of the powder with Apiezon N grease and placed it in an LGR. We used a piece of sapphire that went through the sample loop, and put the grease where the sapphire is in the sample loop. This helps it stay in place where the MW magnetic field is strongest. A traditional EPR spectrometer would likely put the material in an aqueous solution in a glass tube, but that is not practical with this design.

2.2 Cryogenic techniques

PPMS Microwave insert

The experiments discussed here require operation at cryogenic temperatures, with $LiHoF_4$ferromagnetic state requiring 1.5K for magnetic ordering and 100 mK or below to study the hybridized electronuclear modes, while the superconducting resonators need temperatures of order 2 K to function. As helium dilution refrigerators for accessing the sub-Kelvin regime require a fair amount of time and money to operate, it is useful to have a system that allows measurements to be taken much faster/cheaper at the expense of base temperature. For example, for mechanical testing, most thermal contraction/expansion effects are finished by 77 K.

The Quantum Design DynaCool PPMS provides these functions—with temperature control from roughly 1.6 K to 400 K and a magnetic field up to 9 T or 14 T for the two instruments available. The cryostat is self-contained and automated, requiring little

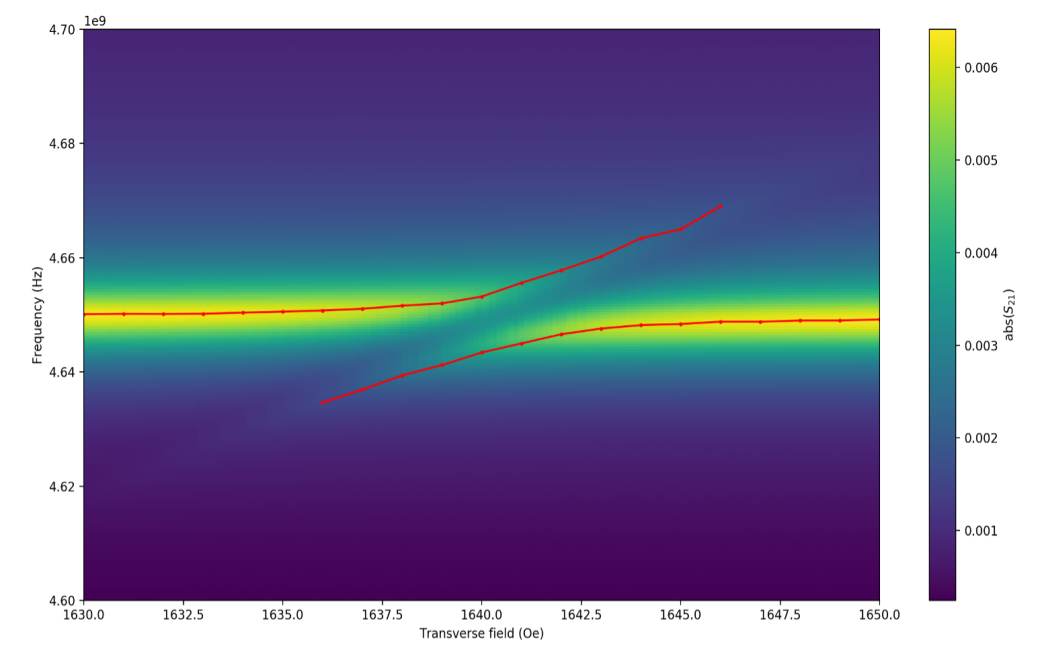

Figure 2.9: Transmission spectrum of DPPH in a loop-gap resonator, using the time-resolved ringdown technique.

more from the user than setting the temperature/magnetic field. The most basic way to load a sample is with the gold-plated copper puck with several pin connections. The operation involves a closed loop of helium liquid/gas which is cooled by a pulse tube refrigerator. This approach works down to around 10 K, at which point it pumps on the helium as in a 1K pot, allowing temperatures near 1.6 K. The primary method of heat transfer is through contact with the puck. Before use the chamber is purged with helium gas (a separate supply from the cooling loop). During use, the chamber retains a few mbar of helium for exchange gas.

In the stock configuration, measurements are made with the 12 pins on the bottom of the puck. However, these pins are only capable of DC measurements, without controlled impedance. Any experiment requiring different connections will need a way to get signals from the cold section at the bottom to a hermetic feedthrough at room temperature.

One important consideration is whether to measure in reflection or transmission, corresponding to one or two cables, respectively. Reflection corresponds to using one antenna on one side of the LGR and measuring S_{11} with a vector network analyzer (VNA) or utilizing a circulator and measuring S_{21}. In transmission, we simply add

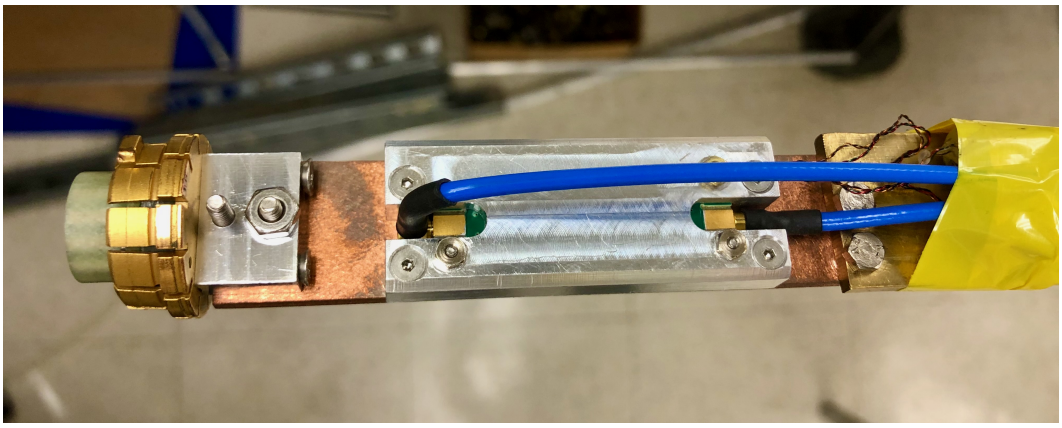

Figure 2.10: Insert used for high frequency measurements in the PPMS, here configured for a chip sample. The gold-plated copper and fiberglass part on the left is known as the puck, which plugs in to the bottom of the machine for thermal contact. Here the blue coaxial cables use SMP connectors to plug into the box, and go up to the stainless steel SMA cable. The copper backing plate seen here can be reconfigured for different sample holders. Note that the assembly must be quite compact to fit in the PPMS bore which has a diameter 1.06".

another pin antenna to the other side of the LGR and measure S_{21} with one antenna connected to the source and the other to the detector/receiver.

In the ideal case, either of these will work. However, we must also consider the properties of the cable materials, as they will be connecting cryogenic temperatures at the bottom to room temperature at the top feedthrough. While the cross-sectional area of the cables is small, materials with high thermal conductivity nonetheless have a strong effect on the base temperature of the sample at the bottom. Normal copper cable (RG-316) and aluminum semi-rigid cable were tried, but they failed to reach low temperatures.

Due to the Wiedemann-Franz law, a material with a low thermal conductivity will also have a low electrical conductivity, in this case causing more dB of loss. One exception to this is the case of superconductors, which have low thermal conductivity but when cooled below the critical temperature T_c they have high electrical conductivity. However, in this case the temperature of the cable between the ends is poorly defined and likely to fluctuate, making this unstable. Instead, we use semi-rigid coaxial cables with stainless steel inner and outer conductors (Micro-Coax UT-085-SS-SS). Using these, the PPMS is able to achieve temperatures below 1.7 K, similar to its capability without such cables mounted.

Dilution refrigerator

To study the low-energy dynamics in $LiHoF_4$, we need to access millikelvin temperatures. This is set by two considerations: thermal photons and the phase diagram. The thermal occupation of energy levels is proportional to the Boltzmann coefficient, $p_i = \exp(-E_i/k_BT) = \exp(-hf_i/k_BT)$, where h is Planck's constant, and k_B is Boltzmann's constant. To get a rough idea of the temperature required to not swamp the system with thermal photons, we can solve for the exponent equaling -1, i.e., $p_i = 1/e$:

$$\frac{-hf_i}{k_BT} = -1 \tag{2.39}$$

$$hf_i = k_BT \tag{2.40}$$

$$f_i = \frac{k_BT}{h} = T \times (20.8\,\mathrm{GHz}) \tag{2.41}$$

$$T = f_i/(20.8\,\mathrm{GHz}). \tag{2.42}$$

This means that for a 20.8 GHz transition, the system needs to be below 1 K in order to see a reasonable absorption (i.e., high spectral weight). The energy levels we are interested for $LiHoF_4$ are of the order 3 GHz, giving an estimate of $T = 3\,\mathrm{GHz}/(20.8\,\mathrm{GHzK^{-1}}) = 144\,\mathrm{mK}$. Additionally, the regime of the $LiHoF_4$ phase diagram where the hyperfine coupling causes the upturn is around 400 mK.

Considering these factors, we need to reach temperatures below 100 mK. These measurements on $LiHoF_4$ and $LiErF_4$ systems were taken in a KelvinoxMX250 helium dilution refrigerator (Oxford Instruments, UK). This system uses a closed cycle of helium-4 and helium-3 isotopes. The sample resonator is mounted on a long cold finger to the magnet center, surrounded by the inner vacuum can (IVC) which is sealed with indium wire holding the sample volume in vacuum at base temperature and a radiation shield (to block 4 K thermal radiation from the IVC). The IVC is placed inside the dewar of liquid helium, which also cools the superconducting magnets.

The cooling is started by pumping on a small volume of liquid helium from the dewar which causes it to cool to around 1.2 K, thus giving it the name 1K pot. Then the ^{3}He-^{4}He mixture is injected through the 1K pot and a flow-limiting impedance, where it cools down enough to condense. Once it condenses, the mixture undergoes a phase separation between ^{3}He-rich and ^{3}He-poor states. The physical construction

is such that the liquid surface sits within the still, and the phase boundary is in the mixing chamber. The mixing chamber is the coldest point, where samples are mounted. ^{3}He is unique in having a non-zero vapor pressure at very low temperature, and by pumping the ^{3}He gas off the still (similar to distillation, hence the name), ^{3}He moves through the mixing chamber phase boundary and removes heat through the entropy of mixing.

DR mounts

$LiHoF_4$ presents several challenges for measuring at cryogenic temperatures in a magnetic field. It is quite brittle and lacking in mechanical strength. Cooling to cryogenic temperatures introduces the issue of differential thermal contraction. $LiHoF_4$ has a coefficient of thermal expansion that is much lower than that of the copper LGR. Magnetic field experiments below the critical temperature exacerbate this with magnetic forces, especially as the strongest fields will be applied transverse to the Ising axis.

These two effects present contradictory requirements: free space around the sample for clearance from thermal contraction, but a tight fit to prevent motion in the magnetic field. Additionally, the sample should have good contact with the copper to allow heat transfer. The vast majority of the thermal contraction occurs between 300 K and 77 K; the contraction from 77 K to mK is usually negligible [GBG80; Eki06].

Making the copper hole big enough to leave an air gap around the sample would make it loose at room temperature. Loading the fridge involves attaching it to a gantry hoist, raising it up and moving it along the gantry track before lowering it into the dewar. All the while, the fridge will inevitably have some pendulum motion, with the LGR/sample at the bottom. So, the sample must be securely fixed at room temperature. There is a way to take advantage of different coefficients of thermal expansion (contraction) so that from room temperature to base temperature there is enough pressure to hold the sample in place, but not enough to crack it. This is to insert the sample with a small amount of Apiezon N grease to the square loop, and then add layers of Teflon shim stock to one side in each dimension, until the sample stays in place when tilted, but can be pushed out with light force. As Teflon has a large coefficient of thermal expansion, a suitable thickness of shim stock plus the sample has a total coefficient of expansion comparable to that of copper, allowing the assembly to be stable throughout the entire loading and cooling process.

Split coil

In order to make accurate measurements of a magnetic material like $LiHoF_4$, we must precisely control the field along the longitudinal and transverse (c) axis. The system already had a large solenoid magnet that can provide a sufficient transverse field, so the Ising axis of the sample must be perpendicular to the solenoid axis. This means that in order to apply a longitudinal field along the Ising axis, a solenoid is not possible and instead we must use a split pair of coils in a Helmholtz configuration. The pair could either go inside or outside the solenoid. Coils inside the solenoid would be closer to the sample and this have a higher field-to-current ratio, but the space is quite limited and it could be quenched by the solenoid, perhaps limiting the useful field range.

Instead, putting the split coil outside the solenoid turns out to be more practical. I had two bobbins made out of aluminum, with central mounting holes and mandrel. A notch is cut deep radially, leaving walls on either side. To wind the coil, we use superconducting wire, which has 35 strands of niobium-titanium (NbTi) in a copper matrix for mechanical reliability and thermal conductivity. The wire is supplied by Supercon, Inc., with a Copper:Superconductor ratio of 1.3:1. The bare wire is 0.40 mm diameter, and 0.430 mm diameter with insulation[1].

This is wound around the mandrel with a coil winding machine, with one wire end sticking out. The coil winding machine moves side to side to evenly fill the bobbin. In principle this axial motion can be adjusted so that the wire is laid side to side with minimal gaps, which puts each wire in even layers offset by a wire radius in order to use the space above and in-between the previous layer's wires. This allows fitting the most wires possible, filling about 90.7% of available space [MWS]. However, this quickly becomes impractical after a few layers, so instead we use "jumble winding" which results filling around 73-80% of the space [MWS].

A very important factor while winding is putting sufficient tension on the wire. For this purpose I used a magnetic tensioner which uses an eddy current brake to prevent the wire from having slack and becoming loose in the coil. While spinning the mandrel, the winder moves the wire outlet left and right. I applied epoxy during winding in order to keep the wires in place under tension. I made a Teflon "spreader" to apply the epoxy evenly, making sure that there are no gaps between wires which might move at high current.

[1] Part number SC-54S43-0.4mm

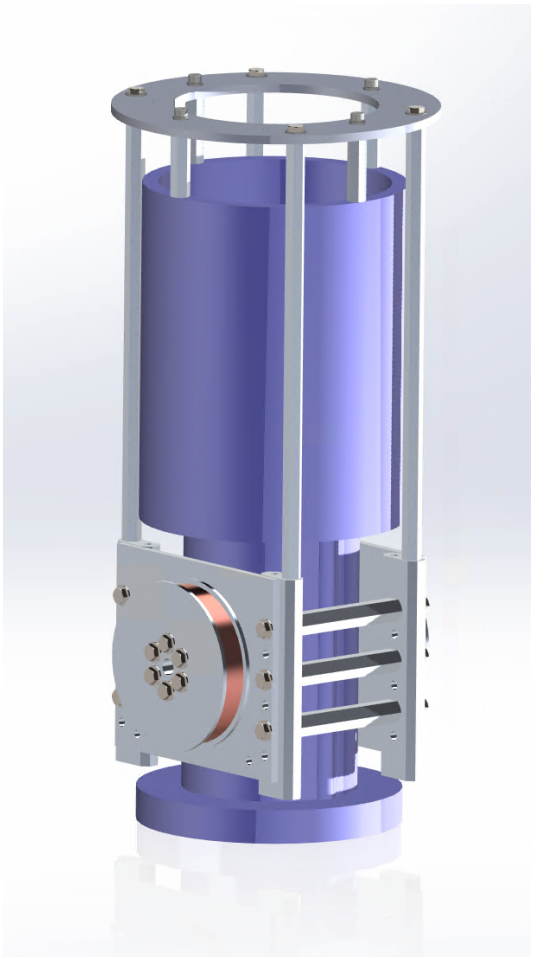

Figure 2.11: Model of the split coil assembly clamped around the solenoid magnet (blue). Superconducting wire is wound in the bobbins on each side attached to plates. Internally threaded standoffs go between the plates and to the upper mounting plate to keep the assembly attached securely.

Each coil was finished at a nominal 3181 turns. I used a program called "loopfield" [Yap23] which calculates the magnetic field of the coil as the superposition of 3181 turns distributed in the bobbin space. The essential parameter we must know about the magnet is the field to current ratio, as the magnetic field is linearly dependent on current. This was both calculated in loopfield and measured using a 3-axis MEMS magnetometer. These both agreed well at

$$B/I = 8.56\,\mathrm{mT/A}. \tag{2.43}$$

While the jumble winding means the turns are not distributed uniformly, this

calculation matched the measured value quite well.

This wire is fairly thick and thus is rated for very high current (and thus field). On its own, the split coil could in principle run with 210 A, for about 1.8 T. This would be quite extreme, but there are limiting factors come from other sources. One is the copper wiring to room temperature, and the feedthrough that connects to it. Also, since these coils surround the solenoid, it is important to make sure the total field applied to the solenoid is not beyond its limit. We have used a practical limit of around 0.5 T, or about 58 A.

The coils are mounted with screws through the mandrel on an aluminum plate. This is then attached to other aluminum spacers and rods which suspend it from the magnet support plate.

Chapter 3

Quantum Phase Transitions in a Model Magnet

This chapter is predominantly adapted from [Lib+21b].

3.1 Introduction

Quantum phase transitions (QPTs) are zero temperature transitions whose critical behavior and fluctuation spectra reveal fundamental properties of technologically useful electronic, magnetic, and optical materials. Canonical examples [Her76] include the ferromagnet-paramagnet transition in metals, and the quantum Ising model, which describes a set of mutually interacting spin-$1/2$ systems in an 'easy axis' crystal field, with quantum fluctuations controlled by an effective field Γ perpendicular to the easy axis. Many systems in physics and elsewhere can be mapped to the Ising model in transverse field [Jur+17; NN96; McA+20; SIC13]; recent interest has focused on quantum computing applications [AL18; Boh+16; Ber+17; Kin+21]. The model is predicted [Her76] to have a single spin wave collective mode, whose energy softens to zero exactly at the quantum critical point (QCP).

Although theory predicts that the soft mode must exist, it has never actually been seen near the QCP in any real Ising spin system. One reason for this is defects and paramagnetic impurities, which have a profound effect on QPTs [Ji+21]. Nuclear spins have a more subtle effect. Many experiments on crystals of transition metal-based magnetic molecules, both in the quantum relaxation regime [GSV06], and the high field, low-T regime where spin waves can propagate [Tak+11], show that the nuclear spins act as a slowly fluctuating random field [PS98; PS00], which destructively scatters any soft electronic collective mode.

Rare earth quantum Ising systems have much stronger hyperfine fields, with obvious effects in, e.g., $LiHo_xY_{1-x}F_4$ [Røn+07; Gir+01; Cha+04]. Theory then suggests [SS05; MS18] that the pure $LiHoF_4$ system actually should have 15 coherent

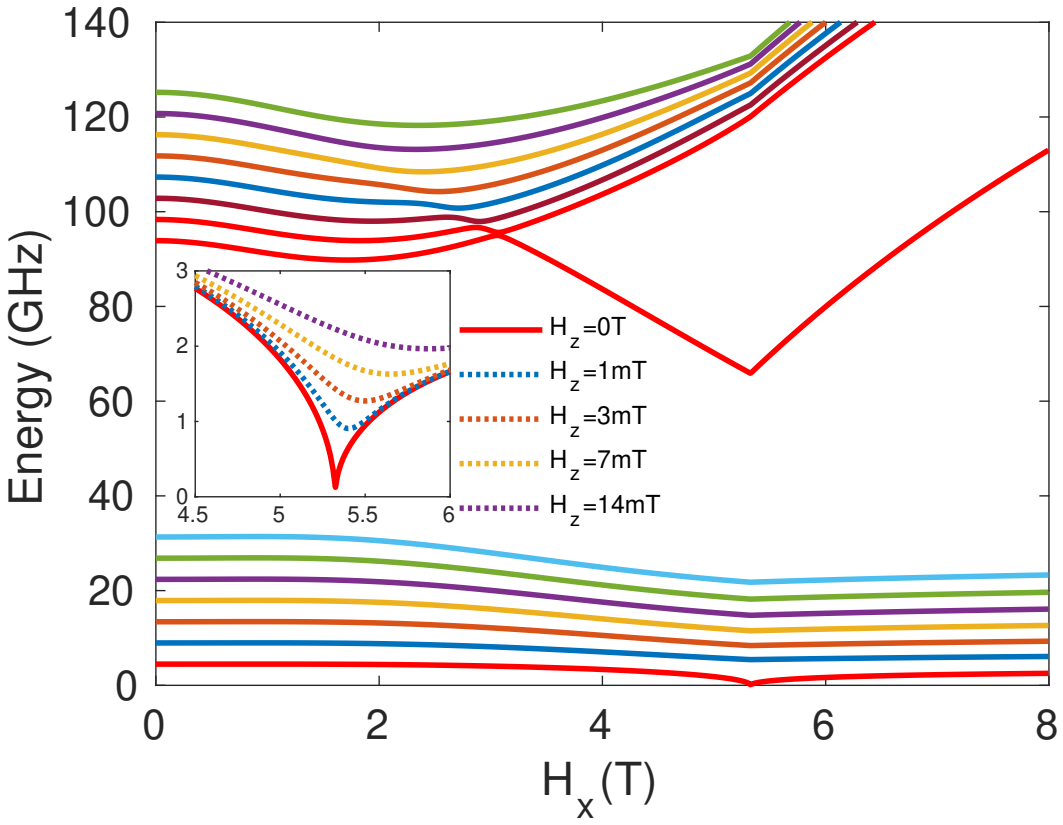

Figure 3.1: Random Phase Approximation (RPA) calculation of the electronuclear collective mode spectrum at momentum $\mathbf{k} = 0$ and temperature $T = 0$, as a function of transverse field H_x, for a long cylinder of $LiHoF_4$. The quantum critical field $H_C \sim 5.3$ T in the calculation. The modes divide into upper and lower groups; at high fields a mode splits off from the upper group. Inset: close-up of the region around the QCP, showing the effect on the soft mode of a small uniform longitudinal field H_z.

electronuclear modes. Instead of scattering the electronic mode, the spin-7/2 Ho nuclear spins hybridize with it to create these modes; similar hybridization has been observed in transition-metal antiferromagnets such as $CsMnI_3$ [Pro+97]. Nonetheless, previous neutron experiments looking for collective modes in this system [Røn+05] (where there is clear evidence for quantum critical scaling near the QCP [BRA96]) found only a gapped electronic mode, and no soft mode.

The previous theory [SS05; MS18] is easily generalized to include the effects of finite T and a small applied longitudinal field H_z [Lib+21c]. Salient features, illustrated in Fig. 3.1, include (i) the splitting into upper and lower groups; (ii) the softening of the lowest mode to zero energy when $H_x = H_c$, the transverse field at the QCP; and (iii) the extreme sensitivity of this soft mode to any longitudinal field H_z, which

immediately gaps the soft mode around the QCP (Fig. 3.1). This last feature has not been discussed previously, and will be of key importance.

Here we describe an experiment on a crystalline sample of $LiHoF_4$, of rectangular prism shape (dimension $1.8 \times 2.5 \times 2.0$ mm^3), at temperature $T \sim 50$ mK, well below the splitting ~ 220 mK between adjacent Ho hyperfine levels. Instead of neutrons, microwave spectroscopy was used, in the frequency range $0.9 < \omega < 5.0$ GHz, to measure AC absorption as a function of ω, T, and applied transverse field H_x. A resonator structure is required to amplify the applied ac signal. In order to obtain a high quality factor Q and field homogeneity, we adopted a tunable loop-gap resonator (LGR) design [WFH84; LSK19b; Lib+21c]. The resonant frequencies are tuned by varying the gap capacitance, via partial or complete filling with pieces of sapphire wafer. The incident power level was restricted to ~ 1 μW (-30 dBm) at the resonator. At this level, sample heating was negligible and the sample was well into the linear response regime.

The spectral weight of the soft mode is predicted to be strongest in the χ^{zz} configuration [SS05; MS18]. This counter-intuitive result is a crystal field effect, and is one reason why the mode was not seen in previous experiments [Kov+16]. In our setup the resonator and sample are oriented with the AC probe field along the Ising z-axis, a solenoid along the transverse x-axis, and a split coil along the z-axis. In this geometry, crystal fields reduce the AC soft mode absorption along y to zero at the QCP.

Results and Analysis

Figs. 3.2 and 3.3 show the measured transmission of single-crystal $LiHoF_4$ in LGRs tuned to different resonant frequencies at T= 55 mK. When the resonant frequency Ω coincides with the soft mode frequency ω, absorption is enhanced, giving a peak in the resonator inverse quality factor $1/Q$ (insets). In Fig. 3.2 the resonator is tuned to the lowest accessible Ω = 930 MHz. In this regime, the field-dependent evolution of the cavity resonant frequency is driven primarily by the change in the static susceptibility of the $LiHoF_4$ crystal. By varying Ω we track the soft mode close to the QCP. In Fig. 3.2 we probe this mode at higher Ω and find two peaks bracketing the 4.8 T QCP, demonstrating that the mode does persist as expected into the paramagnetic phase.

When $\Omega > 2.8$ GHz, the collective mode-cavity mode coupling is strong enough for detection well away from the cavity resonant frequencies (Fig. 3.3 (a,b)). We

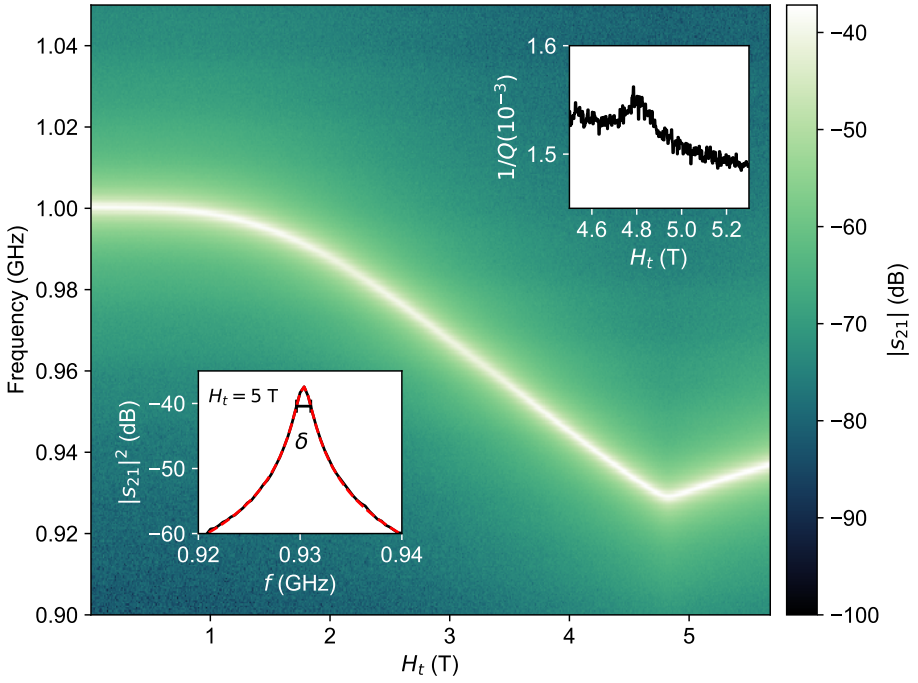

Figure 3.2: Resonant absorption probing a low-energy excitation mode: Transmission magnitude $|s_{21}|^2$ vs. frequency f and transverse magnetic field H_x for a single-mode LGR with zero-field tuning of 1.0 GHz. As the static susceptibility of the $LiHoF_4$ sample increases with H_x, the effective inductance of the resonator + sample circuit increases, resulting in a decreasing resonant frequency, with a cusp at the QPT at $H_C = 4.8$ T. Lower inset: individual frequency spectrum (blue) and Lorentzian fit (orange). Bar indicates the full-width half-maximum point used to determine the quality factor Q. Upper inset: $1/Q$ vs. H_x, showing enhanced dissipation when the energy of the soft mode matches the 0.93 GHz circuit resonant frequency.

ought to then observe transitions between all the collective modes, at frequencies equal to their energy differences. We use a linear combination of absorptive and dispersive Lorentzian lineshapes, to extract the frequencies and linewidths of these transitions. Near the cavity resonance at 4.2 GHz, the spectra were fit to a coupled oscillator model [Sch+10; Hue+13]; the apparent avoided level crossing at 3.6 GHz is an anti-resonance in the LGR response.

We plot in Fig. 3.4 the measured (top) and theoretically expected (bottom) transition energies. The blue points are derived from on-resonance measurements such as those shown in Figs. 3.2 and 3.3(c,d); the orange curve comes from the broadband measurement shown in Fig. 3.3(b). We note that it is essential to do a finite-T RPA

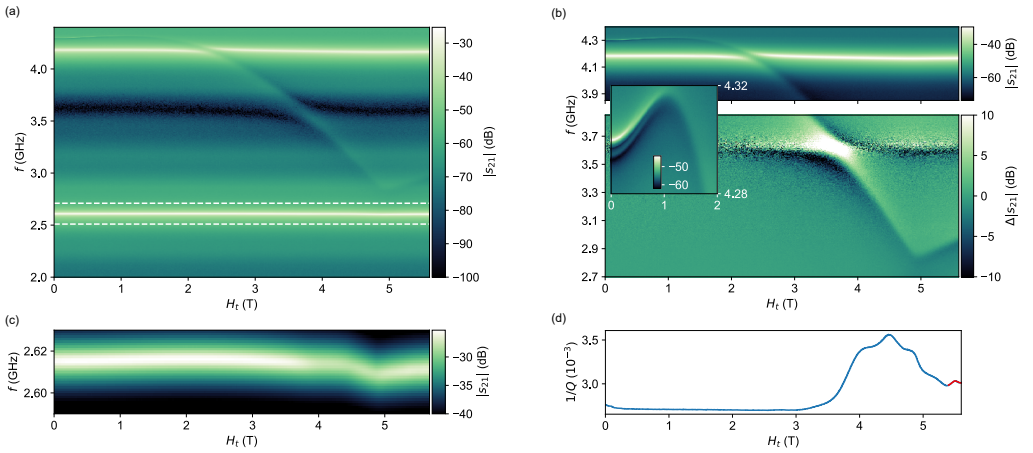

Figure 3.3: Resonant and broadband evolution of higher-energy excitation modes. (a) Transmission magnitude $|s_{21}|^2$ vs. frequency and H_x, with bimodal resonator tuned to 2.6 and 4.2 GHz. (b) Expanded view of the broadband transmission response. The field evolution of the first excited state response appears as a well-defined continuous curve well away from resonant modes of the LGR. Near the cavity tuning of 4.2 GHz and near an extraneous cavity mode at 3.9 GHz, avoided level crossings can be ascribed to hybridization between cavity photons and magnons. For enhanced contrast, the transmission between 2.7 and 3.8 GHz is plotted relative to a zero-field frequency dependent background −70 dB. Inset: Magnified view of transmission in the low-field region where the soft mode and excited states are expected to coincide. A few closely spaced modes are resolved; the non-monotonic shape is reproduced well by the RPA calculations. (c) Expanded view of the resonant response between 2.58 and 2.63 GHz (region between horizontal dashed lines in panel (a)). (d) Transverse field dependence of $1/Q$ for the resonant response shown in (c). At 2.6 GHz, peaks in $1/Q$ are observed above and below the 4.8 T QCP (red lines), indicating that at higher frequencies, the soft mode is visible on both sides of the phase transition.

calculation since both the transition energies and their spectral weights differ from their $T = 0$ values. At $T = 55$ mK, which corresponds to 1.15 GHz, one expects multiple transitions between thermally excited electronuclear states [Lib+21c].

At low transverse field, the three lowest excitation modes are essentially degenerate, resulting in a single curve. The insets to Fig. 3.4 show this behavior; the non-monotonic field dependence of the measured mode is accurately predicted by the model. The RPA calculations overestimate the critical field, primarily due to the absence of mode-mode couplings in the RPA (which, although individually small, have a cumulative effect on the critical field [MS18]).

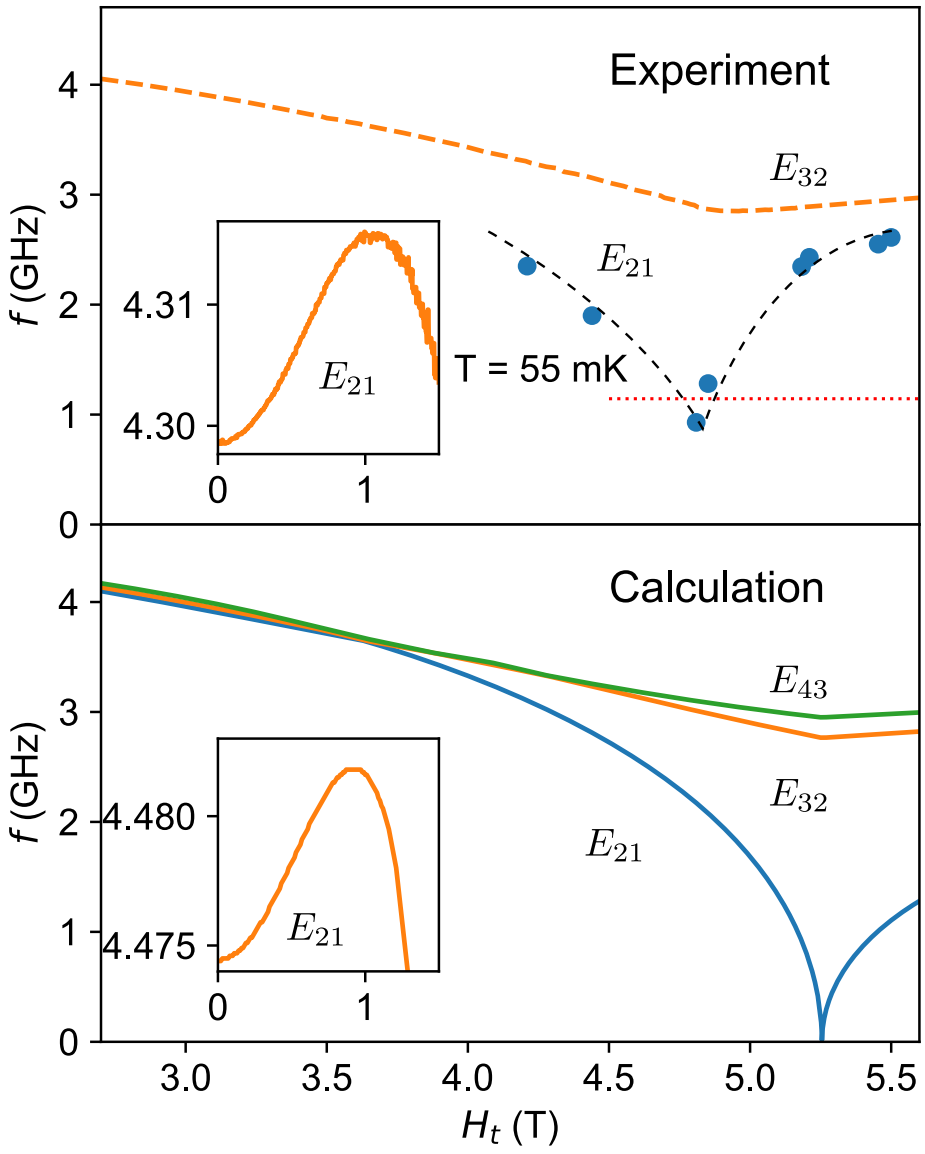

Figure 3.4: Measured and calculated excitation spectra. Top: Measured field dependence of soft mode (E_{21}) and excited state (E_{32}) spectra, at $T = 55$ mK, as determined by on-resonance (blue points, derived from Fig. 3.2 and Fig. 3.3(d)) and off-resonance (orange curve, derived from Fig. 3.3(b)) responses, respectively. The dashed-line curve through the E_{21} points is a guide to the eye. The horizontal dashed line is the frequency conversion of $T = 55$ mK. Bottom: Three lowest transition energies, calculated using a finite-T RPA. The field scale for the QPT differs by $\sim 8\%$. Insets: Measured and calculated frequency evolution at low field, where the three lowest modes are effectively degenerate. The energy scale for the measurement and model differ by $\sim 4\%$.

3.2 Longitudinal field

Another degree of freedom we can explore is a longitudinal field applied to the sample. The effect on the Hamiltonian is analogous to that of the transverse field Zeeman effect term:

$$\mathcal{H}_{long} = g_L \mu_B \sum_i B_z J_i^z, \tag{3.1}$$

where z (longitudinal) is along the Ising axis. We can do this using the split coil mentioned in Chapter 2. One effect of a longitudinal field is to reduce the transverse field value required to break the quantum ferromagnet state due to domain pinning and tunneling. The longitudinal field response allows us to distinguish between the different underlying causes of modes.

The theoretical result that any applied longitudinal field H_z will gap the soft mode means the domain structure and demagnetization field will play defining roles. In $LiHoF_4$ the electronic spin dipolar interaction is much larger than the superexchange interaction. One then expects many Ising domains, with thin low-energy domain walls and an almost uniform demagnetization field except very near the boundaries. This theoretical expectation is confirmed by the observation of micron-sized domains in optical Kerr and Faraday rotation experiments [Bat+75; Pom+88; MPF89]. The precise structure of the domains [KE60; GG85] is then not crucial: what matters is the relation between the mean magnetization density and the demagnetization field. If we model the system as a thick plate, then at zero wavevector, the soft mode is only affected by the average demagnetization field, which we incorporate into the RPA via an effective demagnetizing factor [Lib+21c].

The first step of these measurements is to establish a baseline ratio between the two magnets, to determine the tilt that compensates for slight mechanical misalignments. The sample and magnet are attached through many mechanical connections which cannot be perfectly aligned to each other, especially when considering thermal contraction when cooling down.

Another degree of freedom we can explore is a longitudinal field applied to the sample. The effect on the Hamiltonian is analogous to that of the transverse field Zeeman effect term:

$$\mathcal{H}_{long} = g_L \mu_B \sum_i B_z J_i^z, \tag{3.2}$$

where z (longitudinal) is along the Ising axis. We can do this using the split coil mentioned in Chapter 2. One effect of a longitudinal field is to reduce the transverse field value required to break the quantum ferromagnet state due to domain pinning and tunneling. The split coil response allows us to distinguish between the cause of modes based on how they are affected by the longitudinal field.

Due to the potentially hysteretic nature of the ferromagnet, two distinct field ramping protocols were investigated. First, as depicted in the right column of Fig. 3.5, the direction of the field vector is fixed and the amplitude ramped continuously from 0 to 6 T. Multiple overlapping peaks in the dissipation are observed (dashed curves in Fig. 3.5(c)). In order to classify these peaks, we plot their dependence on field angle in Fig. 3.5(e). The response of the low-energy soft mode is qualitatively different to that of the quantum phase transition, allowing the two features to be separated. As expected, the QPT (identified by the minimum in f_0, corresponding to the peak in the static susceptibility) depends only weakly on the longitudinal field, whereas the enhanced dissipation associated with the soft mode has a strong and approximately quadratic dependence on applied field (Fig. 3.5(e)). This dependence is seen for the mode both above and below the quantum critical point.

A second field-sweeping protocol was followed (right column of Fig. 3.5) to control for ferromagnetic domain effects. In this protocol, we start at high transverse field, sufficient to place the sample well inside the quantum paramagnetic phase. A longitudinal pinning field of 70 mT is applied, the transverse field is ramped down to the desired value immediately below the critical field, thereby driving the sample into the ferromagnetic state. The response of the $LiHoF_4$ sample is then measured as a function of longitudinal field as that field is ramped through zero to the maximum accessible negative field for our coil set. This process is repeated for a series of transverse fields, defining a grid in (H_l, H_t) parameter space. Cutting through the grid at a series of constant longitudinal fields yields the curves shown in Fig. 3.5(d), where we now see the phase transition and the soft-mode feature in the ferromagnetic state, but the initial pinning field has suppressed the soft-mode feature previously visible in the paramagnetic phase. As shown in Fig. 3.5(e), the features defining the phase transition and the soft mode respond to longitudinal field in qualitatively different fashions. The transverse-field location of the phase transition only depends

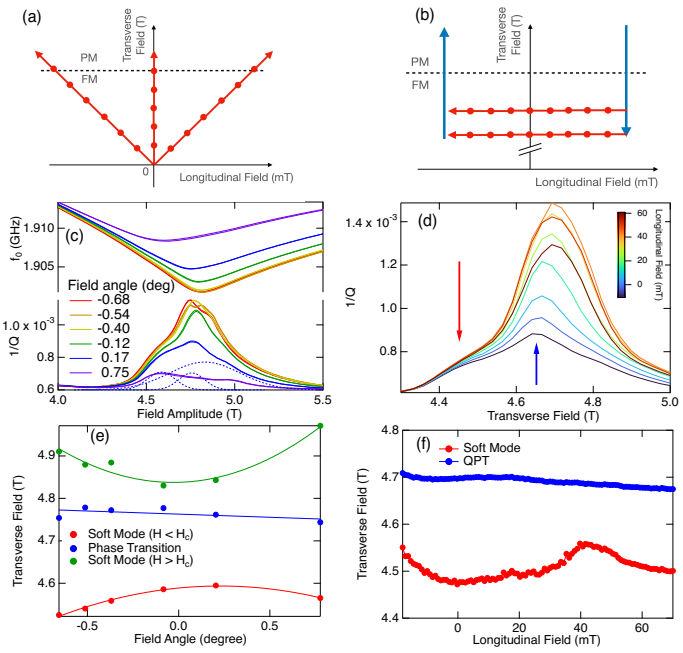

Figure 3.5: Effects of longitudinal dc field. (a) Fixed-angle protocol: fields along the transverse and longitudinal directions are ramped together ratiometrically. (b) Field-cool protocol: starting in the paramagnet, a longitudinal pinning field is applied, the transverse field is decreased to the measurement field, and data taken as a function of longitudinal field. (c) Response to the fixed-angle protocol. The center frequency (top) shows the shift in the quantum phase transition cusp as the field angle is changed. The absorption (1/Q) (bottom) of the low-energy mode absorption diminishes for larger field angles. Zero degrees denotes a field purely in the transverse direction with respect to the crystal. Dashed lines show the three fitted peaks for the 0.17 deg trace. (d) Response to the field-cooling protocol, showing a large peak in the dissipation at the quantum phase transition and a smaller satellite peak due to the low-energy mode crossing the 1.9 GHz measurement frequency. (e) Field-angle dependence of the low-energy mode for transverse fields above and below the quantum phase transition, along with the angle dependence of the phase transition itself. Curves are guides to the eye. (f) Loci of the phase transition and low-energy mode in (H_l, H_T) space. For both field protocols, the low-energy mode exhibits qualitatively different behavior than the phase transition, revealing the influence of a dc longitudinal field and the onset of history dependence due to ferromagnetic domain formation.

weakly on the longitudinal field. However, the presence of a longitudinal field does suppress the magnitude of the peak in the dissipation. By contrast, the location of the soft-mode dissipative peak moves significantly as a function of longitudinal field. It is asymmetric about zero, indicating that hysteresis due to ferromagnetic domains plays a significant role in setting the field scale for the mode.

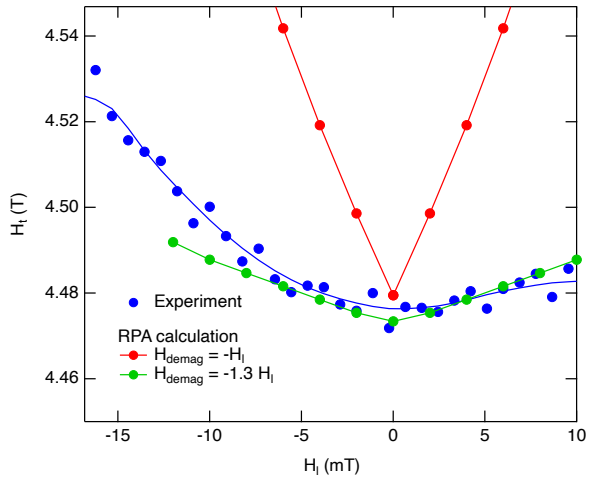

Figure 3.6: Location of the soft-mode peak for small H_z. RPA calculations are for mode locations for two different scalings of internal demagnetization fields. The two theoretical curves are plotted for (i) an internal demagnetization field equal and opposite to the applied field, and (ii) a demagnetization field 30% larger than the applied field, taking into account a finite domain wall energy.

Fig. 3.6 compares theory and experiment for the transverse field location of the soft mode minimum at 1.9 GHz. Two theoretical curves are shown. In the first, the average demagnetization field H_{dm} is assumed equal and opposite to H_z (appropriate to zero energy domain walls). This soft mode minimum has a sharper dependence on H_z than seen in experiment. In the second, a finite domain wall energy is assumed. This increases H_{dm} [KE60]. Micron-sized stripe domains in thin samples of $LiHoF_4$ indicate a domain wall energy $\sim 10^{-2}\ Jm^{-2}$ (which will vary with H_z, H_x, and T). The actual domain structure will be more complicated (e.g., branching in thick samples [Pom+88; GG85]), but still will increase H_{dm}. Assuming $H_{dm} \sim 1.3H_z$ (second theoretical curve) yields a good match to the data.

This protocol is repeated for a series of transverse fields H_x and the resultant mesh of absorptions $1/Q(H_x, H_z)$ is plotted in Fig. 3.6(a). We see strong absorption at a critical value of the transverse field for which the lowest energy excitation has a minimum (similar to critical opalescence). The softening is cut off by H_z, substantially suppressing the peak amplitude. Below the critical value H_c of H_x, we also see resonant absorption where the soft mode is degenerate with the cavity mode. The minimum in the soft mode is then lifted by H_z, suppressing its absorption, and reducing the cavity $1/Q$.

3.3 Discussion

The close agreement of theory with experiment indicates that weakly-coupled RPA electronuclear modes represent the true collective degrees of freedom unusually well. Special conditions are required to observe the soft mode: the net longitudinal field B_z in the sample must be homogeneous and zero; we need to measure χ^{zz}; and we need to go to low ω, T. If the RPA is correct, disorder will scatter all the electronuclear modes, and any net B_z will gap the soft mode.

We now can identify the gapped mode seen in previous neutron scattering experiments on $LiHoF_4$ [Røn+05] as the single electronuclear state that splits off from the upper group of modes shown in Fig. 3.1. RPA calculations correctly predict the measured energy of this mode as a function of H_x, and also predict it to be the only mode with significant spectral weight at these energies.

There are many systems in which quantum Ising spins couple to both static and dynamic “defect" modes (spin impurities, two-level systems, nuclear spins, etc.). One example of current interest is in quantum computation. In adiabatic quantum computation the system moves slowly through a QCP [AL18] such that two-level systems (TLS) are predicted to strongly affect the behavior [WAW09]. Our results, taken together with previous results on molecular magnet crystals, suggest the following general picture:

(i) When the coupling to these defect modes is weak (as for nuclear spins in transition metal-based molecular magnetic systems like Fe_8, Mn_{12}, V_{15}, etc.), for nuclear spins acting on spin qubits in semiconductors [YML16], or TLS defects weakly coupled to superconductors [Coo+04]), then hybridization will be disrupted unless one can go to extremely low T. Experiments will then see quantum relaxation of the Ising spins, and no coherent collective modes. To suppress strong decoherence in the Ising spin (qubit) dynamics one must then raise the characteristic qubit operating frequency of these qubits (using, for example, a strong magnetic field [Tak+11]).

(ii) When the coupling is strong (as for nuclear spins in $LiHoF_4$ and other rare earth systems, or for some junction TLS defects in superconductors [Coo+04]), Ising spin/defect hybridization can occur. If the system is translationally invariant (as in $LiHoF_4$) we then expect coherent hybridized collective modes, one of which will go soft at the QCP. The defects no longer cause decoherence for the Ising spins (qubits), but instead act in concert with them.

Until now there has been no experimental evidence for these coherent modes around a

QPT[1]. It remains of considerable interest to investigate and experimentally manipulate them in a variety of magnetic quantum Ising systems. We see that field sweeps through a QPT in adiabatic quantum computing can no longer be regarded as a simple 2 level-avoidance process—one must consider all of the collective modes. Since many such materials are promising candidates for solid-state qubit realizations [Ber+07; Mor+13; Ped+16], these collective modes must be characterized fully.

[1]Note that propagating electronuclear modes of the Suhl-Nakamura type [cf. [Suh58]; [Nak58]] have been studied for many years in ordered magnetic systems. The key difference here comes from the QPT, where one of these modes softens and is extremely sensitive to any longitudinal field.

Chapter 4

Additional $LiHoF_4$ Measurements

4.1 Introduction

The preceding chapter mostly reflects measurements that were published [Lib+21a] focusing on the electronuclear soft mode. In this chapter we shall explore an assortment of other measurements of $LiHoF_4$ that bear on the fundamental behavior of the spectrum of electronuclear modes and higher lying crystal field states.

4.2 Thermal effects

Another factor to consider is the effect of temperature on the spectra and energy levels of $LiHoF_4$. The occupation probability of a level E_i is given as $p(E_i) = \exp -E_i/k_BT$, or in terms of frequency $p(f_i) = \exp -hf_i/k_BT = \exp a$. For one LGR configuration, I took field scans at several temperatures

In addition to the quantum phase transition seen when ramping magnetic field at a fixed temperature, we can also explore the classical phase transition by ramping temperature at fixed field. The Curie temperature T_c is quite difficult to predict with theory. Often, the exchange coupling parameter J_{ex} is tuned empirically to match experiment. Recent work has also predicted that the classical phase boundary might not decrease monotonically when the magnetic field is raised slightly above zero [DAS22].

In order to investigate this regime, we continuously scan temperature at zero magnetic field while monitoring S_{21}. This is shown in Fig. 4.1. A notable feature is that the absorption drops significantly as the temperature drops below 12 K. This temperature is much too high for any magnetic transition in $LiHoF_4$. However, we can return to Fig. 1.1, where we see that above the ground state doublet is an excited state comparable to this temperature scale. The temperature determines which manifold of

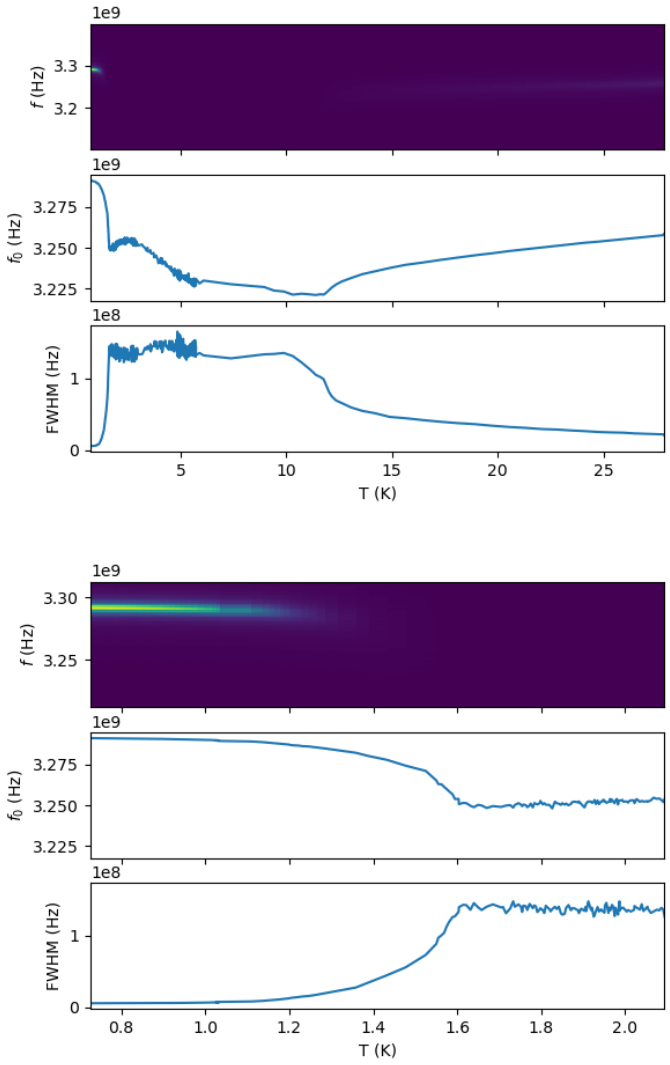

Figure 4.1: Zero-field spectra of $LiHoF_4$ through a wide temperature range. The absorption changes significantly at the phase transition near 1.6K as expected, but we can also see a change around 10-12 K which maps to the next crystal field state as shown in Fig. 1.1.

states is occupied, and the microwave photons can excite photons between hyperfine states within this manifold.

We examine in Fig. 4.2 the temperature dependence of the microwave absorption to further characterize the behavior of the higher-energy transitions. Due to the relatively weak intensity of the off-resonance response, the data in this figure is shown normalized by the $H_t = 0$ behavior. The two features dominant at low temperature—the cusp in the vicinity of the QPT and the avoided level crossing

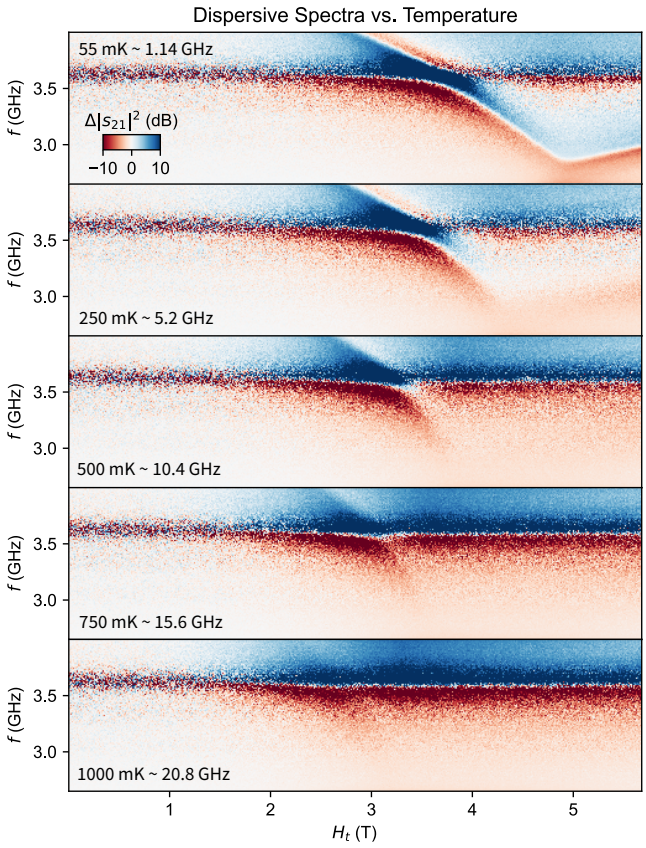

Figure 4.2: Dispersive temperature dependence of spectra in $LiHoF_4$. The transverse field scale decreases as expected with increased temperature due to the shape of the ferromagnetic to paramagnetic phase boundary. Coupling to the modes also weakens at high temperature, especially at low frequencies. Note the conversion 1 K $\sim$ 20.8 GHz, meaning that the population distribution at higher temperatures is such that the absorption is weakened.

where the electronuclear mode energy approaches the 3.6 GHz upper resonance of the LGR—both diminish in intensity and move to lower transverse field as the temperature is increased. The cusp associated with the paramagnetic transition is visible at 250 mK, but it is thermally washed out at higher T, while the avoided level crossing remains observable (albeit with lessened strength) to $T \sim 1$ K, reflecting a separation of energy scales between single ion and collective behavior.

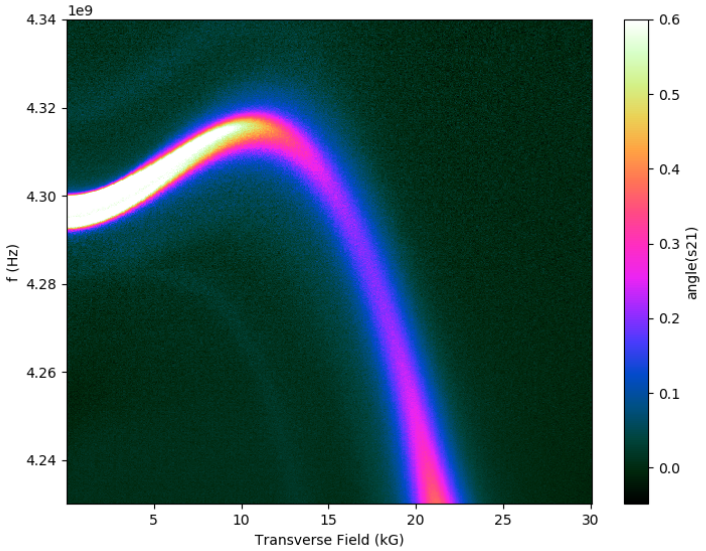

Figure 4.3: Low field dispersive spectrum of $LiHoF_4$ showing the behavior near zero-field. Notice the faint modes below the central hyperfine mode cluster. These are most likely associated with Walker modes.

4.3 Dispersive spectra

In some loop-gap resonator configurations, the field off-resonance is sensitive to the energy levels themselves away from the cavity resonance. This is most likely due to overcoupling to the resonator allowing for off-resonance transmission directly between the antenna pins. These data are very detailed and provide much insight into the system. In this section, I will discuss these results and what they can tell us about the linewidths, excited hyperfine states, and the Walker modes.

At low-field, we see that the hyperfine states are clustered together around 4.3 GHz. At zero field, it is apparent that we are seeing a cluster of transitions as expected in the calculation seen in Figure 3.4[1]. Beyond the main hyperfine modes, we also see a few weak modes in the background, shown in Fig. 4.3 in the phase of S_{21} with an adjusted color scale.

[1]The inset only shows the lowest energy transition at zero field; the clustering behavior is also shown in [Kov+16] Fig. 3b.

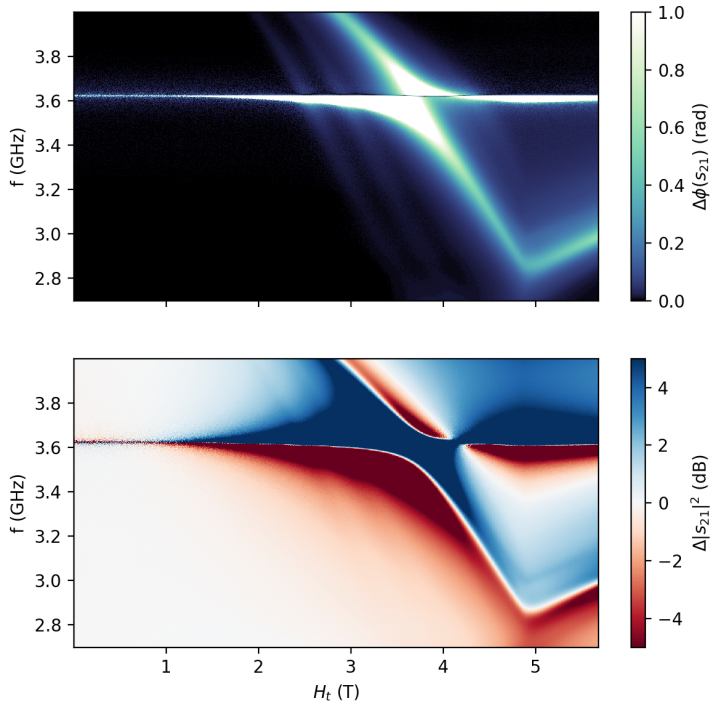

Figure 4.4: Detailed dispersive spectrum of $LiHoF_4$, away from the main resonator mode (with the anti-resonance at 3.6 GHz). The top spectrum displays S_{21} magnitude and the bottom phase, both with a low-field background subtracted. The two Walker modes are visible on the left, and above the central hyperfine mode we can see the higher order modes, visible as a blue line shaded in the phase plot.

4.4 Walker modes

In most of these spectra, we can see a distinct pair of modes that shadow the strong hyperfine mode cluster at lower frequency, seen clearly in Figure 4.4. They are visible on both sides of the phase transition in Figure 4.4, in both the ferromagnetic and paramagnetic states. Additionally, the low-field dispersive spectrum shown in Figure 4.4 has extra modes which seem to be connected to the others. There is one at higher frequency that at zero field starts above and then merges with the central mode. The two at lower frequency and field from the central mode appear to start at slightly lower frequency than the main mode. The one that is closer to the central mode is less distinct from it, but is visible as an asymmetric shoulder. There are no modes like this in the mean field or RPA calculations [MS18].

The first description of Walker modes was by their namesake L.R. Walker [Wal57], in

ferromagnetic resonance (FMR) in ferrites, where that satellite peaks were observed beside the central FMR mode. These arise from spatially inhomogeneous RF fields, which excite modes that vary in phase depending on the location in the material. The variation is on the scale of the sample dimensions, thus setting the smallest wavelength possible. Walker noted that this means for samples larger than micron-size (ours are mm-size) exchange forces are negligible. This theory is also developed under the condition that the material is small enough that these waves do not propagate, leading to size-independence between these two conditions. We can find the behavior of these modes by solving the equation of motion, which can be linearized under the assumption that the spins only make small deviations from the DC field. These solutions must satisfy the usual magnetostatic conditions, hence the other name [Blo67; de +63; TK66].

Walker modes are usually discussed in the context of spheroidal samples which have a uniform demagnetization field. In this case, Walker modes are excited by non-uniform RF fields. For practical reasons (see Chapter 2) we are using cuboidal samples, which have spatially inhomogeneous demagnetization fields [McK23]. The non-uniform demagnetization fields can also excite Walker-like modes.

In order to analyze the Walker modes, we can use the equation of motion (EOM) approach, which is also connected to a method used with RPA [McK23]. The basic equation determining the spin/magnetization dynamics is the Landau-Lifshitz equation:

$$\frac{d\mathbf{M}}{dt} = \gamma\mu_0 \left[\mathbf{M}(t) \times \mathbf{H}_{loc}(t)\right], \tag{4.1}$$

where $\mathbf{H}_{loc}$ is the local field; a sum of an applied field $\mathbf{H}_a$ and the dipolar field $\mathbf{H}_{\text{dip}}$.

In this material we have many interactions to account for. The transitions here are between nuclear states, but they are measured through the electron spins. Furthermore, the electronic spins can be ferromagnetically ordered. These magnetostatic modes are therefore the result of many interactions that must be accounted for to understand magnetic quantum phase transitions in an arbitrarily-shaped material [Chi+23; CJ73; Mak+24].

In order to gain qualitative insight into the magnetostatic modes in $LiHoF_4$, we can follow the work of Blocker for a ferromagnetic sphere [Blo67], which like our

$LiHoF_4$ is monoisotopic so 100% of the atoms have the same nuclear spin. Using an isotropic hyperfine interaction like $LiHoF_4$:

$$\mathcal{H}_{\text{hf}} = -\alpha \mathbf{m} \cdot \mathbf{M} \tag{4.2}$$

where $\mathbf{M}$ is the electronic magnetization and $\mathbf{m}$ is the nuclear spin. $\alpha = A/\hbar^2\gamma_e\gamma_N$ is ratio of the hyperfine coupling strength A to the electronic (γ_e) and nuclear (g_N) gyromagnetic ratios. We can find the Walker modes by solving the linearized Landau-Lifshitz equation:

$$\frac{\mathrm{d}\mathbf{M}}{\mathrm{d}t} = -\gamma_e \left(\mathbf{M} \times \mathbf{H}_e\right), \frac{\mathrm{d}\mathbf{m}}{\mathrm{d}t} = -\gamma_N \left(\mathbf{m} \times \mathbf{H}_N\right). \tag{4.3}$$

Blocker notes that the solutions for this equation can be written as:

$$4\pi M_x = \alpha h_x - j\beta h_y, \tag{4.4}$$
$$4\pi M_y = j\beta h_x + \alpha h_y, \tag{4.5}$$
$$4\pi m_x = \gamma h_x - j\delta h_y, \tag{4.6}$$
$$4\pi m_y = j\delta h_x + \gamma h_y. \tag{4.7}$$

The solutions must also satisfy the magnetostatic equations:

$$\nabla \times \mathbf{h} = 0, \tag{4.8}$$
$$\nabla \cdot [\mathbf{h} + 4\pi(\mathbf{M} + \mathbf{m})] = 0. \tag{4.9}$$

Equations 4.7 and 4.9 are the differential equations that define the Walker modes. The solutions are difficult for a cuboid shaped sample, but this should be practical with finite element software.

We look at the temperature dependence of the two types of modes to further separate out the domain dynamics manifesting as Walker modes from the soft mode and other excitations driven by the single-ion energy hierarchy of the sample. As shown in Fig. 4.5, the avoided level crossings associated with the Walker modes are clearly visible at 55 mK, but have essentially vanished by 500 mK. Conversely, transitions to the higher electronuclear modes persist to 1 K and above (Fig. 4.5).

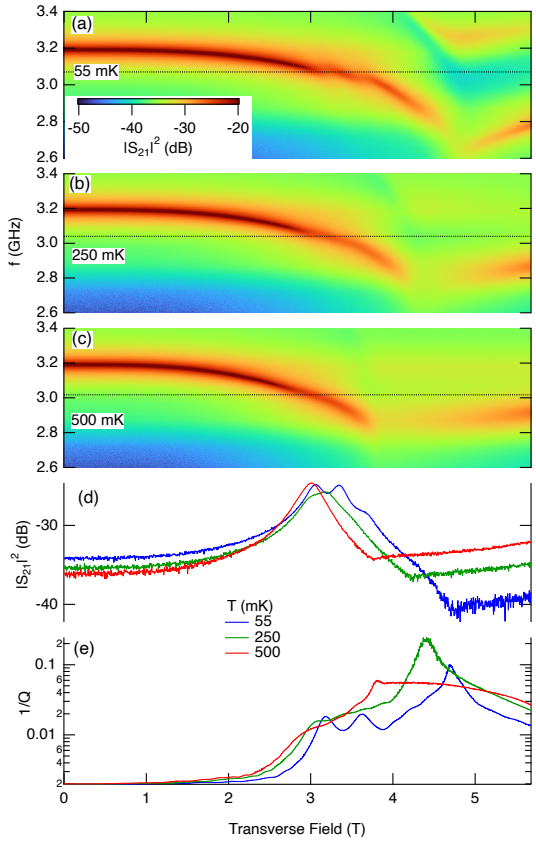

Figure 4.5: Temperature evolution of Walker modes, measured with a resonator tuned to 3.2 GHz at zero magnetic field. (a-c) As the temperature increases from 55 to 500 mK, the avoided level crossings characteristic of the Walker modes weaken and vanish, while the behavior driven by the electronuclear mode structure remains robust. (d) constant-frequency cuts (shown by the dashed lines in the upper three panels) exhibit the temperature evolution. The cuts evolve from a clear multi-peak structure to a single peak due to the net magnetization of the sample with no additional features. (e) $1/Q$ vs H_T for three temperatures, showing the thermal suppression of the Walker mode features.

4.5 Magnon-polaritons

> The theory discussed in this chapter was developed by Ryan McKenzie (Ames National Laboratory, previously University of British Columbia), published in [McK+22]. I am including the essential results and comparison to my data.

Having discussed the mean-field (MF) and random phase approximation (RPA) theories and the experimental data, we can look at the various models and determine what most accurately describes the system. We mentioned one of these earlier with

the circuit model. Another useful simple analogy is to that of coupled harmonic oscillators. We can start with a model of classical harmonic oscillators, which provide a useful and intuitive description with close correspondence to the full quantum system. The cavity, or loop-gap resonator, is oscillator #1, and the spin system is oscillator #2. The VNA probing signal is connected through a spring with a spring constant κ_1 to this oscillator, which corresponds to the coupling antenna. The spin-cavity coupling is representing by another spring with constant κ. For our VNA transmission measurement, the other coupling antenna is connected to the cavity oscillator through a similar spring κ_2 like the other antenna.

We can also analyze this system using the methods of quantum optics. This will allow use of the microscopic Hamiltonian and allow us to make connections to hybrid quantum systems [Flo+19].

The magnon-polariton propagator of the resonator photons ($x = a^\dagger + a$) is found to be

$$D_{mp}(z) = -\frac{2\omega_r}{\beta}\left[\frac{1}{z^2 - \omega_r^2 + \alpha^2 2\omega_r \chi(z)}\right]. \tag{4.10}$$

This propagator is a central result of the magnon-polariton theory. It provides a primary connection between theoretical work and the experimentally-measured resonator transmission function. It includes the effects of counter-rotating terms which become important in the ultra-strong, or deep strong, coupling regimes.

Assuming ohmic (frequency independent) damping of the magnon modes, the damped retarded magnon-polariton propagator may be written ($D^{ret}_{mp}(\omega) = \beta D_{mp}(z \rightarrow \omega + i0^+)$)

$$D^{ret}_{mp}(\omega) = \frac{-2\omega_r}{\omega^2 - \omega^2_{mp} + i\omega\Gamma_{mp}}, \tag{4.11}$$

where from equation (4.10)

$$\omega^2_{mp} = \omega_r^2 + (\Gamma_r/2)^2 - 2\alpha^2\omega_r\chi'(\omega), \tag{4.12}$$

and

$$\omega\Gamma_{mp} = \omega\Gamma_r + 2\alpha^2\omega_r\chi''(\omega). \tag{4.13}$$

A factor of Γ_r has been included to account for any intrinsic damping of the resonator mode.

It follows from equation (4.11) that

$$|S_{21}|^2 \propto \mathrm{Im}[D^{ret}_{mp}] = \frac{2\omega\omega_r\Gamma_{mp}}{(\omega^2 - \omega^2_{mp})^2 + (\omega\Gamma_{mp})^2}. \tag{4.14}$$

Without knowledge of the proportionality constant, one cannot obtain Γ_{mp} from the amplitude and phase of the transmission function; however, one may still obtain the magnon-polariton modes, and compare qualitative features of their linewidths with theoretical results.

In Fig. 4.6, we consider resonator frequencies of $\omega_r/(2\pi) = 3.2\ GHz$ and 3.7 GHz, and compare the calculated transmission function to experimental data for a bimodal loop gap resonator. At these frequencies, the resonator modes are degenerate with the lowest single ion excitation in the system. We see strong avoided level crossings when the lowest single ion excitation is degenerate with the resonator modes. The increased spectral weight of the single ion excitation at 3.2 GHz leads to a stronger avoided level crossing than at 3.7 GHz, despite the reduction in frequency. This is consistent with the avoided level crossings seen in the experimental data.

The experimental data is for a bimodal resonator. In the theoretical calculation we assume the two resonator modes are independent and sum their response. This fails to capture interactions between the resonator modes, which lead to the antiresonance seen in the experimental data near 3.6 GHz, and mixing of the calculated polariton modes. Nevertheless, we find good agreement between the calculated resonator transmission and the experimental data. The lowest polariton mode exhibits a series of weak avoided level crossings in the ferromagnetic phase of the quantum Ising material. These avoided level crossings are due to the soft mode, and Walker modes present in the material (as discussed in Section 5.4).

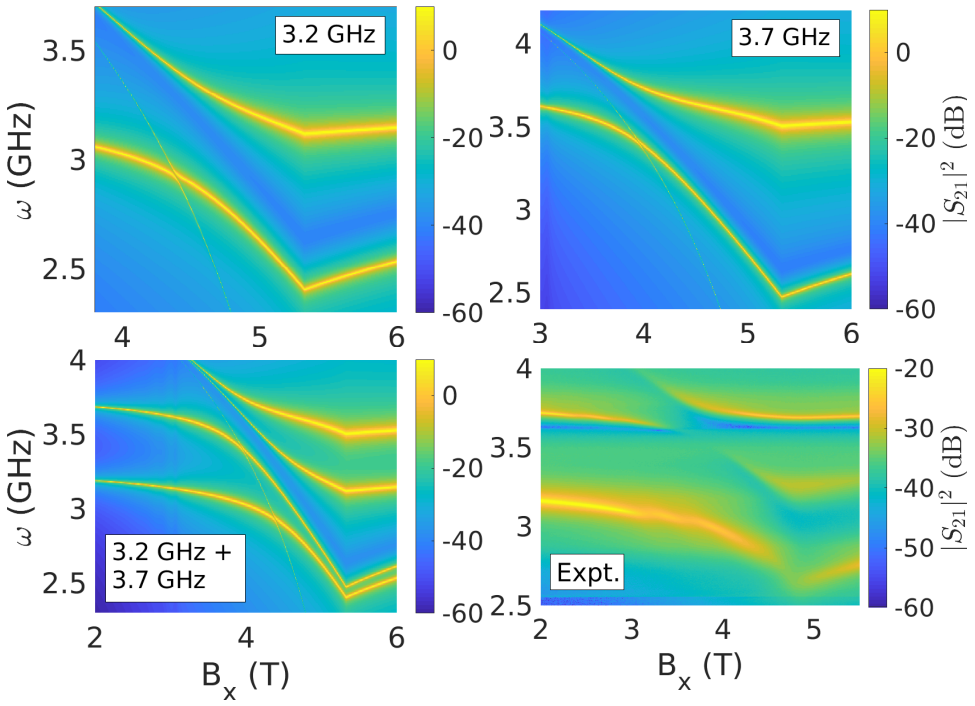

Figure 4.6: Mixed single ion and collective mode transmission of $LiHoF_4$ in a 3.2 GHz and 3.7 GHz resonator at zero temperature. The filling factor is set to $\eta = 0.25$, and the damping parameters are chosen to be in line with what one expects for spin vacancies in diamond. The decoherence factor is set to $\gamma_{dec} = 100\,\text{GHz}$, a value for which, although faint, the soft mode is visible in the transmission spectrum. Comparing the avoided level crossing in the 3.2 GHz resonator to the 3.7 GHz resonator in the upper pair of figures, we see a larger avoided level crossing at the lower frequency. This is due to the increase of the spectral weight of the magnon mode at 3.2 GHz, which supersedes the reduction in coupling strength due to the lower resonator frequency. In the lower pair of figures, we sum the calculated transmission from the 3.2 GHz and the 3.7 GHz resonators, and compare the results to transmission through a bimodal loop gap resonator. In the experimental data, interactions between the resonator modes lead to an antiresonance near 3.6 GHz and hybridization of the polariton modes not accounted for in the theoretical calculation. The lowest polariton mode in the experimental data exhibits weak avoided level crossings consistent with the presence of the collective soft mode, and Walker modes, in the material (see text for details).

Chapter 5

Microwave Measurements in the Dipolar Antiferromagnet $LiErF_4$

5.1 Introduction

The $LiYF_4$ (or YLF) system presents a unique opportunity to study several examples of quantum magnetism. As discussed in Chapter 1, the various rare earth elements are similar chemically which allows the yttrium to be substituted during crystal growth with little structural variation. Here, we will examine $LiErF_4$, where each rare earth site is occupied by erbium.

Erbium ($_{68}$Er) has one more proton than holmium ($_{67}$Ho), and it has six stable isotopes [RBD24]. Of these, only $^{167}_{68}$Ho (23% abundance) has a non-zero nuclear spin ($I = 7/2+$). Hund's rules give the ground state of an Er^{3+} ion as the $4f^{11}$ shell with $S = 3/2, L = 6, J = L + S = 15/2$, which can be written as $^4I_{15/2}$ [Bab+15].

Another notable difference with erbium is that it is a Kramers ion because it has an even atomic number. Along with the other lanthanide elements with even atomic numbers, this means that the Er^{3+} ion has a doubly degenerate ground state, with half-integer spin [Pro16; AB12]. This degeneracy can be split by a magnetic field, breaking time reversal symmetry, which defines an electron paramagnetic resonance (EPR) mode at fairly low field and frequency. The Kramers ions have many other useful properties, such as very long relaxation times and sharp resonances [AB12]. Erbium in particular has seen further recent interest in microwave-to-optical conversion because it has an optical transition in standard telecommunication bands [Pro16].

To analyze this system we can start with the same general Hamiltonian discussed for $LiHoF_4$ (Eq. 1.3):

Citation	B_2^0	$10^3 B_4^0$	$10^3 B_4^4$	$10^5 B_6^0$	$10^5 B_6^4(c)$	$10^5 B_6^4(s)$
[HJN75]	0.0678	-0.678	-6.83	-0.0080	-13.3	± 1.69
[Bab+15]	0.0581	-0.536	-5.53	-0.000625	-10.6	± 2.38

Table 5.1: Crystal field parameters (i.e., coefficients for the Stevens operators) in meV for $LiErF_4$, given by the respective citations (collected by [Bab+15]). In [HJN75], they measured these with susceptibility, and for the latter they used neutron scattering. Note that I am using the same powers of ten I used for the $LiHoF_4$ Table 1.1 (consistent with [Røn+07]); Babkevich uses slightly different powers of ten in the prefactors. Compared to the $LiHoF_4$ values, many of these parameters for $LiErF_4$ have opposite signs. These factors explain the different magnetic ordering; Ising ferromagnet for $LiHoF_4$, and bilayer XY antiferromagnetism in $LiErF_4$.

$$\begin{aligned}\mathcal{H} = &\sum_i V_C\left(\vec{J}_i\right) - g_L\mu_B\sum_i B_x J_i^x + \frac{1}{2}\left(g_L\mu_B\right)^2\sum_{i\neq j}\mathcal{L}_{ij}^{\mu\nu}J_i^\mu J_j^\nu \\ &+ \frac{1}{2}\left(g_L\mu_B\right)^2\frac{J_{ex}}{a^3}\sum_{i,nn}\vec{J}_i\cdot\vec{J}_{NN} + A\sum_i\left(\vec{I}_i\cdot\vec{J}_i\right).\end{aligned} \tag{5.1}$$

As before, the first term with V_c represents the crystal electric field, which depends on the relative positions of neighboring ions. The relevant Stevens operators $O_l^m(\mathbf{J}_i)$ determined by symmetry are the same as in $LiHoF_4$, but the coefficients differ due to the different 4f electron configuration. These values are shown in Table 5.1.

The dipole coupling takes the same form:

$$\mathcal{L}_{ij}^{\mu\nu} = \frac{\delta^{\mu\nu}|\vec{r}_{ij}|^2 - 3(\vec{r}_{ij})^\mu(\vec{r}_{ij})^\nu}{|\vec{r}_{ij}|^5}. \tag{5.2}$$

These slightly different parameters give a significant difference in the magnetic ordering of $LiErF_4$. The crystal field leads to antiferromagnetic ordering. Whereas $LiHoF_4$ has ferromagnetic ordering with spins aligned to the Ising axis, in $LiErF_4$ the spins are aligned within a bilayer, which are antiferromagnetically coupled to each other. Two stacked layers have spins pointing in one direction in plane (→), and two layers stacked on top have the opposite spin in plane (←) [Kra+12]. Within the plane, the spins are oriented along either the crystalline a or b axes, giving an XY/4 symmetry.

Here, we are interested in the microwave spectra of $LiErF_4$ and how it relates to its antiferromagnetic ordering. The most relevant and detailed treatment of $LiErF_4$ in the

literature can be found in the work of C. Kraemer, with an overview in Kraemer et al. [Kra+12] and more detail in his thesis [Kra09]. These papers are mostly concerned with neutron scattering, but have some relevance here for microwave measurements. As discussed previously, microwave measurements with an LGR can overcome limitations for neutron scattering experiments. The neutron flux can significantly increase the sample temperature, making measurements below $T \sim 200\,\mathrm{mK}$ difficult. Additionally, because erbium has a number of stable isotopes, neutron activation could affect the sample by changing the isotopic composition, thus changing the effect of hyperfine coupling to nuclear spins. There have been susceptibility experiments using isotopically pure Li $^{168}ErF_4$, eliminating the hyperfine term [Gha12]. The effect was most pronounced at 35 mK, where the pure ^{168}Er sample had a lower H_c. This became less and less prominent at higher temperatures, until the two samples behaved the same around 260 mK. Measuring with an LGR also allows us to access a much lower energy scale. For comparison, 1 GHz = 4 meV.

5.2 Data

The techniques for measurements with $LiErF_4$ were similar to those of $LiHoF_4$. A single crystal sample of $LiErF_4$ was mounted in an LGR in the dilution refrigerator (Kelvinox MX250), using the solenoid transverse field magnet along with the split coil from section 2.2.

As with $LiHoF_4$, we can measure the dynamic susceptibility through the resonator properties. Away from crossings with specific energy levels, the change in resonant frequency δf_0 corresponds to the real part χ' and the change in inverse quality factor $\delta(1/Q)$ corresponds to the imaginary part χ''. The overall features and shape of the dynamic susceptibility are fairly similar to the low-frequency/static susceptibility, allowing for comparison to other experiments. The neutron scattering intensity also has a similar qualitative connection to the susceptibility, allowing some comparisons [Kra09].

We start by examining the zero-field temperature dependence, as shown in Fig. 5.1. We see the antiiferromagnetic phase transition around 360 mK as expected from Ref. [Kra+12]. The resonance is fairly broad above T_N and sharpens below, denoting a decrease in dissipation.

The LGR also allows us to directly measure the hyperfine mode. This is seen in the avoided level crossing in Fig. 5.2 at low temperatures. Around 0.03 T and 3.04 GHz we see where the hyperfine mode intersects the resonator frequency.

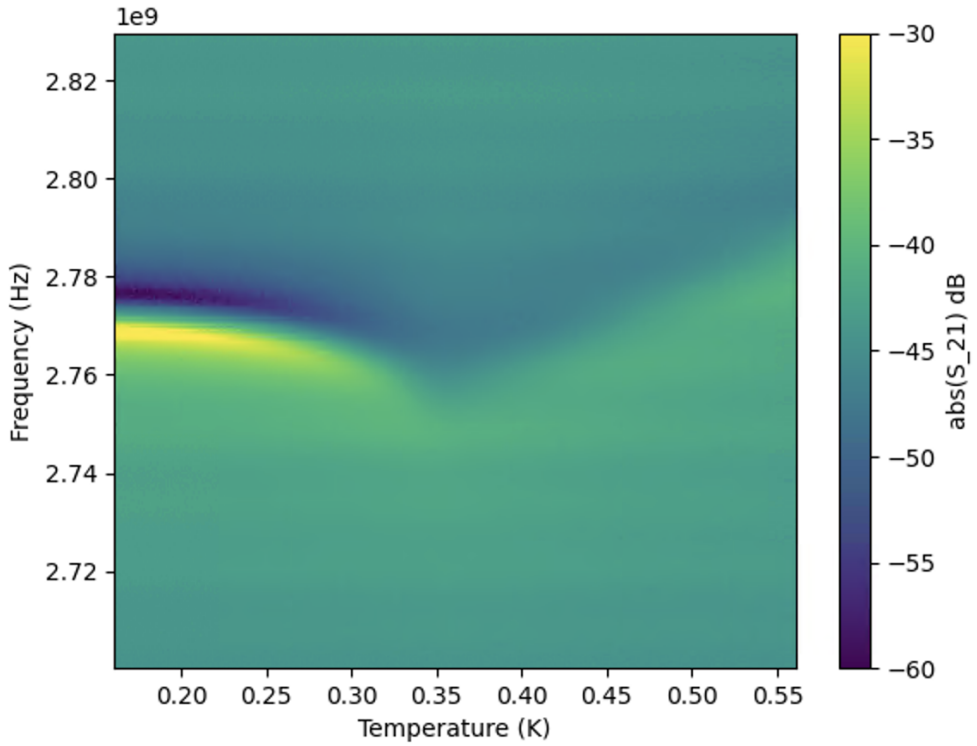

Figure 5.1: LGR measurement of $LiErF_4$ at zero field while cooling from 600 to 150 mK.

A key result is that the susceptibility sharpens as the temperature decreases from $\sim 360\,\text{mK}$ to $\sim 100\,\text{mK}$. Below this, we see that the susceptibility behavior at the quantum phase transition (QPT) actually becomes broader. This can be seen more quantitatively in Fig. 5.3, which fits the individual microwave spectra to a simple circuit model to obtain the real component of the magnetic susceptibility. This is counterintuitive, as we generally expect continuous sharpening as thermal fluctuations decrease. I tested to make sure it is not the result of hysteresis, magnetic field ramp rate, or microwave power. All of these spurious causes were ruled out. Other people in the research group have continued this work using low-frequency susceptibility, which reproduced this result, combined with heat capacity to directly measure the electronuclear energy scales. The fundamental similarity between the low and high frequency measurements shows that this behavior is an intrinsic effect. Instead, a more detailed analysis conducted by other members of the group demonstrated that it arises from isotopic disorder of erbium, leading to random moment disorder once the temperature cools below 150 mK and the hyperfine coupling becomes relevant.

Returning to the work of Kraemer et al., they do not see this effect in neutron scattering

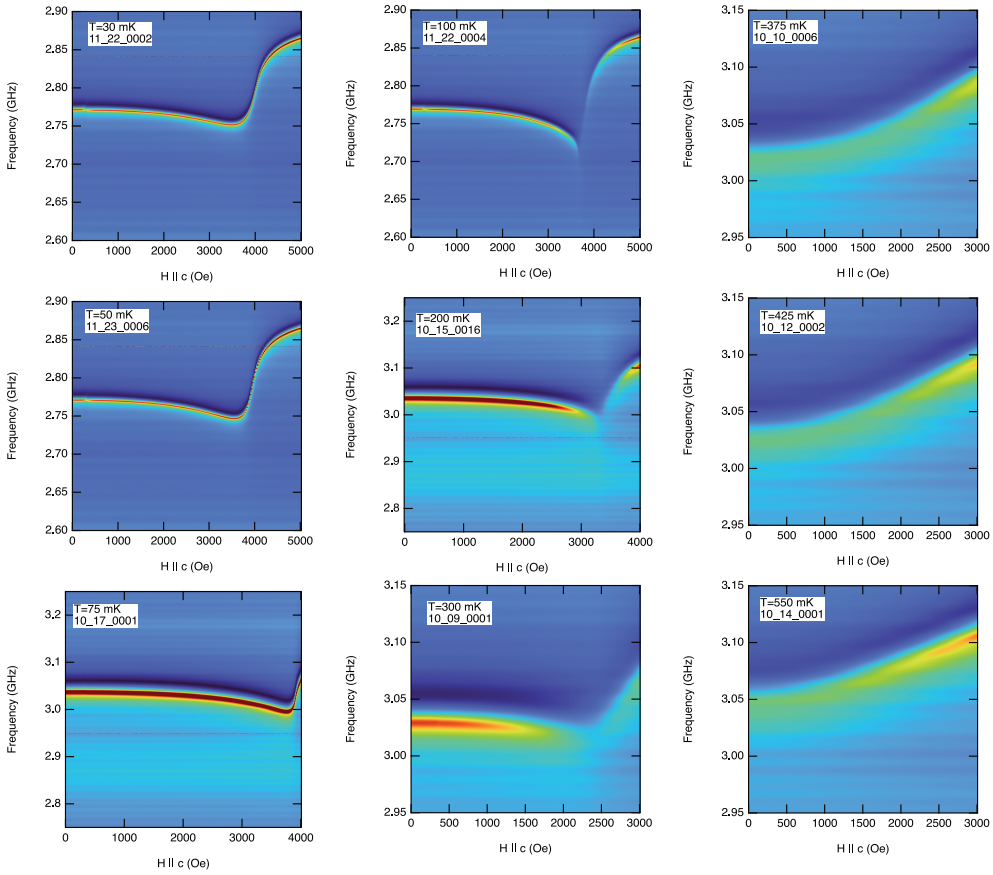

Figure 5.2: LGR measurement of $LiErF_4$ at various temperatures, ramping the magnetic field along the c-axis. At low temperatures, notice the hyperfine level crossing around 0.02 T. The linewidth (corresponding to the imaginary part of the susceptibility χ'') is mostly constant throughout the range at the lowest temperatures. Around 100 mK there is a sharp cusp and dramatic change in loss near 3700 Oe.

measurements [Kra+12]. Their measured intensity diagrams mostly level out below 150 mK, so heating from the neutrons most likely prevented them from reaching sufficiently low temperatures to see this effect. Further microwave measurements should be made with isotopically-pure $LiErF_4$to see what effect it has on the low-field level crossing and the susceptibility behavior.

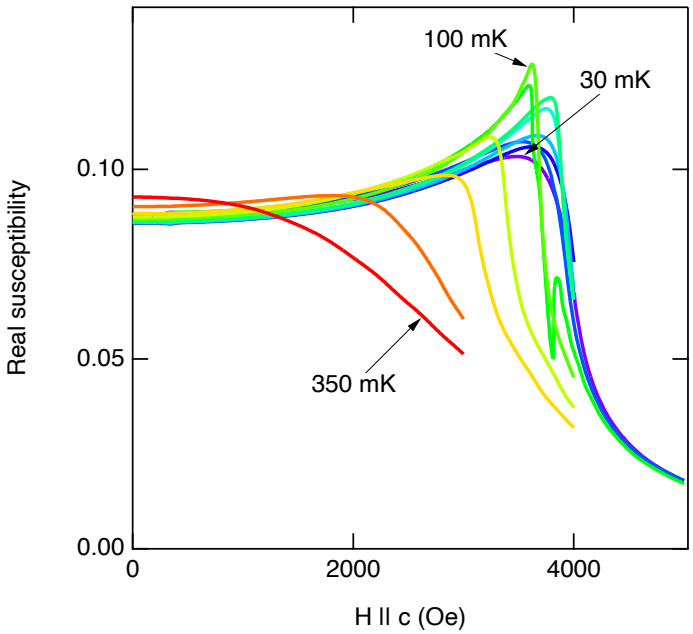

Figure 5.3: Susceptibility of $LiErF_4$ as a function of magnetic field along c at a series of temperatures. These curves are derived from the spectra shown in Fig. 5.2.

Chapter 6

Superconducting Microwave Resonators

6.1 Introduction

Superconducting resonators have many useful properties that have led to a range of applications and study through the years. These range from particle accelerators, sensitive radiation detectors (MKIDs) [Day+03], narrowband filters, and more recently qubits in quantum information science [For10; Pre+21]. Particle accelerators typically use 3-dimensional cavities, but the others use superconducting coplanar waveguide (CPW) resonators which we will focus on in this chapter. Although these are usually made with aluminum, our goal is investigate the use of niobium (and tantalum, which is very similar) to improve the quality of these resonators.

In this chapter we will focus on techniques for making higher-quality superconducting resonators with niobium and tantalum, and then look at how they might be interfaced with rare earth ion crystals for magnetic resonance and hybrid quantum systems.

6.2 Theory

Material

In this section we are primarily looking at elemental niobium films grown on sapphire. Later in this chapter we discuss using tantalum, which is just below niobium in the periodic table's group 5. Niobium is a metallic type II superconductor with a transition temperature of $T_c = 9.2\,\mathrm{K}$ in bulk [RBD24], though T_c decreases in thin films. This is the highest T_c for an elemental superconductor. The type II designation indicates that in a magnetic field, it allows penetration of flux vortices which allows the superconductivity to persist at higher fields than type I superconductors, which completely exclude magnetic flux but break down at smaller fields.

These factors make niobium a common, workhorse superconductor. Most practical applications use an alloy of niobium and titanium (NbTi), which can handle higher

temperatures and fields than the pure metal [RBD24]. This is what I used to build the split coil magnet in section 2.2. Niobium-titanium actually sees more use than higher-temperature and/or -field capable materials, because NbTi has excellent mechanical properties that are important for using it as a practical wire. The wire for the split coil was no more difficult to handle than a copper wire.

In this case, we are concerned with thin films of elemental niobium. While the most commonly used superconducting circuits and qubits are made with aluminum, niobium has some advantages [Pre+21]. Of course, niobium has a much higher $T_c = 9.2\,\mathrm{K}$ compared to aluminum's $T_c = 1.175\,\mathrm{K}$. It is also far more resilient to magnetic fields as a type II superconductor, with $B_0 = 206\,\mathrm{mT}$ for Nb compared to $B_0 = 10.49\,\mathrm{mT}$ for Al [RBD24].

Another important characteristic is that niobium forms many different oxides. This will relevant later when discussing loss sources. The most common of these is niobium pentoxide (Nb_2O_5) [NMG16]. For Josephson junctions (i.e., for qubits) it is most common to use aluminum oxide as the barrier. For niobium junctions, it is possible to use either Nb or Al oxide [THK89].

Molecular-beam epitaxy

The most significant method that we are using to improve the quality of superconducting films and resonators is by using molecular-beam epitaxy (MBE). In most cases, people make these films using techniques like sputtering and electron-beam evaporation. While these techniques are fast and widely available, they have some drawbacks. In sputtering for example, these include substrate interface damage from ions, and issues with contamination [Jia+23]. MBE also introduces several capabilities that these other techniques do not. For example, MBE allows control of growth on the layer-by-layer scale, with in-situ monitoring [AH19]. It also allows for the growth of films made up of elements from multiple sources. These capabilities are very important to improving superconducting resonators, as many of the loss sources are due to interfaces and contamination. Growing niobium films with MBE has been explored before (e.g., [ZF99]), but there are many opportunities to improve the processes and minimize loss.

Fundamentally, an MBE system source consists of an ultra-high vacuum (UHV) environment which houses a holder for the substrate, a mechanism to heat the substrate, and several material sources. Heating the substrate can improve the surface quality and crystallinity due to thermodynamic and kinetic effects [HS89]. The

design of the sources depends on which element is being used. For materials that evaporate at relatively low temperature, Knudsen cells are used. Also known as effusion cells, Knudsen cells use a filament to heat the source material so it evaporates. A shutter system controls the vapor flux [AH19]. For refractory metals, like niobium in our case, Knudsen cells would melt before the source. Therefore, when working with niobium, we use an electron beam to evaporate the Nb source.

A key characteristic of MBE is that the deposition rate is fairly slow. This allows more control of the growth, such as crystalline layers. It is possible to monitor this growth using reflection high-energy electron diffraction (RHEED) [AH19]. Growing slowly also has the consequence that contamination is more likely to be incorporated in the film. This is why a very clean UHV environment is required, often with a mass spectrometer to monitor the chamber.

Loss

Superconductors are well known for the absence of resistance to DC current. It is thus counter-intuitive that they are subject to other sources of loss at RF frequencies. These sources can be categorized by several properties, such as the location in the circuit (usually in bulk or an interface). This means that different designs of resonators can change the contribution of loss sources, as well as the fabrication process determining the quality of these areas. They can also have very different dependence on measurement parameters, particularly incident power (also corresponding to photon number and AC current), the temperature, a DC magnetic field, or a DC current.

One significant source of dissipation is two-level systems. The behavior has been known for a long time, first in amorphous materials [MCL19; HA76]. Even when using a metal film on a crystalline substrate, they are still prolific, such as on passivated surfaces [Zmu12; Phi87; Nie+20]. The microscopic origin of TLS is not well understood. TLS typically occur when the potential energy associated with an atom's position in a disordered system has minima can be tunneled between. The energies involved are usually quite low, so they only become important at very low temperatures.

One of our main goals is to reduce loss in these resonators, and TLS is dominant at low temperature and when approaching the single-photon limit. Our goal is to improve the material quality in order to reduce the number of defects correlated with TLS. Usually, other experiments grow the superconducting films using techniques

like sputtering or electron-beam evaporation, which form an amorphous film with a fair amount of defects creating TLS, especially at material interfaces. Another benefit of MBE is that when a substrate with similar lattice constant is used, the epitaxial layers can form a well-aligned interface. This should provide a benefit because TLS are known to be relevant at interfaces.

Additionally, polycrystalline films have TLS loss localized to the grain boundaries [Pre+21]. A key quality of MBE is that we can grow crystals layer by layer, we should be able to significantly reduce the contribution of TLS loss at grain boundaries.

Nonlinearity

A useful property of superconducting resonators is the nonlinearity [Tho+20] which can be driven by incident radiation, temperature, or AC current level. This leads to many applications such as detectors, temperature measurements, and amplifiers [KS23; YB06]. We can look at how our resonators respond different power levels (corresponding to current levels) to learn more about the film quality and suitability for such applications.

6.3 Design

For the initial experiments, we are using a design with an array of $\lambda/4$ resonators with a section of transmission line close to the central line. These are considered hanger resonators, and are usually measured in transmission (S_{21}). When an incident signal frequency is off resonance with all of the resonators, the signal is passed through with minimal loss as the hangers reflect most of any coupled energy back to the main transmission line. When the signal is on resonance with a resonator it will absorb some energy away from the main transmission line. Therefore, the S_{21} trace of such a device is normally close to 1 (less normal cable/transmission loss), with sharp notches, i.e., decreases in transmission, when on resonance with any of these resonators. Notably with these superconducting resonators, the quality factors are on the order of $Q \sim 10^5 - 10^6$ or higher. This means that they are easy to miss if the frequency resolution of the VNA is not fine enough to see the notches.

There are multiple ways to conceptualize an electromagnetic resonator. We discussed loop-gap resonators (LGRs) previously, as a three-dimensional resonator which to some extent can be thought of as a lumped-element (LE) resonator with spatially distict inductance and capacitance (and thus electric and magnetic fields). LGRs and

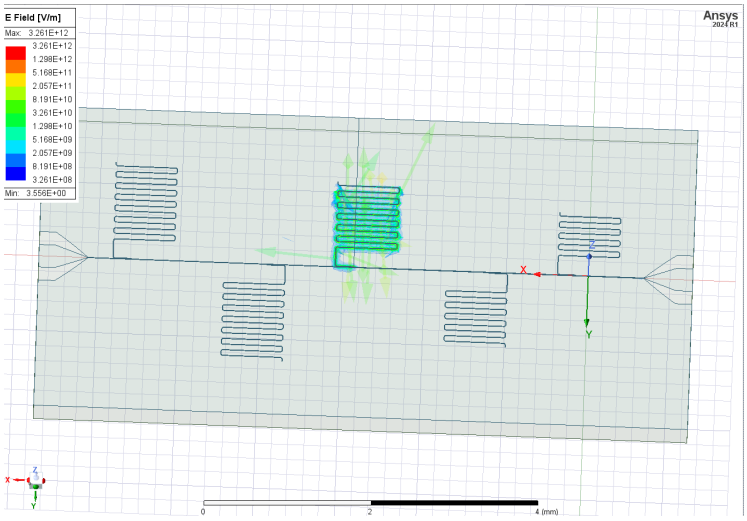

Figure 6.1: HFSS simulation of the primary resonator design discussed here, developed by JPL collaborators. The electric field is plotted with the middle resonator in resonance. The electric field is concentrated in plane across the gaps.

cavity resonators are the main types of 3D resonators, but we can also consider 2D resonators. It is possible to make a 2D LE resonator with capacitive and inductive structures separated in analogy to LGRs, but here we will consider an analogy to 3D cavities in 2D transmission line resonators.

When electromagnetic waves encounter an electrically conductive material the magnitude decreases exponentially with the depth in the material. The field magnitude is proportional to $\exp(-\gamma z)$ where z is the position inside the conductor, and γ is the propagation constant [Poz11]:

$$\gamma = \alpha + j\beta \approx j\omega\sqrt{\mu\epsilon}\sqrt{\frac{\sigma}{j\omega\epsilon}} = (1+j)\sqrt{\frac{\omega\mu\sigma}{2}}. \tag{6.1}$$

This is complex in general, with a phase constant β and an attenuation constant α. It is useful to define a skin depth where the fields have decayed by $1/e = 36.8\%$. This depth is given by

$$\delta_s = \frac{1}{\alpha} = \sqrt{\frac{2}{\omega\mu\sigma}}. \tag{6.2}$$

For a typical good conductor (gold, silver, copper, ...) this is on the order of 1 µm.

6.4 Microfabrication

Substrate

As discussed previously, a key factor in growing epitaxial films is the compatibility between the lattices of the substrate and film. In order to minimize defects, the crystal lattices should be able to fit together neatly. For niobium, it turns out that crystals of sapphire (crystalline Al_2O_3) are remarkably well-matched to niobium [WMT01]. Additionally, as discussed in the context of LGR tuning, sapphire has excellent properties at microwave frequencies. This means that niobium on sapphire is an excellent combination for high-quality microwave CPW resonators [WGP03].

To grow these superconducting films, we start with a sapphire substrate. This is mainly chosen because its lattice constant is comparable to that of the niobium that will grow on top. Niobium forms crystals with a body-centered cubic (BCC) structure, with a lattice constant of 0.3307 nm. Sapphire (Al_2O_3) is a hexagonal close packed (HCP) structure with $a = 0.4759$ nm and 1.2991 nm [Du+16]. The lattice mismatch between these two is given by

$$\delta_1 = 2\frac{d_f - d_s}{d_f + d_s} \tag{6.3}$$

where d_f is the plane spacing of the Nb film lattice, and d_s is the substrate plane spacing [Du+16; BSW02]. The following crystal alignments are well-matched. We have used the first one:

$$\mathrm{Al_2O_3}[1\,1\,\bar{2}\,0] \parallel \mathrm{Nb}[1\,1\,0] \tag{6.4}$$

$$\mathrm{Al_2O_3}[0\,0\,0\,1] \parallel \mathrm{Nb}[\bar{1}\,1\,1] \tag{6.5}$$

$$\mathrm{Al_2O_3}[1\,\bar{1}\,0\,0] \parallel \mathrm{Nb}[\bar{1}\,1\,2]. \tag{6.6}$$

The films were grown by Sandra Glotzer with MBE, taking care to clean the surface before deposition. Due to how the substrates are held by the corners, metal film is missing in small notches at the corners, which had to be accounted for in the design.

I made an assortment of chip patterns that were ordered on a mask, shown in Fig. 6.2. However, the measured data shown here are using a design made by collaborators at JPL, shown in Fig. 6.1.

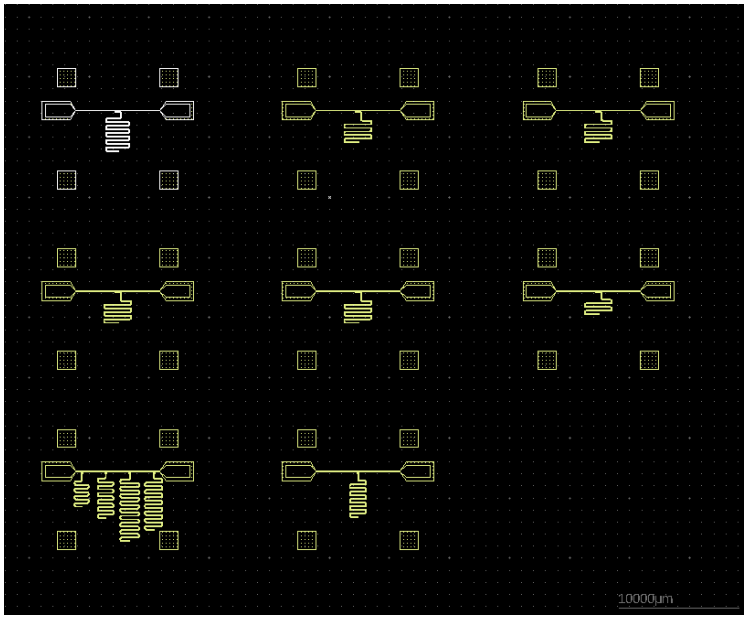

Figure 6.2: Original layout with various CPW resonators that I used to ordered a mask. Each small square is a chip pattern that can be used, with varying parameters including coupling method and length.

Wet processing

The first process we attempted was using wet chemicals for the steps. First, I ordered a mask with an array of many resonator variations, with the layout pictured in Figure 6.2. This mask consists of a glass substrate with the pattern in chrome. This is a negative mask, so the mask has metal where the end product will not have metal. The samples with Nb film are usually 10x10 mm. The following is an overview of the process. We prebake the sample and then spin-coat the sample with the PKP-308PI (Purified Kodak Photoresist) photoresist. After another bake, we use an MJB3 mask aligner to align, contact, and expose the chip. After this, we develop the chip in the specified developer for PKP. At this point we have hardened/insoluble photoresist covering the parts that should end up with metal.

We then etch the niobium film in a solution of 10% hydrofluoric acid (HF), which is the only known effective wet etchant for niobium. The need to use HF is what necessitated the PKP resist, as it is said to be resistant to HF. However, our attempts with wet processing had issues with adhesion, nonuniform photoresist application, and unknown sources of contamination. The likely issue is poor adhesion of the photoresist which then could make it more prone to degradation by HF. This resulted

in rough edges seen in Figure 6.3.

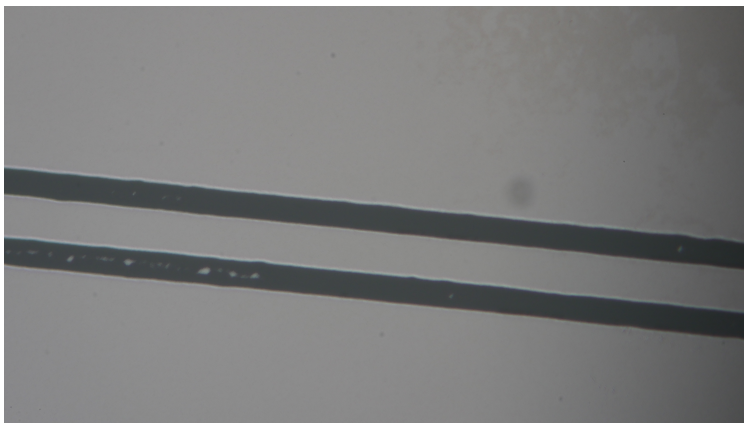

Figure 6.3: Microscope photograph of a niobium CPW made using the wet process with HF described in the text. The edges became rough, likely due to HF attacking the photoresist and over-etching.

Dry processing

Rather than trying further wet processing methods, we had an opportunity to manufacture resonators using a dry process at the Jet Propulsion Laboratory (JPL). This process is similar to the wet process, but using a dry etching process instead of HF. This process is similar to the wet process, but with some critical differences. The sample is coated with an anti-reflective layer (BARC) and Oir620 photoresist. This is a positive photoresist, meaning the pattern must be inverted. The combination of these chemicals worked well, with better adhesion.

For this process we could use the same mask aligner with a positive mask. However, these were done in the JPL cleanroom which has a Heidelberg laser writer which exposes the pattern directly on to the resist instead of with a mask. The laser writer itself accomplishes the same result that we could get with a photomask and aligner, but eliminates the step of ordering a mask. Instead it takes a layout file and exposes it like a laser printer for paper. This is very useful for making and changing prototypes.

After developing and exposing the chip, the other step that changed by using the JPL cleanroom is that a dry etch process is available. This allows us to use inductively coupled plasma (ICP) reactive-ion etching (RIE) to remove the BARC and niobium film according to the pattern. After the pattern is written, the unexposed resist and remaining BARC are etched in the dry process as well.

This process gave us very good films, by replacing the problematic factors of the wet process. The difficulties of the wet process mainly arise from the fact that HF is the only known effective wet etchant for niobium, but it is also very harsh. This created problems with the resist peeling. The dry etch does have a drawback of damaging the metal film by the ion bombardment. The relevance of this is not yet known, but may incentivize finding an effective wet process that does not use plasma etching. This would require finding a photoresist with good adhesion that is not damaged by HF.

6.5 Measurement

In order to measure the resonator properties, we need a way to mount them in a cryogenic environment and connect them to coaxial cables. The nominal superconducting transition temperature T_c of niobium is 9.25 K [RBD24], so we can use the PPMS insert from section 2.2. In place of the LGR box I made a box to hold the 10x10mm chip and a printed circuit board (PCB) made with a high-frequency-compatible substrate[1]. The sapphire sample itself rests on the aluminum box, though this only works for PPMS measurements which stay above aluminum's T_c, below which it is a poor thermal conductor.

The large pads on the perimeter of the chip (including ground) are connected to the gold-plated PCB transmission line by wire bonds. It was found that aluminum bonding wire was effective for bonding to niobium; gold did not stick.

The PCB has a larger coplanar waveguide line between two SMP connectors, with an open middle space where the superconducting device is connected in series. The SMP connectors take the place of the MMCX connectors used with the LGRs. The SMP connectors are soldered to a board cutout, and we found that it is important to prevent the solder migrating near the wire bonding site. This is most effective using solder paste melted on a hot plate to connect the very small SMP connector without affecting the wire bond pad.

Similar to the LGR PPMS measurements, with this setup we can reach temperatures near what the PPMS reaches without the insert, around 1.65 K.

We initially had trouble finding the resonances on the VNA. The problem was that the resonances are so sharp that they are invisible unless the VNA has resolution down to the kHz scale FWHM. The Keysight E5071C only allows 1601 points per measurement, so recording a broad spectrum requires connecting several narrowband

[1] Rogers Corporation RO4350B

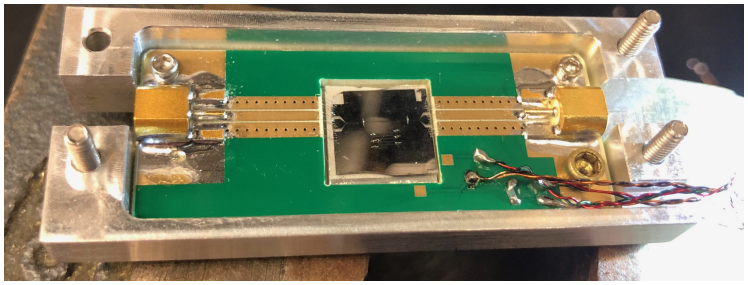

Figure 6.4: Photograph of the first chip design fabricated with a niobium film on sapphire, mounted in the PPMS box.

measurements. The first designs probably would work with the improved fabrication and narrowband measurement, but for the dry process we started with the JPL design.

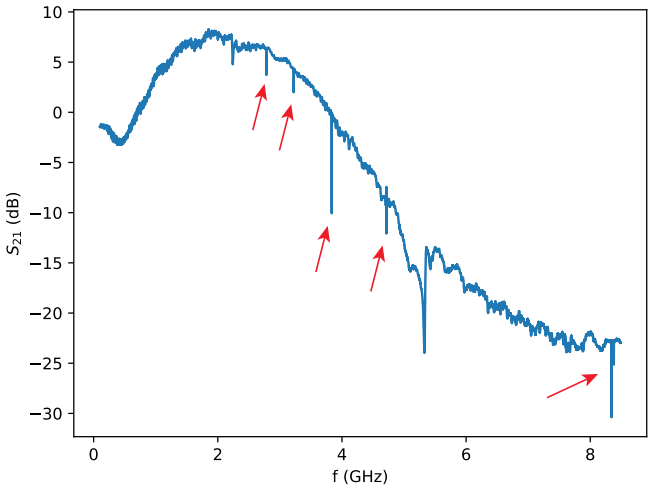

Figure 6.5: Broadband spectrum of a niobium resonator at 1.8 K using the PPMS insert. The modes marked with arrows are sharp superconductor modes, while the others are parasitic modes likely arising from the box or wire bonds.

6.6 Analysis

In order to analyze the superconducting resonators we need a model for the S_{21} data. In the case of the designs used here, we have a CPW transmission line connecting the two ports in series, with several “hanger" transmission line resonators coupled through adjacent transmission lines. At most frequencies, the signal passes through with a fairly constant amount of attenuation. When the VNA frequency matches the

resonant frequency of one of the resonators (or multiple, if the lengths of some are identical) that particular resonator absorbs some of the energy so that less passes through. That is to say, this is called a notch configuration, where S_{21} is normally high at most frequencies, and lower at specific resonances. This is in contrast to my LGRs where S_{21} is normally low and the only way to transmit between the two pins is to excite particular resonant modes. The lineshape is mostly the same, it is primarily a matter of X vs. 1-X. In principle, the superconducting resonators are analyzed the same way as those made from normal metals. The lineshape functions are mostly the same, but with a much larger Q. The copper LGRs are mostly on the order of $Q \sim 10^2 - 10^3$ while our Nb CPW resonators have achieved up to $Q_i = 1.87 \times 10^6$ at 1 K.

The narrow bandwidth of these resonators makes it easier to work with complex S_{21} data, either as real/imaginary, or magnitude/phase. The reason for this is that when measuring phase with a VNA, there is usually a sawtooth pattern when looking at phase as a function of frequency $\phi = \arg(S_{21}(f))$. This is caused by the delay experienced by signals propagating through transmission lines, mostly from coaxial cables. For the phase measurements shown previously, it is necessary to compensate for this. The delay time can be determined by the group delay t_g, given by $t_g = -\dfrac{\mathrm{d}\phi}{\mathrm{d}\omega}$ [Key]. Away from the resonance, this is a constant determined by the slope of the sawtooth curve. This gives the delay time caused by the transmission lines. This can be subtracted from the phase for a clean measurement. However, because the superconducting resonators have a very small bandwidth, the sawtooth effectively becomes a constant phase offset.

With the complex S_{21} being easier to use here, we can apply other methods to analyze the data. In particular, when we make an XY plot of $(\Re(S_{21}), \Im(S_{21}))$ we get a circle in the complex plane. This fact was used in [Pro+15a] to create an algorithm and software [seb24] to apply this fitting method to resonator measurements. For a notch type resonator like our niobium CPWs, they use the complex S_{21} transmission function in the form:

$$S_{21}^{\text{notch}}(f) = a e^{j\alpha} e^{-2\pi j f \tau} \left[1 - \frac{(Q_l/|Q_c|) e^{j\phi}}{1 + 2jQ_l(f/f_r - 1)} \right]. \tag{6.7}$$

The component before the brackets represents the effects of the environment outside the resonator: cables, connectors, amplifiers, etc. a represents an overall scaling

factor from external factors, and α is a fixed phase shift from them. $e^{-2\pi j f \tau}$ represents the delay from cables and such. The bracketed term represents the resonator itself. Q_l is the loaded quality factor and $|Q_c|$ is the absolute value of the coupling quality factor. The $e^{j\phi}$ term represents asymmetry which can arise from standing waves in the transmission lines connected to the resonator (perhaps at the wire bonds) or the input and output impedance seen by the resonator being slightly different on each side [Pro+15a]. The resonant frequency is given by f_r with f being the independent variable, frequency.

In regards to the first term, VNA measurements will often use a calibration kit which replaces the sample or device under test (DUT) and allows for a calibration of all effects that are not due to the DUT. However, this quite impractical for these cryogenic measurements, because there are several connectors and long cables that are not accessible when cold. However, as discussed previously, the superconducting resonators have such narrow bandwidths that the cable delay represented by $e^{-2\pi j f \tau}$ is effectively constant. The same is true for things like connectors, cables, and amplifiers which can also have frequency dependent loss; these become part of a constant factor through the resonator bandwidth [Pro+15a].

The internal quality factor represents the intrinsic behavior of the resonator and is thus the most meaningful. It is calculated in the usual way for combining quality factors [Pro+15a]:

$$\frac{1}{Q_i} = \frac{1}{Q_l} + \Re\left(\frac{1}{Q_i}\right). \tag{6.8}$$

6.7 SC resonator for LHF

As discussed previously, LGRs are good for microwave spectroscopy because the microwave magnetic field is fairly uniform over the sample volume, in terms of both magnitude and direction. This is beneficial in reducing inhomogeneous broadening. Additionally, the filling factor can be high. However, if we want to saturate an energy level with many MW photons, this can be difficult in LGRs. This is particularly true for case of stoichiometric rare earth crystals [2], where the concentration and number

[2] Meaning the composition is given by a normal chemical formula with integer coefficients, rather than a percentage or ppm doping. For example in our case, this refers to $LiYF_4$ with 100% of the yttrium replaced by the magnetic ion.

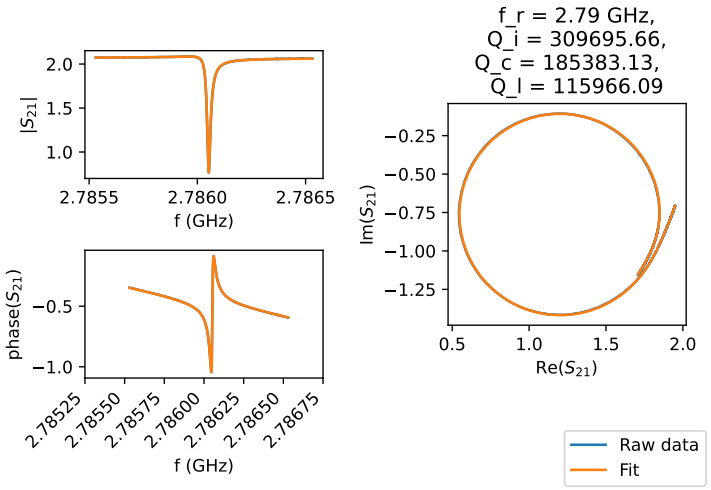

Figure 6.6: Niobium resonator spectrum at 1.8K in the PPMS, with the results of the circle fit described in [Pro+15a].

of ion spins is very high. The LGR will couple the input MW power to the entire sample, thus usually making it difficult to saturate a transition without excessive power and heating.

A CPW resonator made with a regular conductor would not provide a substantial improvement in this regard. However, a superconducting CPW resonator gives benefits in two factors: a smaller mode volume, and higher Q. The combination of a high Q and small mode volume allows us to focus many photons on a small number of spins, increasing prospects of saturation.

Conclusion

We have started work to produce improved superconducting resonators through the use of MBE to create cleaner films. Results have been promising so far, and further study will identify the benefits of these techniques. Measuring at single photon level and sufficiently low temperature will allow us to identify the benefits of these efforts in reducing TLS loss for superconducting circuits. Applying these insights to superconductors with magnetic field tolerance will show their use in nonlinear spin resonance experiments.

Chapter 7

Future Work

In this chapter, we will discuss possible future work based on these results and techniques.

7.1 Nonlinear pumping

A key feature of the $LiHoF_4$ phase diagram as shown in Fig. 1.2 is the upturn in the critical transverse field at low temperatures. The origin of this effect is seen when we calculate the phase diagram with and without the hyperfine term A. In this case the upturn disappears, and the phase diagram is as expected for the basic transverse field Ising system. This property raises an interesting prospect: is it possible to control this hyperfine coupling, and thus the magnetic ordering phase diagram? In particular, is it possible to drive the magnetic phase transition at rates faster than what can be realistically managed by directly ramping the magnetic field.

Understanding what happens when a system is driven through a phase transition at different rates is a universal topic in physics. For millennia blacksmiths have known how to quench steel to change its properties [Jin11]. The concept of quenching, or forcing a system through a phase transition, emerges in fields as distinct as galaxy formation in the early universe within cosmology and superfluid helium vortices [Zur85] and metallurgy in condensed matter. A universal concept that connects these systems is given by the Kibble-Zurek mechanism [Du+23], first developed by Kibble [Kib76] to describe how galaxies formed after the big bang along defects like cosmic strings, and it was applied to laboratory experiments by Zurek [Zur85].

The key result of the KZ theory can be used to describe the behavior of a system that is quenched through a phase transition. This can be applied to both classical (CPT) and quantum phase transitions (QPTs). The important distinction here is that classical phase transitions are driven by temperature, while QPTs can happen at zero temperature when a different parameter is varied, such as magnetic field.

Of course, in practice QPTs are studied at finite temperature, but to be precise the quantum critical point (QCP) is at absolute zero. Nonetheless, as long as the quantum fluctuations are much stronger than the thermal fluctuations, it is possible to discern the zero-temperature behavior. Either way, consider a system with an independent parameter g with a quantum critical point at $g = g_c$. For a driven quantum two-level system, the characteristic relaxation time is the inverse of the minimum gap and diverges at the QCP [Dut+15].

Following Dutta et al., we can consider a linear quench, where the parameter approaches g_c as t/τ, i.e., $\lambda = t/\tau = g - g_c$, with the critical point at $t = 0$, as shown in Fig. 7.1. The adiabatic theorem says that if the system's relaxation time is smaller than the time where g is varied, then the system stays in the ground state. When the variations happen faster than the relaxation time, we have non-adiabatic excitations. With the relaxation time given by ξ_τ, the crossover between adiabatic and non-adiabatic behavior can be given as [Dut+15]:

$$\left|\frac{\lambda}{\dot{\lambda}}\right| = \hat{t} = \xi_\tau(t = \hat{t}). \tag{7.1}$$

Universality gives that the correlation time diverges as $\xi_\tau \approx |g - g_c|^{-\nu z}$, so we can rewrite this transition as

$$\hat{t} \approx (g - g_c)^{-\eta z}|_{\hat{t}} \approx \left(\frac{\hat{t}}{\tau}\right) \tag{7.2}$$

which means $\hat{t} \approx \tau^{\nu z/(\nu z+1)}$. As seen in Fig. 7.1, at $\pm\hat{t}$ we see three regions where the behavior goes from adiabatic on the outside to the so-called critical slowing down in the center region. Returning to the context of a quantum ferromagnet, Kibble-Zurek theory gives us another critical concept. Using Eq. 7.1 and noting that the domain size is related to the healing length $\hat{\xi} \approx \xi_\tau^{1/z}$ and assuming one defect per domain, we can write the number density n of defects as

$$n \sim \frac{1}{\hat{\xi}^d} \sim \tau^{-\frac{d\nu}{\nu z+1}}, \tag{7.3}$$

where d is the dimensionality of the system, and z and ν are the critical exponents. In summary, in an experiment where we can quench a quantum system at rates above

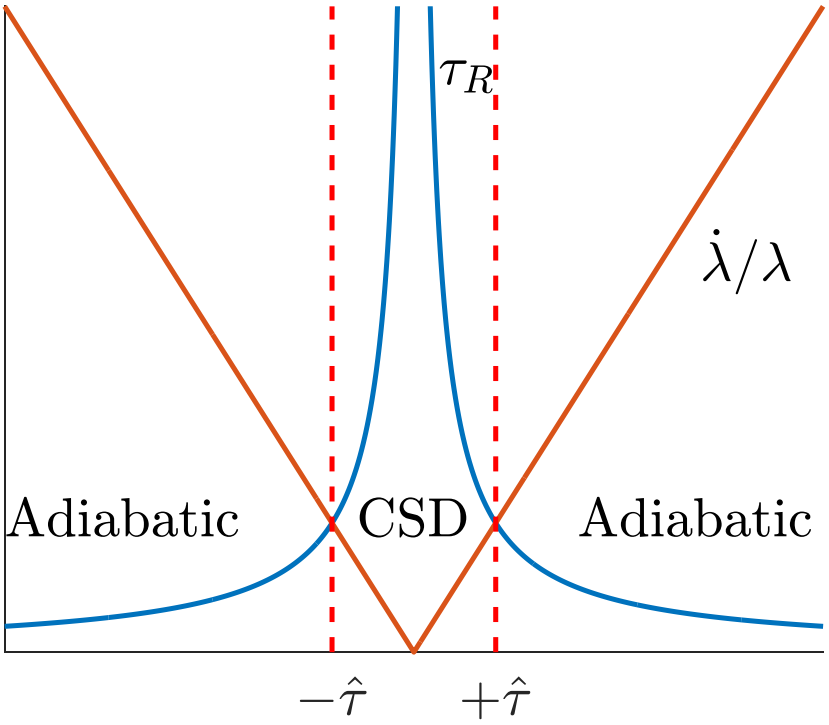

Figure 7.1: Illustration of the Kibble-Zurek mechanism in a linear quench. For $|t| < \hat{\tau}$ the Hamiltonian is changing faster than the diverging relaxation time, making this the critical slowing down regime. Outside the center regime, the Hamiltonian is changing slower than the relaxation time so the change takes effect adiabatically [Dut+15].

and below the critical rate, we can look for universal behavior in the resulting defect density. In a magnetic spin system, the defect density will roughly correspond to the magnetization or susceptibility.

Quench in $LiHoF_4$

Having described the general formulation of quantum quenches, we can now discuss how it might work in $LiHoF_4$. For a transverse field Ising model system, the obvious quench method would be to adjust the transverse magnetic field. However, the superconducting magnets required to produce fields of several Tesla have very high inductance. The driving current $i(t)$ that produces the field cannot be changed too fast due to the back-action voltage:

$$V = -L\frac{\mathrm{d}i}{\mathrm{d}t}. \tag{7.4}$$

Changing the current (thus field) too quickly creates arcing and can cause the superconductor itself to thermally quench when a portion becomes non-superconducting. This is not to be confused with a quantum quench in the TFIM sample, but rather a magnet quench which results in a dramatic boiling of liquid helium and loss of the magnetic field. A quickly changing magnetic field also generates eddy currents in the sample holder/resonator which would most likely lead to excessive heating which would make a controlled quantum quench difficult.

However, another property of the $LiHoF_4$ system might provide an opportunity for a quantum quench. As discussed previously, the $LiHoF_4$ phase diagram differs from that of a basic quantum transverse field Ising model by the upturn in critical field at low temperature. This happens because of the hyperfine coupling to ^{165}Ho nuclei, which couples the nuclear and electronic spin states together. This creates an effective composite spin $\mathbf{I} + \mathbf{J}$ which requires a higher transverse field in order to break ferromagnetic ordering [BRA96]. This leads to a possibility to explore–if we saturate the nuclear states, that degree of freedom is eliminated as the spins can go between the electronic states without needing to change nuclear energy levels. This would in turn reduce the magnetic field scale needed to break ferromagnetic ordering.

Measurements

In order to make these dynamic measurements possible, there are several factors that we must consider. First, we need a way to apply a short, high-power microwave pulse, and probe the microwave response (S_{21}) before, during, and after such a pulse. As mentioned previously, VNAs are not intended for measurements where timing is critical; measurements are taken on the scale of tenths of a second up to several seconds. Additionally, the measurement sequence is not well-defined, making it difficult to control the details of when power at each frequency is applied for measurement. There are also variable delays during the measurement sequence. In section 2.1 we developed the time-resolved measurement technique which will be important for any dynamic experiment working with short time scales.

The The timescale possible by this technique is $\tau = Q/(\pi f_0)$, in terms of the quality factor Q and resonant frequency f_0 [Gyü+15].

Measuring any kind of nonlinear effect requires care in order to avoid thermal effects, which usually occur on a fairly long timescale. For these measurements I took care to ensure that the average power remains the same. For example, if the goal is to maintain an average output power of P_{avg}, we must track how long t_{on} a high power level P_{on} is active, and then turn off the power for an appropriate time t_{off} in order to maintain the average power level P_{avg}. For example, if an average power of $P_{\text{avg}} = -20$ dBm $= 0.01$ mW is desired, and $P_{\text{on}} = -10$ dBm $= 0.1$ mW is active for $t_{\text{on}} = 1$ s, then the power should be off for $t_{\text{off}} = 9$ s. This can also be considered in terms of the duty cycle d, which is the fraction of the time that the power is on:

$$d = \frac{t_{\text{on}}}{t_{\text{on}} + t_{\text{off}}}. \tag{7.5}$$

The average power can also be written in terms of the duty cycle:

$$P_{\text{avg}} = \frac{t_{\text{on}}}{t_{\text{on}} + t_{\text{off}}} P_{\text{on}} = dP_{\text{on}}. \tag{7.6}$$

With special attention to thermal effects, we have surveyed various regimes looking for power dependence in $LiHoF_4$. We did not find any obvious change in the phase diagram up to a few milliwatts VNA source power. However, some measurements reveal power dependence at a lower field within the ferromagnetic state, as shown in Fig. 7.2.

The cause of this behavior at intermediate fields is not clear. One possibility is domain wall motion, which requires additional theoretical investigation. It could also be a different kind of Walker mode, though it is distinct from the well-defined Walker modes at higher frequency.

Another possible method to modulate the phase diagram and drive a quench was described by Gómez-León and Stamp [GS17]. This describes a dynamical quantum phase transition, occurring when a high frequency and power AC field is applied to the $LiHo_xY_{1-x}F_4$system (as well as similar systems). The AC field is assumed to be at frequencies much higher than the dipolar and hyperfine coupling strengths, but lower than the gap to the next crystal field level, thus $\approx 30 - 200$ GHz.

While this analysis leads to interesting results, the microwave field amplitude needed for a significant effect would require immense power input to the resonator and cause

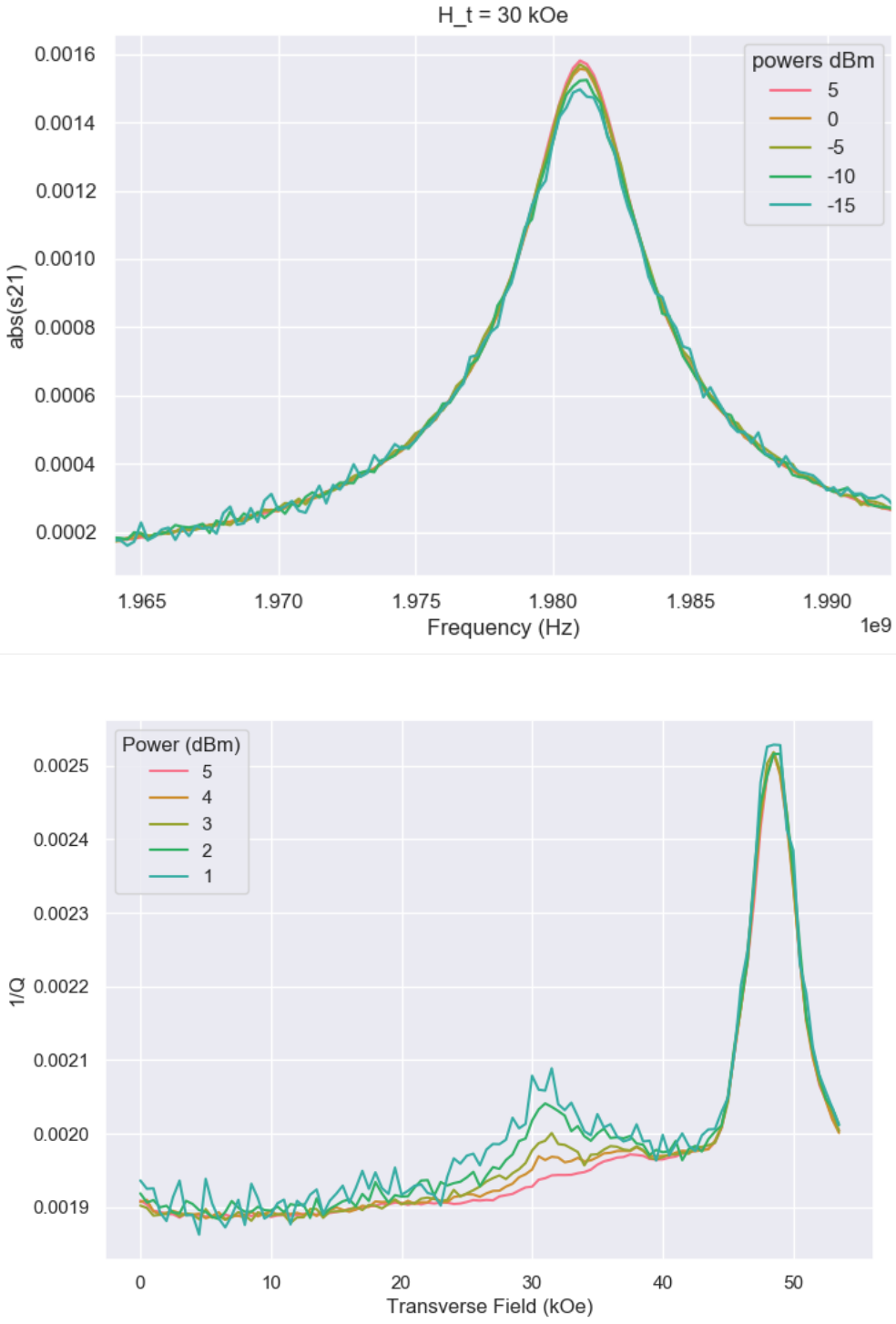

Figure 7.2: Measurements of power dependence of $LiHoF_4$ in a loop-gap resonator. (a) Power dependence of S_{21} for a 2 GHz resonator taken at 30 kOe, taken with appropriate delays to avoid heating. The results of taking this measurement at a wide field range and fitting for $1/Q$ are shown in (b). The phase transition does not shift appreciably, but there is a power dependent effect around 30 kOe. The cause of this absorption and its power dependence is unclear, as it does not correlate with any RPA electronuclear modes. Domain wall motion is a possible cause.

extreme heating. The magnitude of the effect is given as a function of $\alpha = \Gamma_x/\omega$, where $\Gamma \approx 1$ leads to a moderate effect. Γ is the AC field magnitude and ω is its frequency; thus the energy scale corresponding to Γ and ω are similar. The units here are strange, due to some constants being defined as equal to 1. The frequency corresponds to an energy of $h\nu \approx 2 \times 10^{-23}$J = for $\eta = 30$ GHz. The AC field magnitude of a typical LGR is $B_0 \approx (3.8 \times 10^{-4} P_0)$ T [WFH84]. Converting to energy,

$$E_\Gamma \approx g_L \mu_B B_0 \approx 7 \times 10^{-27} \times P_0 \tag{7.7}$$

Thus, the input power P_0 is on the order of a few kilowatts! A typical microwave oven is around 1 kW, so this is clearly not compatible with a dilution refrigerator. Further study of the dynamical phase transition theory is needed. As mentioned in chapter 6, superconducting resonators have the advantage of much higher Q's and allow for very small mode volume. While they have a drawback of increased inhomogeneity in microwave field magnitude and direction compared to LGRs, the combination of high Q and small mode volume increases photon density should make saturation more accessible.

Bibliography

[Col48] G. B. Collins, ed. *Microwave Magnetrons*. 1st ed. Radiation Laboratory Series. New York: McGraw-Hill Book Co., 1948.

[Ste52] K. W. H. Stevens. "Matrix Elements and Operator Equivalents Connected with the Magnetic Properties of Rare Earth Ions." In: *Proceedings of the Physical Society. Section A* 65.3 (Mar. 1952), pp. 209–215. ISSN: 0370-1298. DOI: 10.1088/0370-1298/65/3/308. (Visited on 04/25/2024).

[AT55] J. O. Artman and P. E. Tannenwald. "Measurement of Susceptibility Tensor in Ferrites." In: *Journal of Applied Physics* 26.9 (Sept. 1955), pp. 1124–1132. ISSN: 0021-8979, 1089-7550. DOI: 10.1063/1.1722165. (Visited on 04/06/2021).

[Wal57] L. R. Walker. "Magnetostatic Modes in Ferromagnetic Resonance." In: *Physical Review* 105.2 (Jan. 1957), pp. 390–399. ISSN: 0031-899X. DOI: 10.1103/PhysRev.105.390. (Visited on 04/10/2020).

[Nak58] T. Nakamura. "Indirect Coupling of Nuclear Spins in Antiferromagnet with Particular Reference to MnF_2 at Very Low Temperatures." In: *Progress of Theoretical Physics* 20.4 (Oct. 1958), pp. 542–552. ISSN: 0033-068X. DOI: 10.1143/PTP.20.542. (Visited on 06/27/2024).

[Suh58] H. Suhl. "Effective Nuclear Spin Interactions in Ferromagnets." In: *Physical Review* 109.2 (Jan. 1958), pp. 606–606. ISSN: 0031-899X. DOI: 10.1103/PhysRev.109.606. (Visited on 04/10/2020).

[KE60] C. Kooy and U. Enz. "Experimental and Theoretical Study of the Domain Configuration in Thin Layers of $BaFe_{12}0_{19}$." In: *Philips Research Reports* 15 (1960), pp. 7–29.

[de +63] P. G. de Gennes et al. "Nuclear Magnetic Resonance Modes in Magnetic Material. I. Theory." In: *Physical Review* 129.3 (Feb. 1963), pp. 1105–1115. DOI: 10.1103/PhysRev.129.1105. (Visited on 04/08/2020).

[HGB63] A. J. Heeger, S. K. Ghosh, and T. G. Blocker III. "Mn55 Nuclear Magnetic Resonance in Manganese Ferrite." In: *Journal of Applied Physics* 34.4 (Apr. 1963), pp. 1034–1035. ISSN: 0021-8979. DOI: 10.1063/1.1729358. (Visited on 06/06/2024).

[TK66] E. A. Turov and V. G. Kuleev. “Coupled Oscillations of Electronic and Nuclear Spins in Antiferromagnets.” In: *Journal of Experimental and Theoretical Physics (USSR)* 22.1 (1966), p. 176.

[Blo67] T. G. Blocker. “Coupled Electron-Nuclear Magnetostatic Modes in Magnetic Materials.” In: *Physical Review* 154.2 (Feb. 1967), pp. 446–447. ISSN: 0031-899X. DOI: 10.1103/PhysRev.154.446. (Visited on 04/10/2020).

[CJ73] M. G. Cottam and M. J. Jones. “Theory of Nuclear Spin Interactions in Ferromagnetic Insulators. I. The Thermodynamic Properties.” In: *Journal of Physics C: Solid State Physics* 6.6 (Mar. 1973), pp. 1007–1019. ISSN: 0022-3719. DOI: 10.1088/0022-3719/6/6/015. (Visited on 06/27/2024).

[Bat+75] J. E. Battison et al. “Ferromagnetism in Lithium Holmium Fluoride-$LiHoF_4$. II. Optical and Spectroscopic Measurements.” In: *Journal of Physics C: Solid State Physics* 8.23 (Dec. 1975), pp. 4089–4095. ISSN: 0022-3719. DOI: 10.1088/0022-3719/8/23/022. (Visited on 05/14/2020).

[HJN75] P. E. Hansen, T. Johansson, and R. Nevald. “Magnetic Properties of Lithium Rare-Earth Fluorides: Ferromagnetism in $LiErF_4$ and $LiHoF_4$ and Crystal-Field Parameters at the Rare-Earth and Li Sites.” In: *Physical Review B* 12.11 (Dec. 1975), pp. 5315–5324. DOI: 10.1103/PhysRevB.12.5315. (Visited on 04/16/2024).

[Her76] J. A. Hertz. “Quantum Critical Phenomena.” In: *Physical Review B* 14.3 (Aug. 1976), pp. 1165–1184. DOI: 10.1103/PhysRevB.14.1165.

[HA76] S. Hunklinger and W. Arnold. “Ultrasonic Properties of Glasses at Low Temperatures.” In: *Physical Acoustics*. Ed. by W. P. Mason and R. N. Thurston. Vol. 12. Academic Press, Jan. 1976, pp. 155–215. DOI: 10.1016/B978-0-12-477912-9.50008-4. (Visited on 01/04/2024).

[Kib76] T. W. B. Kibble. “Topology of Cosmic Domains and Strings.” In: *Journal of Physics A: Mathematical and General* 9.8 (Aug. 1976), pp. 1387–1398. ISSN: 0305-4470, 1361-6447. DOI: 10.1088/0305-4470/9/8/029. (Visited on 11/01/2018).

[EEA79] L. Esterowitz, R. C. Eckardt, and R. E. Allen. “Long-wavelength Stimulated Emission via Cascade Laser Action in Ho : YLF.” In: *Applied Physics Letters* 35.3 (Aug. 1979), pp. 236–239. ISSN: 0003-6951. DOI: 10.1063/1.91083. (Visited on 07/18/2024).

[GBG80] D. Gettemy, N. P. Barnes, and E. Griggs. “Liquid Nitrogen Cooled Laser Rod Holder Design.” In: *Review of Scientific Instruments* 51.9 (Sept. 1980), pp. 1194–1197. ISSN: 0034-6748. DOI: 10.1063/1.1136393. (Visited on 03/14/2024).

[HW81] W. N. Hardy and L. A. Whitehead. “Split-Ring Resonator for Use in Magnetic Resonance from 200–2000 MHz.” In: *Review of Scientific Instruments* 52.2 (Feb. 1981), pp. 213–216. ISSN: 0034-6748, 1089-7623. DOI: 10.1063/1.1136574. (Visited on 04/09/2024).

[CL82] B. Cook and I. J. Lowe. “A Large-Inductance, High-Frequency, High-Q, Series-Tuned Coil for NMR.” In: *Journal of Magnetic Resonance (1969)* 49.2 (Sept. 1982), pp. 346–349. ISSN: 0022-2364. DOI: 10.1016/0022-2364(82)90200-1. (Visited on 04/08/2024).

[FH82] W. Froncisz and J. S. Hyde. “The Loop-Gap Resonator: A New Microwave Lumped Circuit ESR Sample Structure.” In: *Journal of Magnetic Resonance (1969)* 47.3 (May 1982), pp. 515–521. ISSN: 00222364. DOI: 10.1016/0022-2364(82)90221-9. (Visited on 04/11/2024).

[WFH84] R. L. Wood, W. Froncisz, and J. S. Hyde. “The Loop-Gap Resonator. II. Controlled Return Flux Three-Loop, Two-Gap Microwave Resonators for ENDOR and ESR Spectroscopy.” In: *Journal of Magnetic Resonance (1969)* 58.2 (June 1984), pp. 243–253. ISSN: 00222364. DOI: 10.1016/0022-2364(84)90214-2. (Visited on 10/05/2018).

[Bri85] J. E. Brittain. “The Magnetron and the Beginnings of the Microwave Age.” In: *Physics Today* 38.7 (July 1985), pp. 60–67. ISSN: 0031-9228, 1945-0699. DOI: 10.1063/1.880982. (Visited on 06/30/2024).

[GG85] M. Gabay and T. Garel. “Phase Transitions and Size Effects in the Ising Dipolar Magnet.” In: *J. Physique Lett.* 46 (1985), pp. L-989-L–997.

[Zur85] W. H. Zurek. “Cosmological Experiments in Superfluid Helium?” In: *Nature* 317.6037 (Oct. 1985), pp. 505–508. ISSN: 1476-4687. DOI: 10.1038/317505a0. (Visited on 11/12/2018).

[Phi87] W. A. Phillips. “Two-Level States in Glasses.” In: *Reports on Progress in Physics* 50.12 (Dec. 1987), p. 1657. ISSN: 0034-4885. DOI: 10.1088/0034-4885/50/12/003. (Visited on 06/26/2024).

[Pom+88] J. Pommier et al. “(H, T) Phase Diagram of a Uniaxial Dipolar Ferromagnet : $LiHoF_4$.” In: *Le Journal de Physique Colloques* 49.C8 (Dec. 1988), pp. C8-1949-C8–1950. ISSN: 0449-1947. DOI: 10.1051/jphyscol:19888882. (Visited on 02/14/2024).

[HS89] M. A. Herman and H. Sitter. *Molecular Beam Epitaxy*. Ed. by U. Gonser et al. Vol. 7. Springer Series in Materials Science. Berlin, Heidelberg: Springer, 1989. ISBN: 978-3-642-97098-6. DOI: 10.1007/978-3-642-97098-6. (Visited on 08/02/2024).

[MPF89] P. Meyer, J. Pommier, and J. Ferre. “Magnetooptic Observation Of Domains At Low Temperature In The Transparent Ferromagnet $LiHoF_4$.” In: *Electro-Optic and Magneto-Optic Materials and Applications*. Vol. 1126. International Society for Optics and Photonics, Dec. 1989, pp. 93–98. DOI: 10.1117/12.961386. (Visited on 08/23/2021).

[THK89] Y. Tarutani, M. Hirano, and U. Kawabe. “Niobium-Based Integrated Circuit Technologies.” In: *Proceedings of the IEEE* 77.8 (Aug. 1989), pp. 1164–1176. ISSN: 1558-2256. DOI: 10.1109/5.34117. (Visited on 08/03/2024).

[JM91] J. Jensen and A. R. Mackintosh. *Rare Earth Magnetism: Structures and Excitations*. Oxford University Press, June 1991. ISBN: 978-0-19-852027-6. DOI: 10.1093/oso/9780198520276.001.0001. (Visited on 03/15/2024).

[BRA96] D. Bitko, T. F. Rosenbaum, and G. Aeppli. “Quantum Critical Behavior for a Model Magnet.” In: *Physical Review Letters* 77.5 (July 1996), pp. 940–943. ISSN: 0031-9007, 1079-7114. DOI: 10.1103/PhysRevLett.77.940. (Visited on 10/08/2018).

[NN96] H. Nishimori and Y. Nonomura. “Quantum Effects in Neural Networks.” In: *Journal of the Physical Society of Japan* 65.12 (1996), pp. 3780–3796. DOI: 10.1143/jpsj.65.3780.

[Pro+97] L. A. Prozorova et al. “Investigation of the Hyperfine Interaction in the Antiferromagnetic $CsMnI_3$.” In: *Journal of Experimental and Theoretical Physics* 85.5 (Nov. 1997), pp. 1035–1038. ISSN: 1090-6509. DOI: 10.1134/1.558416. (Visited on 07/26/2024).

[PS98] N. V. Prokof’ev and P. C. E. Stamp. “Low-Temperature Quantum Relaxation in a System of Magnetic Nanomolecules.” In: *Physical Review Letters* 80.26 (June 1998), pp. 5794–5797. ISSN: 0031-9007, 1079-7114. DOI: 10.1103/PhysRevLett.80.5794. (Visited on 04/02/2019).

[ZF99] G. L. Zhou and C. P. Flynn. “Fingered Morphology of Niobium (110) Grown by Molecular-Beam Epitaxy.” In: *Physical Review B* 59.12 (Mar. 1999), pp. 7860–7867. DOI: 10.1103/PhysRevB.59.7860. (Visited on 08/03/2024).

[PS00] N. V. Prokof’ev and P. C. E. Stamp. “Theory of the Spin Bath.” In: *Rep. Prog. Phys.* 63 (2000), pp. 669–726.

[Gir+01] R. Giraud et al. “Nuclear Spin Driven Quantum Relaxation in $LiY_{0.998}Ho_{0.002}F_4$.” In: *Physical Review Letters* 87 (2001), p. 057203. DOI: 10.1103/PhysRevLett.87.057203.

[WMT01] A. R. Wildes, J. Mayer, and K. Theis-Bröhl. “The Growth and Structure of Epitaxial Niobium on Sapphire.” In: *Thin Solid Films* 401.1 (Dec. 2001), pp. 7–34. ISSN: 0040-6090. DOI: 10.1016/S0040-6090(01)01631-5. (Visited on 04/07/2023).

[BD02] V. Banerjee and S. Dattagupta. “Model Quantum Magnet. II. Calculation of NMR Line Shapes.” In: *Physical Review B* 66.6 (Aug. 2002), p. 064418. ISSN: 0163-1829, 1095-3795. DOI: 10.1103/PhysRevB.66.064418. (Visited on 05/12/2020).

[BSW02] R. Benedek, D. N. Seidman, and C. Woodward. “The Effect of Misfit on Heterophase Interface Energies.” In: *Journal of Physics: Condensed Matter* 14.11 (Mar. 2002), p. 2877. ISSN: 0953-8984. DOI: 10.1088/0953-8984/14/11/307. (Visited on 08/03/2024).

[Day+03] P. K. Day et al. “A Broadband Superconducting Detector Suitable for Use in Large Arrays.” In: *Nature* 425.6960 (Oct. 2003), pp. 817–821. ISSN: 1476-4687. DOI: 10.1038/nature02037. (Visited on 01/06/2024).

[WGP03] R. C. C. Ward, E. J. Grier, and A. K. Petford-Long. “MBE Growth of (1 1 0) Refractory Metals on a-Plane Sapphire.” In: *Journal of Materials Science: Materials in Electronics* 14.9 (Sept. 2003), pp. 533–539. ISSN: 1573-482X. DOI: 10.1023/A:1024585400149. (Visited on 10/04/2024).

[Cha+04] P. B. Chakraborty et al. “Theory of the Magnetic Phase Diagram of $LiHoF_4$.” In: *Physical Review B* 70 (2004), p. 144411. DOI: 10.1103/PhysRevB.70.144411.

[Che+04] L. F. Chen et al. *Microwave Electronics: Measurement and Materials Characterization*. Wiley, Apr. 2004. ISBN: 978-0-470-84492-2.

[Coo+04] K. B. Cooper et al. “Observation of Quantum Oscillations between a Josephson Phase Qubit and a Microscopic Resonator Using Fast Readout.” In: *Physical Review Letters* 93.18 (Oct. 2004), p. 180401. DOI: 10.1103/PhysRevLett.93.180401. (Visited on 07/26/2024).

[Røn+05] H. M. Rønnow et al. “Quantum Phase Transition of a Magnet in a Spin Bath.” In: *Science (New York, N.Y.)* 308 (2005), pp. 389–392.

[SS05] M. Schechter and P. C. E. Stamp. “Significance of the Hyperfine Interactions in the Phase Diagram of LiHo x Y 1 - x F 4.” In: *Physical Review Letters* 95.26 (Dec. 2005). ISSN: 0031-9007, 1079-7114. DOI: 10.1103/PhysRevLett.95.267208. (Visited on 10/04/2018).

[Eki06] J. Ekin. *Experimental Techniques for Low-Temperature Measurements: Cryostat Design, Material Properties and Superconductor Critical-Current Testing*. Oxford: Oxford University Press, Incorporated, 2006. ISBN: 978-0-19-152469-1. (Visited on 03/12/2024).

[GSV06] D. Gatteschi, R. Sessoli, and J. Villain. *Molecular Nanomagnets*. Oxford University Press, Mar. 2006. ISBN: 978-0-19-856753-0. DOI: 10.1093/acprof:oso/9780198567530.001.0001. (Visited on 07/26/2024).

[YB06] B. Yurke and E. Buks. “Performance of Cavity-Parametric Amplifiers, Employing Kerr Nonlinearites, in the Presence of Two-Photon Loss.” In: *Journal of Lightwave Technology* 24.12 (Dec. 2006), pp. 5054–5066. ISSN: 1558-2213. DOI: 10.1109/JLT.2006.884490. (Visited on 06/21/2024).

[Ber+07] S. Bertaina et al. “Rare-Earth Solid-State Qubits.” In: *Nature Nanotechnology* 2.1 (Jan. 2007), pp. 39–42. ISSN: 1748-3387, 1748-3395. DOI: 10.1038/nnano.2006.174. (Visited on 08/23/2018).

[CC07] J. Choma and W.-K. Chen. *Feedback Networks: Theory and Circuit Applications*. World Scientific, 2007. ISBN: 978-981-02-2770-8.

[Røn+07] H. M. Rønnow et al. “Magnetic Excitations near the Quantum Phase Transition in the Ising Ferromagnet $LiHoF_4$.” In: *Physical Review B* 75.5 (Feb. 2007), p. 054426. DOI: 10.1103/PhysRevB.75.054426.

[ML08] J. Mispelter and M. Lupu. “Homogeneous Resonators for Magnetic Resonance: A Review.” In: *Comptes Rendus. Chimie* 11.4-5 (2008), pp. 340–355. ISSN: 1878-1543. DOI: 10.1016/j.crci.2007.10.003. (Visited on 04/06/2024).

[Tab+08] S. M. A. Tabei et al. “Perturbative Quantum Monte Carlo Study of LiHoF 4 in a Transverse Magnetic Field.” In: *Physical Review B* 78.18 (Nov. 2008), p. 184408. ISSN: 1098-0121, 1550-235X. DOI: 10.1103/PhysRevB.78.184408. (Visited on 06/12/2024).

[Kra09] C. Kraemer, ed. *Quantum Phase Transitions in a Magnetic Model System*. ETH-Zurich, 2009.

[WAW09] A. T. S. Wan, M. H. S. Amin, and S. X. Wang. “Landau-Zener Transitions in the Presence of Spin Environment.” In: *International Journal of Quantum Information* 07.04 (June 2009), pp. 725–737. ISSN: 0219-7499. DOI: 10.1142/S0219749909005353. (Visited on 07/26/2024).

[For10] P. Forn-Diaz. “Superconducting Qubits and Quantum Resonators.” PhD thesis. Sept. 2010.

[Sch+10] D. I. Schuster et al. “High-Cooperativity Coupling of Electron-Spin Ensembles to Superconducting Cavities.” In: *Physical Review Letters* 105.14 (Sept. 2010), p. 140501. ISSN: 0031-9007, 1079-7114. DOI: 10.1103/PhysRevLett.105.140501. (Visited on 09/18/2019).

[Jin11] Jindal. *Material Science and Metallurgy:* Pearson Education India, 2011. ISBN: 978-93-325-0125-6.

[Mis11] S. K. Misra. *Multifrequency Electron Paramagnetic Resonance: Theory and Applications*. John Wiley & Sons, Mar. 2011. ISBN: 978-3-527-63355-5.

[Poz11] D. M. Pozar. *Microwave Engineering*. John Wiley & Sons, Nov. 2011. ISBN: 978-0-470-63155-3.

[Sac11] S. Sachdev. *Quantum Phase Transitions*. 2nd ed. Cambridge: Cambridge University Press, 2011. ISBN: 978-0-521-51468-2. DOI: 10.1017/CBO9780511973765. (Visited on 07/06/2024).

[Tak+11] S. Takahashi et al. “Decoherence in Crystals of Quantum Molecular Magnets.” In: *Nature* 476.7358 (Aug. 2011), pp. 76–79. ISSN: 0028-0836, 1476-4687. DOI: 10.1038/nature10314. (Visited on 11/07/2018).

[AB12] A. Abragam and B. Bleaney. *Electron Paramagnetic Resonance of Transition Ions*. OUP Oxford, June 2012. ISBN: 978-0-19-102300-2.

[Gha12] N. N. Ghanepour. “Classical and Quantum Critical Phenomena in the Dipolar Antiferromagnet $LiErF_4$.” PhD thesis. EPFL, 2012. DOI: 10.5075/epfl-thesis-5372. (Visited on 01/27/2021).

[Kra+12] C. Kraemer et al. “Dipolar Antiferromagnetism and Quantum Criticality in $LiErF_4$.” In: *Science* 336.6087 (June 2012), pp. 1416–1419. ISSN: 0036-8075, 1095-9203. DOI: 10.1126/science.1221878. (Visited on 04/16/2024).

[Poz12] D. M. Pozar. *Microwave Engineering*. Chichester, UNITED STATES: Wiley, 2012. ISBN: 978-1-118-21363-6. (Visited on 06/22/2024).

[Zmu12] J. Zmuidzinas. “Superconducting Microresonators: Physics and Applications.” In: *Annual Review of Condensed Matter Physics* 3.1 (2012), pp. 169–214. DOI: 10.1146/annurev-conmatphys-020911-125022. (Visited on 11/08/2022).

[Hue+13] H. Huebl et al. “High Cooperativity in Coupled Microwave Resonator Ferrimagnetic Insulator Hybrids.” In: *Physical Review Letters* 111.12 (Sept. 2013), p. 127003. DOI: 10.1103/PhysRevLett.111.127003. (Visited on 07/26/2024).

[Mor+13] G. W. Morley et al. “Quantum Control of Hybrid Nuclear–Electronic Qubits.” In: *Nature Materials* 12.2 (Feb. 2013), pp. 103–107. ISSN: 1476-4660. DOI: 10.1038/nmat3499.

[SIC13] S. Suzuki, J.-i. Inoue, and B. K. Chakrabarti. *Quantum Ising Phases and Transitions in Transverse Ising Models*. Vol. 862. Lecture Notes in Physics. Berlin, Heidelberg: Springer, 2013. ISBN: 978-3-642-33039-1. DOI: 10.1007/978-3-642-33039-1. (Visited on 03/30/2024).

[Bab+15] P. Babkevich et al. “Neutron Spectroscopic Study of Crystal-Field Excitations and the Effect of the Crystal Field on Dipolar Magnetism in Li R F 4 (R = Gd , Ho, Er, Tm, and Yb).” In: *Physical Review B* 92.14 (Oct. 2015), p. 144422. ISSN: 1098-0121, 1550-235X. DOI: 10.1103/PhysRevB.92.144422. (Visited on 03/21/2024).

[Bob15] J. S. Bobowski. “Using Split-Ring Resonators to Measure Complex Permittivity and Permeability.” In: *2015 Conference on Laboratory Instruction Beyond the First Year*. College Park, MD: American Association of Physics Teachers, Nov. 2015, pp. 20–23. DOI: 10.1119/bfy.2015.pr.005. (Visited on 04/08/2024).

[Dut+15] A. Dutta et al. *Quantum Phase Transitions in Transverse Field Spin Models: From Statistical Physics to Quantum Information*. Cambridge University Press, Jan. 2015. ISBN: 978-1-316-39541-7.

[Gyü+15] B. Gyüre et al. "A Time Domain Based Method for the Accurate Measurement of Q-factor and Resonance Frequency of Microwave Resonators." In: *Review of Scientific Instruments* 86.9 (Sept. 2015), p. 094702. ISSN: 0034-6748. DOI: 10.1063/1.4929865. (Visited on 04/06/2024).

[Pro+15a] S. Probst et al. "Efficient and Robust Analysis of Complex Scattering Data under Noise in Microwave Resonators." In: *Review of Scientific Instruments* 86.2 (Feb. 2015), p. 024706. ISSN: 0034-6748, 1089-7623. DOI: 10.1063/1.4907935. (Visited on 12/06/2018).

[Pro+15b] S. Probst et al. "Microwave Multimode Memory with an Erbium Spin Ensemble." In: *Physical Review B* 92.1 (July 2015), p. 014421. ISSN: 1098-0121, 1550-235X. DOI: 10.1103/PhysRevB.92.014421. (Visited on 10/04/2024).

[Ang+16] A. Angerer et al. "Collective Strong Coupling with Homogeneous Rabi Frequencies Using a 3D Lumped Element Microwave Resonator." In: *Applied Physics Letters* 109.3 (July 2016), p. 033508. ISSN: 0003-6951, 1077-3118. DOI: 10.1063/1.4959095. (Visited on 07/01/2019).

[Boh+16] J. G. Bohnet et al. "Quantum Spin Dynamics and Entanglement Generation with Hundreds of Trapped Ions." In: *Science* 352.6291 (June 2016), pp. 1297–1301. DOI: 10.1126/science.aad9958. (Visited on 04/18/2024).

[Du+16] J. L. Du et al. "What Determines the Interfacial Configuration of Nb/Al2O3 and Nb/MgO Interface." In: *Scientific Reports* 6.1 (Oct. 2016), p. 33931. ISSN: 2045-2322. DOI: 10.1038/srep33931. (Visited on 08/03/2024).

[Kov+16] I. Kovacevic et al. "Probing Strongly Hybridized Nuclear-Electronic States in a Model Quantum Ferromagnet." In: *Physical Review B* 94.21 (Dec. 2016), p. 214433. DOI: 10.1103/PhysRevB.94.214433.

[Kov16] I. Kovacevic. "Probing Entangled States of the Nuclear-Electronic Quantum Magnet LiHoF4." PhD thesis. EPFL, 2016.

[McK16] R. McKenzie. "Fluctuations and Phase Transitions in Quantum Ising Systems." PhD thesis. University of British Columbia, 2016. DOI: 10.14288/1.0314166. (Visited on 08/29/2018).

[NMG16] C. Nico, T. Monteiro, and M. P. F. Graça. "Niobium Oxides and Niobates Physical Properties: Review and Prospects." In: *Progress in Materials Science* 80 (July 2016), pp. 1–37. ISSN: 0079-6425. DOI: 10.1016/j.pmatsci.2016.02.001. (Visited on 08/02/2024).

[Ped+16] K. S. Pedersen et al. “Toward Molecular 4f Single-Ion Magnet Qubits.” In: *Journal of The American Chemical Society* 138.18 (May 2016), pp. 5801–5804. ISSN: 0002-7863. DOI: 10.1021/jacs.6b02702.

[Pro16] S. Probst. “Hybrid Quantum System Based on Rare Earth Doped Crystals.” PhD thesis. KIT Scientific Publishing, Sept. 2016.

[YML16] W. Yang, W.-L. Ma, and R.-B. Liu. “Quantum Many-Body Theory for Electron Spin Decoherence in Nanoscale Nuclear Spin Baths.” In: *Reports on Progress in Physics* 80.1 (Nov. 2016), p. 016001. ISSN: 0034-4885. DOI: 10.1088/0034-4885/80/1/016001. (Visited on 07/26/2024).

[Ber+17] H. Bernien et al. “Probing Many-Body Dynamics on a 51-Atom Quantum Simulator.” In: *Nature* 551.7682 (Nov. 2017), pp. 579–584. ISSN: 1476-4687. DOI: 10.1038/nature24622. (Visited on 04/18/2024).

[GS17] Á. Gómez-León and P. C. E. Stamp. “Dynamical Quantum Phase Transitions in Presence of a Spin Bath.” In: *Physical Review B* 95.5 (Feb. 2017). ISSN: 2469-9950, 2469-9969. DOI: 10.1103/PhysRevB.95.054402. (Visited on 11/01/2018).

[Jur+17] P. Jurcevic et al. “Direct Observation of Dynamical Quantum Phase Transitions in an Interacting Many-Body System.” In: *Physical Review Letters* 119.8 (Aug. 2017), p. 080501. DOI: 10.1103/PhysRevLett.119.080501. (Visited on 04/18/2024).

[AL18] T. Albash and D. A. Lidar. “Adiabatic Quantum Computation.” In: *Reviews of Modern Physics* 90.1 (Jan. 2018), p. 015002. DOI: 10.1103/RevModPhys.90.015002. (Visited on 04/18/2024).

[Bal+18] J. R. Ball et al. “Loop-Gap Microwave Resonator for Hybrid Quantum Systems.” In: *Applied Physics Letters* 112.20 (May 2018), p. 204102. ISSN: 0003-6951, 1077-3118. DOI: 10.1063/1.5025744. (Visited on 11/15/2018).

[Bob18] J. S. Bobowski. “Probing Split-Ring Resonator Permeabilities with Loop-Gap Resonators.” In: *Canadian Journal of Physics* 96 (Aug. 2018), pp. 878–886. ISSN: 0008-4204. DOI: 10.1139/cjp-2017-0436. (Visited on 04/08/2024).

[Eis18] E. R. Eisenach. “Tunable and Broadband Loop Gap Resonator for Nitrogen Vacancy Centers in Diamond.” Thesis. Massachusetts Institute of Technology, 2018. (Visited on 11/15/2018).

[MS18] R. D. McKenzie and P. C. E. Stamp. “Thermodynamics of a Quantum Ising System Coupled to a Spin Bath.” In: *Physical Review B* 97.21 (June 2018), p. 214430. DOI: 10.1103/PhysRevB.97.214430. (Visited on 03/14/2024).

[AH19] H. Asahi and Y. Horikoshi. *Molecular Beam Epitaxy: Materials and Applications for Electronics and Optoelectronics*. Wiley Series in Materials for Electronic & Optoelectronic Applications. Hoboken: Wiley, 2019. ISBN: 978-1-119-35498-7.

[DB19] J. Dubreuil and J. S. Bobowski. "Ferromagnetic Resonance in the Complex Permeability of an Fe_3O_4 Nanosuspension at Radio and Microwave Frequencies." In: *Journal of Magnetism and Magnetic Materials* 489 (Nov. 2019), p. 165387. ISSN: 03048853. DOI: 10.1016/j.jmmm.2019.165387. arXiv: 1811.01168 [cond-mat, physics:physics]. (Visited on 07/15/2024).

[Eve+19] J. R. Everts et al. "Microwave to Optical Photon Conversion via Fully Concentrated Rare-Earth-Ion Crystals." In: *Physical Review A* 99.6 (June 2019), p. 063830. ISSN: 2469-9926, 2469-9934. DOI: 10.1103/PhysRevA.99.063830. (Visited on 05/31/2024).

[Flo+19] G. Flower et al. "Experimental Implementations of Cavity-Magnon Systems: From Ultra Strong Coupling to Applications in Precision Measurement." In: *New Journal of Physics* 21.9 (Sept. 2019), p. 095004. ISSN: 1367-2630. DOI: 10.1088/1367-2630/ab3e1c. (Visited on 07/04/2024).

[LSK19a] M. M. Libersky, D. M. Silevitch, and A. Kouki. "Design of a Loop-Gap Resonator with Bimodal Uniform Fields Using Finite Element Analysis." In: *2019 22nd International Conference on the Computation of Electromagnetic Fields (COMPUMAG)*. July 2019, pp. 1–4. DOI: 10.1109/COMPUMAG45669.2019.9032729.

[LSK19b] M. M. Libersky, D. M. Silevitch, and A. Kouki. "Design of a Loop-Gap Resonator with Bimodal Uniform Fields Using Finite Element Analysis." In: *arXiv:1910.12479 [appl.phys]* (Oct. 2019). arXiv: 1910.12479 [appl.phys].

[MCL19] C. Müller, J. H. Cole, and J. Lisenfeld. "Towards Understanding Two-Level-Systems in Amorphous Solids: Insights from Quantum Circuits." In: *Reports on Progress in Physics* 82.12 (Dec. 2019), p. 124501. ISSN: 0034-4885, 1361-6633. DOI: 10.1088/1361-6633/ab3a7e. (Visited on 01/05/2024).

[McA+20] S. McArdle et al. "Quantum Computational Chemistry." In: *Reviews of Modern Physics* 92.1 (Mar. 2020), p. 015003. DOI: 10.1103/RevModPhys.92.015003. (Visited on 07/26/2024).

[Nie+20] D. Niepce et al. "Geometric Scaling of Two-Level-System Loss in Superconducting Resonators." In: *Superconductor Science and Technology* 33.2 (Jan. 2020), p. 025013. ISSN: 0953-2048. DOI: 10.1088/1361-6668/ab6179. (Visited on 12/13/2023).

[Tho+20] C. N. Thomas et al. “Nonlinear Effects in Superconducting Thin Film Microwave Resonators.” In: *New Journal of Physics* 22.7 (July 2020), p. 073028. ISSN: 1367-2630. DOI: 10.1088/1367-2630/ab97e8. (Visited on 06/24/2024).

[Eis21] H. Eisenlohr. “Frontiers of quantum criticality: Mott transition, nuclear spins, and domain-driven transitions.” PhD thesis. 2021.

[Ji+21] H. Ji et al. “Disorder Effects on Quantum Transport and Quantum Phase Transition in Low-Dimensional Superconducting and Topological Systems.” In: *Advances in Physics: X* 6.1 (Jan. 2021), p. 1884133. ISSN: null. DOI: 10.1080/23746149.2021.1884133. (Visited on 07/26/2024).

[Kin+21] A. D. King et al. “Scaling Advantage over Path-Integral Monte Carlo in Quantum Simulation of Geometrically Frustrated Magnets.” In: *Nature Communications* 12.1 (Feb. 2021), p. 1113. ISSN: 2041-1723. DOI: 10.1038/s41467-021-20901-5. (Visited on 04/18/2024).

[Lib+21a] M. Libersky et al. “Direct Observation of Collective Electronuclear Modes About a Quantum Critical Point.” In: *arXiv:2101.05143 [cond-mat, physics:quant-ph]* (Oct. 2021). arXiv: 2101.05143 [cond-mat, physics:quant-ph].

[Lib+21b] M. Libersky et al. “Direct Observation of Collective Electronuclear Modes about a Quantum Critical Point.” In: *Physical Review Letters* 127.20 (Nov. 2021), p. 207202. DOI: 10.1103/PhysRevLett.127.207202.

[Lib+21c] M. Libersky et al. “Direct Observation of Collective Electronuclear Modes about a Quantum Critical Point (Supplemental Material).” In: *Physical Review Letters* 127.20 (Nov. 2021), p. 207202. DOI: 10.1103/PhysRevLett.127.207202. (Visited on 07/16/2024).

[Pre+21] A. Premkumar et al. “Microscopic Relaxation Channels in Materials for Superconducting Qubits.” In: *Communications Materials* 2.1 (July 2021), pp. 1–9. ISSN: 2662-4443. DOI: 10.1038/s43246-021-00174-7. (Visited on 08/03/2024).

[DAS22] T. Dollberg, J. C. Andresen, and M. Schechter. “Effect of Intrinsic Quantum Fluctuations on the Phase Diagram of Anisotropic Dipolar Magnets.” In: *Physical Review B* 105.18 (May 2022), p. L180413. ISSN: 2469-9950, 2469-9969. DOI: 10.1103/PhysRevB.105.L180413. (Visited on 03/30/2024).

[McK+22] R. D. McKenzie et al. “Theory of Magnon Polaritons in Quantum Ising Materials.” In: *Physical Review A* 106.4 (Oct. 2022), p. 043716. ISSN: 2469-9926, 2469-9934. DOI: 10.1103/PhysRevA.106.043716.

[Chi+23] S. Chigusa et al. “Dark Matter Detection Using Nuclear Magnetization in Magnet with Hyperfine Interaction.” In: *Physical Review D* 108.9 (Nov. 2023), p. 095007. ISSN: 2470-0010, 2470-0029. DOI: 10.1103/PhysRev

D.108.095007. arXiv: 2307.08577 [cond-mat, physics:hep-ex, physics:hep-ph, physics:quant-ph]. (Visited on 06/28/2024).

[Du+23] K. Du et al. "Kibble–Zurek Mechanism of Ising Domains." In: *Nature Physics* 19.10 (Oct. 2023), pp. 1495–1501. ISSN: 1745-2481. DOI: 10.1038/s41567-023-02112-5. (Visited on 03/15/2024).

[Jia+23] H. Jia et al. "Investigation of the Deposition of α-Tantalum (110) Films on a-Plane Sapphire Substrate by Molecular Beam Epitaxy for Superconducting Circuit." In: *Journal of Vacuum Science & Technology B* 41.5 (Sept. 2023), p. 052210. ISSN: 2166-2746. DOI: 10.1116/6.0002886. (Visited on 08/02/2024).

[KS23] M. Khalifa and J. Salfi. "Nonlinearity and Parametric Amplification of Superconducting Nanowire Resonators in Magnetic Field." In: *Physical Review Applied* 19.3 (Mar. 2023), p. 034024. ISSN: 2331-7019. DOI: 10.1103/PhysRevApplied.19.034024. (Visited on 12/11/2023).

[McK23] R. McKenzie. *Magnetostatic Modes and Criticality in Uniaxial Magnetic Materials*. Aug. 2023. arXiv: 2308.14169 [cond-mat].

[Su+23] Y. Su et al. "A Wide-Frequency-Tuning Micro-Loop-Gap Resonator for Miniature Rubidium Vapor-Cell Atomic Frequency Standards." In: *IEEE Transactions on Microwave Theory and Techniques* 71.12 (Dec. 2023), pp. 5135–5146. ISSN: 1557-9670. DOI: 10.1109/TMTT.2023.3276194. (Visited on 03/25/2024).

[Yap23] T. Yapo. *Tedyapo/Loopfield*. https://github.com/tedyapo/loopfield. Mar. 2023. (Visited on 03/22/2024).

[Mak+24] T. Makiuchi et al. *Field Dispersion and Strong Coupling of Nuclear-Electron Spin Excitation in $MnCO_3$*. May 2024. DOI: 10.48550/arXiv.2405.08323. arXiv: 2405.08323 [cond-mat]. (Visited on 06/28/2024).

[RBD24] J. R. Rumble, T. J. Brunno, and M. J. Doa, eds. *CRC Handbook of Chemistry and Physics: A Ready-Reference Book of Chemical and Physical Data*. 105th edition. CRC Handbook of Chemistry and Physics / Chemical Rubber Company 105th edition (2024). Boca Raton London New York: CRC Press, 2024. ISBN: 978-1-03-265562-8.

[seb24] sebastianprobst. *Sebastianprobst/Resonator_tools*. https://github.com/sebastianprobst/resonator_tools. July 2024. (Visited on 07/23/2024).

[Sta+24] P. Stamp et al. "Gallery of Soft Modes: Theory and Experiment at a Ferromagnetic Quantum Phase Transition." In: *Submitted to Physical Review B* (2024).

[Key] Keysight. *Group Delay*. https://helpfiles.keysight.com/csg/e5080b/Tutorials/Group_Delay6_5.htm. (Visited on 07/23/2024).

[LD] LD Didactic GmbH. *Electron Spin Resonance at DPPH - Determining the Magnetic Field as a Function of the Resonance Frequency - Electron Spin Resonance at DPPH - Determinig the Magnetic Field as a Function of the Resonance Frequency - Electron Spin Resonance - Atomic Shell - Atomic and Nuclear Physics - Physics Experiments - Physics*. https://www.leybold-shop.com/physics/physics-experiments/atomic-and-nuclear-physics/atomic-shell/electron-spin-resonance/electron-spin-resonance-at-dpph-determinig-the-magnetic-field-as-a-function-of-the-resonance-frequency/vp6-2-6-2.html. (Visited on 04/19/2024).

[MWS] MWS Wire. *Coil Winding Wire*. https://mwswire.com/magnet-wire/coil-winding-wire/. (Visited on 07/12/2024).